

Design of a Catheter Motion Control System

Submitted to the Graduate School of Natural and Applied Sciences
in partial fulfillment of the requirements for the degree of

Master of Science

in Mechanical Engineering

by

Gökmen Atakan Türkmen

ORCID 0000-0002-4845-6547

August, 2021

This is to certify that we have read the thesis **Design of a Catheter Motion Control System** submitted by **Gökmen Atakan Türkmen**, and it has been judged to be successful, in scope and in quality, at the defense exam and accepted by our jury as a MASTER'S THESIS.

APPROVED BY:

Advisor: **Assoc.Prof. Dr. Levent Çetin**
İzmir Kâtip Çelebi University

Committee Members:

Assoc. Prof. Dr. Erkin Gezgin
İzmir Kâtip Çelebi University

Assist. Prof. Dr. Barış Oğuz Gürses
Ege University

Date of Defense: August 9, 2021

Declaration of Authorship

I, **Gökmen Atakan Türkmen**, declare that this thesis titled **Design of a Catheter Motion Control System** and the work presented in it are my own. I confirm that:

- This work was done wholly or mainly while in candidature for the Master's / Doctoral degree at this university.
- Where any part of this thesis has previously been submitted for a degree or any other qualification at this university or any other institution, this has been clearly stated.
- Where I have consulted the published work of others, this is always clearly attributed.
- Where I have quoted from the work of others, the source is always given. This thesis is entirely my own work, with the exception of such quotations.
- I have acknowledged all major sources of assistance.
- Where the thesis is based on work done by myself jointly with others, I have made clear exactly what was done by others and what I have contributed myself.

Signature:

Date: 09.08.2021

Design of a Catheter Motion Control System

Abstract

Due to the risks of traditional surgical methods, the robotic technology has become more popular in the medical applications. Making large incisions in the patient's body may cause a permanent deformation on the patient during surgical operations. The surgical operations may become minimally invasive procedures by sending catheter systems to the channels in the body when possible. Apparently, one of the important key points in medical engineering is the control of the catheter system. The traditional catheter systems are controlled by surgical specialists using strings placed inside the catheter. This control strategy not only results in low positioning accuracy but also requires expertise to control. Besides, the catheter sizes became larger due to peripheral components. Therefore, automated control is a desired approach for providing high accuracy and versatility in catheter-based surgical operations.

In this thesis, the motion control of the catheter system used in the medical field in 2D space is concerned. Firstly, two actuator systems were designed to advance the catheter and to guide of the catheter tip in body vessels or channels. The advancement of the catheter was controlled by a friction drive system in a closed-loop manner. A novel sliding mode control was proposed to control the drive system. A millimeter size permanent magnet was placed at the tip of the catheter tube to control the orientation of the catheter. An untethered permanent magnet actuator is used to manipulate the position of the millimeter size permanent magnet directly and the orientation of the

catheter tube indirectly. The feedback for motion control was provided via machine vision setup. These three systems were operated synchronously using the Robot Operating System(ROS).

The performance of the motion control system was verified with a test rig which is a planar projection of 3D bronchial model data. The results showed that the proposed control methodology and the designed system can control catheter motion.

Keywords: Catheter drive, sliding mode control, untethered magnetic actuator



Kateter Hareket Kontrol Sisteminin Tasarımı

ÖZ

Geleneksel cerrahi yöntemlerinin riskli olması robotik teknolojisinin tıp alanında daha sık kullanılmasına sebep olmaktadır. Ameliyatlar sırasında hastanın vücudunda büyük kesikler açılmakta ve bu durum hastanın vücudunda kalıcı izler bırakabilmektedir. Vücut içindeki kanallara -mümkün olduğunda- kateter ile müdahale edilmesi ameliyatları minimal invaziv hale getirmektedir. Bu nedenle, tıbbi mühendislik uygulamalarında önemli olan konulardan biri de kateter sisteminin kontrol edilmesidir. Yaygın olarak kullanılan kateter sistemlerinin çoğu, cerrahlar tarafından kateterin iç kısmına yerleştirilmiş olan teller kullanılarak kontrol edilir. Bu kontrol stratejisi ile, istenilen pozisyon hassasiyeti elde edilmemekte hem de bu stratejinin uygulanması için uzmanlık gerekmektedir. Bu nedenle, otomatik kontrollü kateterler kullanılarak, cerrahi operasyonlarda yüksek doğruluk ve işlevsellik sağlamak istenilen bir yaklaşımdır. Bu tez kapsamında, tıp alanında kullanılan kateter sistemlerinin iki boyutlu uzayda hareket kontrolü ile ilgilenilmiştir. İlk olarak, kateter ucunun ilerlemesini ve yönlendirmesini sağlamak için iki eyleyici sistem tasarlanmıştır. Sürtünmeli tahrik sistemi kullanılarak kateter ilerlemesinin yüksek hassasiyetli kapalı döngü kontrolü yapılmıştır. Bu sistemin kontrollünde yeni bir kayan kipli denetleyici yöntemi kullanılmıştır. Kateterin yönelimini kontrol etmek için ise, kateterin uç kısmına milimetrik boyutlarda kalıcı mıknatıs yerleştirilmiştir. Bir temassız kalıcı mıknatıs eyleyiciyle, bu milimetre boyutundaki kalıcı mıknatısın konumu doğrudan ve de kateterin yönelimi dolaylı olarak değiştirilmiştir. Hareket kontrolü için geri

besleme, makine görmesi sistemi ile sağlanmıştır. Bu üç sistem, Robot İşletim Sistemi kullanılarak eş zamanlı olarak çalıştırılmıştır. Kateterin hareket kontrol sisteminin performansı, üç boyutlu bronşiyal model verilerinin düzlemsel bir projeksiyonu ile elde edilen deneysel düzenek üzerinde doğrulanmıştır. Sonuçlar, önerilen kontrol metodolojisinin ve tasarlanan sistemin, kateteri kontrol etme yeteneğine sahip olduğunu göstermiştir.

Anahtar Kelimeler: Kateter sürme, kayan kipli kontrol, bağlantısız manyetik eyleyici.





To my supportive mother

Acknowledgment

I would like to thank my advisor, Assoc. Prof. Dr. Levent Çetin for his valuable contributions to the creation of the thesis. I would like to thank Res. Asst. Nail Akçura and Faculty member Dr. Serkan Doğanay for helping with the image processing part and finite element analyses, respectively. I would also like to thank to Erdem Doguş Akkuş and Ali İhsan Tümkaya for design of Cartesian drive system. I also want to express my gratitude to Tugrul Uslu for his help in the production of the test rig.

The catheter tip motion control part of this study was supported by the Scientific and Technological Research Council of Turkey (TÜBİTAK, Grant No. 118E769). We would like to thank our project colleagues from the Microrobotics and Mechatronics Laboratory of the Department of Mechanical Engineering at Ege University for providing simulations of COMSOL Multiphysics program.

Table of Contents

Declaration of Authorship.....	ii
Abstract.....	iii
Öz.....	v
Acknowledgment	viii
Table of Contents	ix
List of Figures	xiii
List of Tables.....	xvii
List of Abbreviations.....	xviii
List of Symbols	xix
1 Introduction.....	1
1.1 Motivation	1
1.2 Literature Review	2
1.3 Contribution	7
2 Catheter Tip Motion	10
2.1 Frictional Drive Design Concept.....	10
2.1.1 Roller Design	11
2.1.2 Active Roller Driving System.....	12
2.2 Catheter Force and Motor Torque Relation Experiment.....	12
2.3 Mathematical Model of Frictional Drive	15
2.4 Sliding Mode Control.....	17
2.4.1 Classical Sliding Mode Controller Design.....	18

2.5	Chattering Attenuation Methods for Increasing the Control Performance	21
2.5.1	Quasi-Sliding Mode Control	21
2.5.2	Asymptotic Sliding Mode	22
2.6	Performance Improvement Method	23
2.6.1	Proportional Integral Asymptotic Sliding Mode Control (PIASMC)	23
2.7	Experimental Results.....	24
2.7.1	Test setup	25
2.7.2	The Controller Performance Tests	25
2.7.3	Controller Improvement.....	28
3	Catheter Guidance System	31
3.1	Permanent Magnet Actuator.....	31
3.1.1	Characteristics of the Permanent Magnet Inside the Catheter	31
3.2	Catheter Guidance	32
3.2.1	Magnetic Guidance via Permanent Magnet Actuator	32
3.2.2	The Force Required for Bending the Catheter	33
3.3	Permanent Magnet Actuator System Design	35
3.4	Finite Element Analysis for Permanent Magnets.....	36
3.4.1	Finite Element Analysis for a Single Permanent Magnet	37
3.4.2	Calculating Magnetic Force Values of a Single Magnet	40
3.4.3	Finite Element Analysis for Double Magnet System.....	42
3.4.4	Calculating Magnetic Force Values of Double Magnet System.....	44
3.4.5	Finite Element Analysis for Triple Magnet System.....	46

3.4.6	Calculating Magnetic Force Values of Triple Magnet System.....	48
3.5	Guidance Strategy	50
3.6	Guidance Results.....	51
3.6.1	Experimental Setup	51
3.6.2	Test Results	52
4	Machine Vision Feedback	55
4.1	Machine Vision	55
4.1.1	Obtaining the Digital Image.....	56
4.1.2	Identifying the Target in the Image.....	57
4.1.3	Noise Reduction Methods.....	60
4.1.4	Obtaining the Position Information of The Target in The Working Environment.....	63
5	Catheter Motion	66
5.1	Task Controller.....	67
5.2	ROS Based Control	67
5.2.1	Filesystem Level	67
5.2.2	Computation Graph Level.....	68
5.2.3	ROS Community Level.....	69
5.2.4	Basic ROS Commands.....	69
5.2.5	ROS Packages	69
5.3	Working Environment.....	73
5.4	Motion Control Experiment	74
5.4.1	Experimental Result.....	76
5.5	Discussion	82

6 Conclusion.....	84
References	86
Curriculum Vitae.....	98



List of Figures

Figure 1.1 The Sensei Robotic Navigation System [16].....	2
Figure 1.2 Stereotaxis Niobe Magnetic Navigation System [29]	3
Figure 1.3 Imaging (CGCI) Magnetic Navigation System [31]	4
Figure 1.4 Catheter Driving System (Weixing et al. [37]) (A) Disk gear, (B) Drive gear, (C) Gear group, (D)(E) Step Motor, (F)(G)(H) Bracket, (I) Catheter	5
Figure 1.5 Catheter Driving System (Xu et al. [38]).....	6
Figure 1.6 Catheter Drive System (Fumihito et al. Research [39])	6
Figure 1.7 System General Block Diagram	7
Figure 1.8 External Magnetic Field Effect on the Small Magnetic Particle Tipped Catheter	8
Figure 2.1 Frictional Catheter Driving Diagram a) Front View, b) Side View	11
Figure 2.2 Passive Roller Design	11
Figure 2.3 Frictional Catheter Driving System	12
Figure 2.4 The Simple Seesaw Mechanism	13
Figure 2.5 Seesaw Mechanism.....	14
Figure 2.6 Current And Force Relation.....	15
Figure 2.7 Frictional Catheter Driving System, a) CAD Design, b) Diagram.....	15
Figure 2.8 Static and Kinetic Friction	16
Figure 2.9 Frictional Catheter Driving System	25
Figure 2.10 Sliding Mode Controller Control Actions and Position State Result When Goal Position 200 mm a-b) Classical Sliding Mode, c-d) Quasi Sliding Mode, e-f) Asymptotic Sliding Mode	27

Figure 2.11 Sliding Mode Controller Control Actions and Position State Result When Goal Position 5 mm a-b) Classical Sliding Mode, c-d) Quasi Sliding Mode, e-f) Asymptotic Sliding Mode.....	28
Figure 2.12 Proportional Integral Asymptotic Sliding Mode a) Position State Result b) Actions State Result	29
Figure 3.1 Simple Cantilever Beam Schematic	34
Figure 3.2 a) Block Magnet Representation b) Cylindrical Magnet Representation c) Ring Magnet Representation d) Spherical Magnet Representation	36
Figure 3.3 Geometric View Of a) All System, b) Single Magnet System.....	37
Figure 3.4 Magnetic Field X-axis Values Dependent On Number of Mesh.....	38
Figure 3.5 Mesh View of a) All System, b) Single Magnet System.....	38
Figure 3.6 Magnetic Flux Density Norm	39
Figure 3.7 Coordinate Grid Values	40
Figure 3.8 Magnetic Effect on Different Y-axis Values in X and Z Planes a-c-e) Magnetic Force Magnitudes, b-d-f) Magnetic Force Vector Direction ..	41
Figure 3.9 Magnetic Effect on Different Z-axis Values in X and Z Planes a-c-e) Magnetic Force Magnitudes, b-d-f) Magnetic Force Vector Direction ..	42
Figure 3.10 Geometric View of a) All System, b) Double Magnet System	43
Figure 3.11 Mesh View of a) All System, b) Double Magnet System	43
Figure 3.12 Magnetic Flux Density Norm	44
Figure 3.13 Magnet Effect on Different Y-axis Values in X and Z Planes a-c-e) Magnetic Force Magnitudes, b-d-f) Magnetic Force Vector Direction ..	45
Figure 3.14 Magnet Effect on Different Z-axis Values in X and Z Planes a-c-e) Magnetic Force Magnitudes, b-d-f) Magnetic Force Vector Direction ..	46
Figure 3.15 Geometric View of a) All System, b) Triple Magnet System	47
Figure 3.16 Mesh View of a) All System, b) Triple Magnet System	47
Figure 3.17 Magnetic Flux Density Norm	48
Figure 3.18 Magnet Effect on Different Y-axis Values in X and Z Planes a-c-e) Magnetic Force Magnitudes, b-d-f) Magnetic Force Vector Direction ..	49

Figure 3.19 Magnet Effect on Different Z-axis Values in X and Z Planes a-c-e) Magnetic Force Magnitudes, b-d-f) Magnetic Force Vector Direction ..	50
Figure 3.20 Magnet Motion System	52
Figure 3.21 Magnet Position and Catheter Bending Angle	53
Figure 3.22 Magnet Distance and Catheter Angle Relation	54
Figure 4.1 Illumination System and Working Environment.....	57
Figure 4.2 HSV Color Circle [77].....	58
Figure 4.3 HSV Color Bar Selection	58
Figure 4.4 HSV Position Detection a) Captured Image, b) Masking of the Captured Image.....	59
Figure 4.5 Median and Gaussian Filters with HSV Position Detection a) Captured Image, b) Masking of the Captured Image.....	61
Figure 4.6 Median, Gaussian, Erosion and Dilation Filters with HSV Position Detection a) Captured Image, b) Masking of the Captured Image	62
Figure 4.7 The Working Environment Calibration Points.....	63
Figure 4.8 Curve Fitting Results of the xt.....	64
Figure 4.9 Curve Fitting Results of the yt	64
Figure 5.1 System Block Diagram.....	66
Figure 5.2 Graphical Representation Of ROS Procedure	68
Figure 5.3 Catheter Driving System Block Diagram.....	70
Figure 5.4 Magnet Driving System Block Diagram	71
Figure 5.5 Machine Vision Feedback Block Diagram.....	72
Figure 5.6 QT-Design Block Diagram.....	73
Figure 5.7 2D Bronchial CAD Model.....	73
Figure 5.8 Working Environment of a) CAD Model, b) Test Rig.....	74

Figure 5.9 Experimental Setup a) Test Rig b) Experimental Setup Components (i- Frictional Drive, ii-Guidance System, iii-Image Acquisition System, iv- Test Rig and Its Illumination System).....	75
Figure 5.10 User Interface.....	76
Figure 5.11 Desired Position 1 of the Catheter Motion System a) Position State, b) Input Graph, c) Position Path of The Catheter, d) The Images of System at Certain Times	77
Figure 5.12 Desired Position 2 of the Catheter Motion System a) Position State, b)Input Graph, c) Position Path of The Catheter, d) The Images of System at Certain Times	78
Figure 5.13 Desired Position 3 of the Catheter Motion System a) Position State, b)Input Graph, c) Position Path of The Catheter, d) The Images of System at Certain Times	79
Figure 5.14 Desired Position 4 of the Catheter Motion System a) Position State, b)Input Graph, c) Position Path of The Catheter, d) The Images of System at Certain Times	80
Figure 5.15 Desired Position 5 of the Catheter Motion System a) Position State, b)Input Graph, c) Position Path of The Catheter, d) The Images of System at Certain Times	81
Figure 5.16 Desired Position 6 of the Catheter Motion System a) Position State, b)Input Graph, c) Position Path of The Catheter, d) The Images of System at Certain Times	82

List of Tables

Table 2.1	Sliding Mode Control Performance	25
Table 3.1	Magnet Distance to Rotation Angle	49
Table 5.1	ROS Commands.....	64



List of Abbreviations

CGCI	Catheter Guidance Control and Imaging
EMA	Electromagnetic Actuator
HSV	Hue Saturation Value
MAE	Mean Absolute Error
PIASM	Proportional Integral Asymptotic Sliding Mode
ROS	Robotic Operating System
SMC	Sliding Mode Control

List of Symbols

τ_m	Motor Torque [Nm]
μ	Friction Coefficient [.]
σ	Sliding Surface [.]
ω	Angular Velocity [rad/s]
F_m	Catheter Force [N]
m	Mass [kg]
r	Active Cylinder Radius [mm]
N	Normal Force [N]
F_f	Friction Force [N]
v	Lyapunov Stability Function [.]
φ	Switching Function [.]
s	The Auxiliary Sliding Variable [.]
u	Input Signal [N]
d	Material Compression Amount [mm]
x_1	Position State [mm]
x_2	Velocity State [mm/s]
x_d	Desired Position [mm]
\dot{x}_d	Desired Velocity [mm/s]
F_d	Bounded Unknown Disturbance Value [N]
$f(x_2, t)$	Uncertainty in System [N]
ζ	The Derivative of The Control Input [.]
K	Proportional Gain Parameter [.]

\vec{M}	Magnetization Vector [.]
\vec{B}	Magnetic Flux Density [T]
$\nabla\vec{B}$	Gradient of the Magnetic Flux Density [.]
\vec{F}_m	Magnetic Force [N]
$\vec{\tau}_m$	Magnetic Torque [Nm]
I	Second Moment of Inertia mm ⁴
σ_t	Tensile Stress [MPa]
ϵ_t	Tensile Strain [.]
E	Young Modules [MPa]
α	Slope of Material [radian]
δ	Deflection of Material [mm]
B_r	Remanence of Permanent Magnet [T]

Chapter 1

Introduction

The surgical methods are important procedures for interventional medicine. Technological developments made surgical procedures more sensitive, reliable, less harmful, and easier for the patients and surgeons [1]. Due to the contribution to patient's comfort during recovery, the minimally invasive techniques have become increasingly popular in recent years, both for diagnosis and surgery in medical practice [2, 3].

1.1 Motivation

Endoscopy, bronchoscopy, angiography, and colonoscopy are some of the most common applications of minimally invasive methods to view and manipulate the organs with a catheter [4]. The endoscopy is performed with catheters sent to the canals in the body [5, 6]. Therefore, the catheter control has a critical role in this type of operation, as improperly moving catheters may harm the organs [7, 8]. Most catheter systems are controlled by experts using strings placed inside the catheter [9]. This control strategy provides low steering accuracy [10]. Therefore, automated control is an attractive strategy for providing automation, versatility, and low risk in catheter-based surgical operations [11]. Also, the surgical experts do not meddle to learn how to control the system. In addition, when the catheter is controlled automatically, surgeries became faster and safer [12]. Moreover, patients and surgical professionals are less exposed to radiation from X-ray fluoroscopy [13]. Concerning the mentioned concept this study focuses on motion control of a catheter system.

1.2 Literature Review

The catheter system consists of guidance and drive systems. The guidance system enables the catheter to bend and the drive system advances the catheter tube. With the synchronous operation of systems, the motion control of the catheter is accomplished.

The guidance system is usually controlled using strings placed inside the catheter systems [14, 15]. The Sensei robotic navigation system is one of the common on-the-shelf catheter systems [16] (Figure 1.1). It exploits tendon drives for controlling catheter tip motion and provides a haptic interface for control of the surgeon. Such systems have disadvantages of having lower accuracies and not being fully automated as mentioned above.

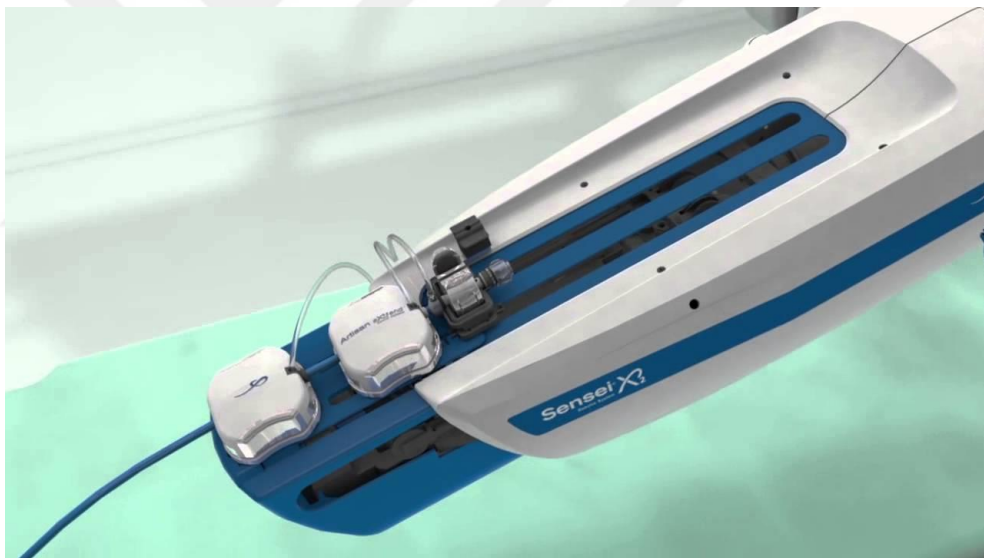


Figure 1.1: The Sensei Robotic Navigation System [16]

A recent approach to catheter guidance is to use magnetic fields. For this purpose, the magnets are used for pushing or pulling magnetic particles placed in the catheter to bend it [10, 17]. By this means, the torque required for the guidance of the catheter can be transferred to the microparticles from the external magnetic actuator [18, 19]. The reason for the higher position accuracy of this process is that the small-scaled microparticles placed at the tip of the catheters make the catheter more versatile [20].

The surgical operations performed with microparticle carrying catheters require precise control. The catheters eventually don't damage healthy tissues. They only interact with the targeted area [21].

The magnetic actuators are divided into two groups as active and passive actuators [22, 23]. The active magnetic actuators are also known as electromagnetic actuator (EMA) systems. It converts electrical energy to magnetic energy [24, 25]. The control of the magnetic torque and force acting on the microparticle are provided by the structural features of the electromagnetic actuator system and the control of the applied electrical current [24, 26]. A passive magnetic actuator (permanent magnet), on the other hand, applies a magnetic force depending on its distance from the microparticle [27, 28].

Stereotaxis Niobe Magnetic Navigation System (Figure 1.2) [15, 29] facilitates vector-based navigation by placing two permanent magnets on opposite sides of the patient table to produce a magnetic field. By changing the positions of the permanent magnets, the magnetic force applied to the catheter is changed. However, the Niobe system has the following disadvantages: The two permanent magnets are too large, it cannot be control in real-time and the produced magnetic field is limited.



Figure 1.2: Stereotaxis Niobe Magnetic Navigation System [29]

Catheter Guidance Control and Imaging (CGCI) Magnetic Navigation System (Figure 1.3) [30] consists of eight electromagnets placed semi-spherically on the patient table. It can change the magnitude, direction, and gradient of the magnetic field in real-time. In this way, it can apply torque (bending) or force (pull or push) to the catheter. One of the biggest disadvantages of electromagnetic systems is the heating problem during operation.

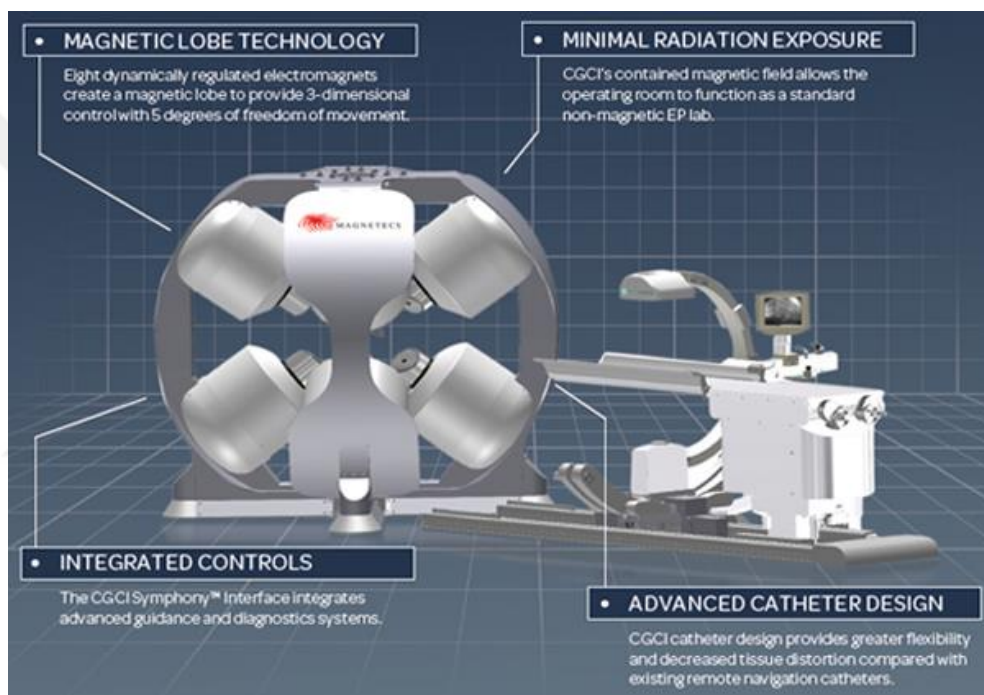


Figure 1.3: Imaging (CGCI) Magnetic Navigation System [31]

The driving system is used for the advancing the catheter. The driving system provides the necessary driving force to transmit to the catheter according to the structural properties of the catheter. The control of the transmitted force can be carried out by various actuators and controller methods.

Weixing et al. designed a high-precision catheter drive system using the master-slave approach [8] (Figure 1.4). The sensitivity of the system is 0.015 mm, which is accomplished by gear systems and a large driving cylinder. They aimed to transfer the torque produced in the actuator to the catheter without any loss, using the friction

driving system [32]. Friction drive systems [33] are actuator systems that transfer force or torque to the output port using a friction cylinder connected to any source of force or torque. These may be considered as two-link (motor-driven friction wheel and catheter) mechanisms with a standard kinematic pair consistent with the one degree of freedom. When operated concerning the rolling without slippage condition, torque or force on the drive shaft is transmitted to the catheter without loss or slippage [2]. Frictional catheter drive systems have the advantage of directly controlling and limiting the interaction force, making them preferred as actuators in continuous robotic systems [34] and biomedical devices [35]. The main disadvantage of friction drive systems is that slipping is handled very carefully in the design stage. The system is controlled in torque mode and the amount of force transferred to the catheter is limited due to avoid the slipping problem. The lack of force control and force range limitation in the mentioned study does not provide any explanation for possible slippage problem in the setup. In addition, it can be seen in the figure that the size of the driving system is not suitable for the surgical area.

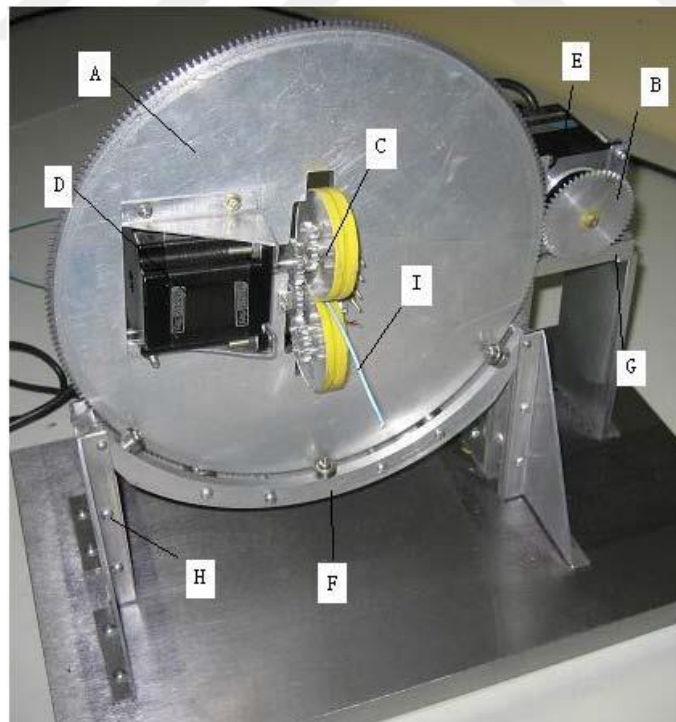


Figure 1.4: Catheter Driving System (Weixing et al. [8]) (A) Disk gear, (B) Drive gear, (C) Gear group, (D)(E) Step Motor, (F)(G)(H) Bracket, (I) Catheter

Xu et al. [36] used the same type of catheter driving system, and unlike the previously mentioned study, researchers use a sensor to measure the force on the tip of the catheter (Figure 1.5). The researchers use force control in this system but did not consider the slippage effect in the study.

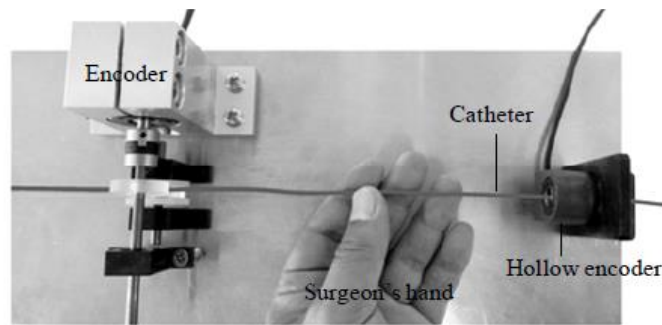


Figure 1.5: Catheter Driving System (Xu et al. [36])

Fumihito et al. [37] presented a linear stepping mechanism for catheter driving (Figure 1.6). This study proposes a linear push-pull mechanism to overcome the slippage problem in frictional drives. However, it is insufficient for catheter drive systems because it is not suitable for position control and has low accuracy and precision. Besides, it is not suitable for surgical operation due to a lack of force control.

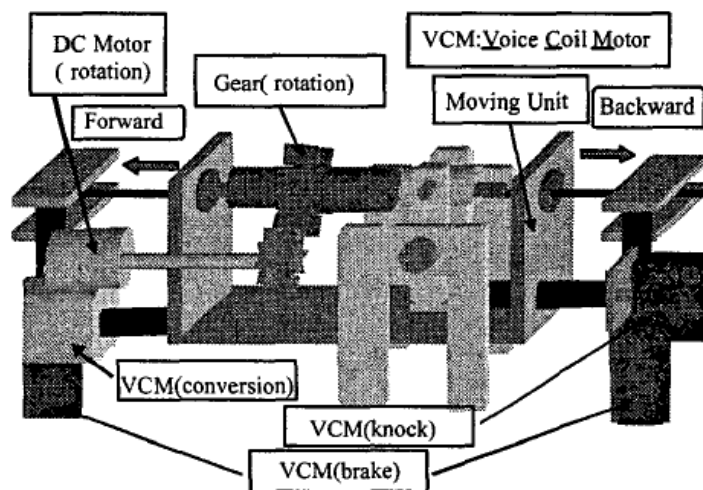


Figure 1.6: Catheter Drive System (Fumihito et al. Research [37])

1.3 Contribution

In this study, automatic motion control of the catheter system is proposed. The catheter is driven using a frictional drive and guided by an untethered permanent magnet actuator. The general block diagram of the system is shown in Figure 1.7.

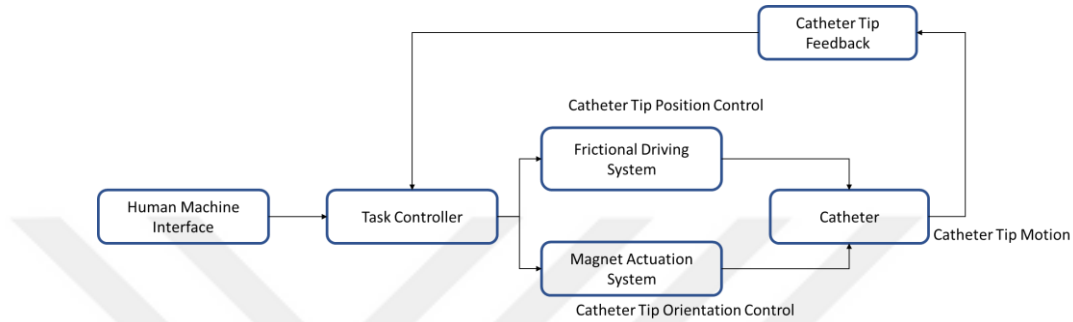


Figure 1.7: System General Block Diagram

The main concerns in catheter drive systems are: precise movement, force limitation, and the robustness of controllers [8]. First, the classical sliding mode controller is applied [38] to obtain a suitable controller for the frictional catheter drive system. Then the two chattering attenuation methodologies, which are quasi sliding mode [39], and asymptotic sliding mode controller [40], were used. The performances of each of the controllers were analyzed experimentally and the controller parameters are adjusted by trial and error. The performances of the controllers were compared with mean absolute error (MAE), rise time, settling value and overshoot controller metrics. Later, a new controller method, Proportional Integral Asymptotic Sliding Mode, was proposed by combination and updating of the multiple controllers to improve the performance of the system. In the guidance system, permanent magnet actuation was used. The distribution of the magnetic forces produced by the magnet with various configurations was obtained by Finite Element Analysis [22]. Magnet actuation system has two degrees of freedom. The pole directions of the permanent magnet and the small particle are kept opposite so the permanent magnet can pull the small particle in the catheter by using an external magnetic field. The guidance phenomena of the system is given in Figure 1.8. In the figure, the external magnetic field is generated by the

permanent magnet and the catheter tip tries to align with the magnetic field direction. In this way, it was thought that wherever the magnet guidance system goes, the catheter follows the system and tries to align with the magnetic field direction.

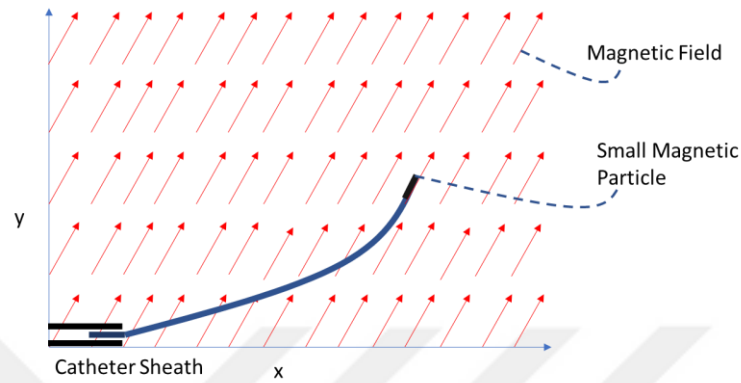


Figure 1.8: External Magnetic Field Effect on the Small Magnetic Particle Tipped Catheter

In this study, a low-cost optical tracking system was designed according to the stereo vision principle for the positioning of the catheter [41]. HSV color model was used for the detection of the catheter tip. Various filtering methods were used to remove the noise. Then, a set of calibration points were marked and the pixel and real coordinates of those points were extracted for the calibration process. The camera was calibrated using the curve-fitting method [42]. Then, using the K Nearest Neighborhood method, the amount of advancement required for the catheter to reach the desired location was found [43–45]. The accuracy of K Nearest Neighborhood is 99.9%. The drive, the guidance, and the machine vision systems were worked synchronously to operate the catheter positioning with the automatic control method. For this, three systems were operated synchronously by using Robotic Operating System (ROS) [46].

This Thesis is organized as follows. Section 2 presents the conceptual design of the catheter driving system and controller algorithm. Section 3 present the catheter guidance system strategy. Section 4 shows a visual feedback system. Section 5 mentioned catheter motion and the human-machine interface. Section 6 presents the conclusions and future work for this thesis.



Chapter 2

Catheter Tip Motion

This section presents the modeling and design of the catheter drive system. The catheter was ensured to move in a hollow pipette by using the sliding mode controller. In this experiment, the performance of the catheter tip motion controller was examined.

2.1 Frictional Drive Design Concept

In this study, the frictional drive mechanism is chosen for the catheter drive system. The main issues in such medical systems are safety, easy insertion of the catheter into the drive system, and reducing the slippery effect caused by the frictional drive mechanism. The basic idea of the friction drive mechanism is, an active cylinder is driven by a motor and a passive cylinder creates a pressure point between the catheter and the active cylinder. The conceptual design of the proposed actuator system is shown in Figure 2.1. The main purpose of the passive cylinder is to prevent the catheter from slipping and transmit the active cylinder force to the catheter without any loss. In this way, the catheter have 1DOF mobility and the efficiency of the mechanism is kept high. In the first step, active and passive cylinders were designed. The second step is the designing process of the active cylinder system.

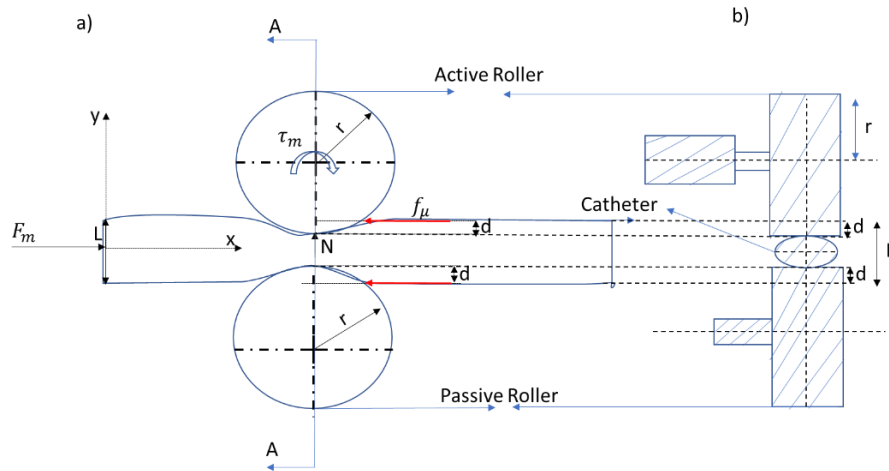


Figure 2.1: Frictional Catheter Driving Diagram a) Front View, b) Side View

2.1.1 Roller Design

In this concept, the system was designed similar to the Weixing roller mechanism which was used in this work [8]. First, a two-cylinder was designed. Then, the outside of the cylinders was covered with a high frictional rubber material. Some trials were made before designing the active cylinder. Initially, a base was designed to keep the two cylinders parallel to each other. Then, a catheter was placed in the middle of the cylinders which is shown in Figure 2.2. Then a force was applied manually to observe the catheter movement. This experimental part also helps us to find the optimal catheter pressure distance (which is d) between the catheter and cylinders to ensure easy insertion of the catheter and a drive without the slipping effect. As a result of this experiment, the d value was found as 0.5 mm.

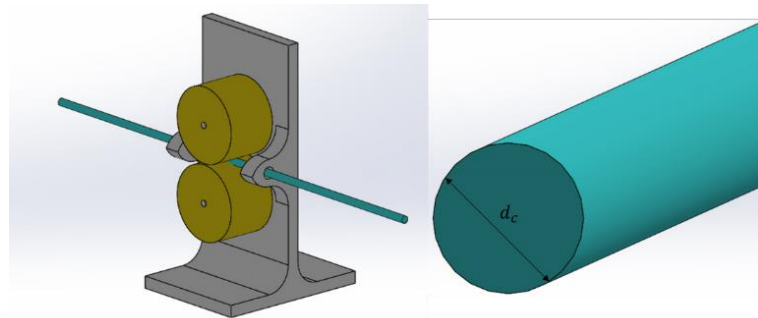


Figure 2.2: Passive Roller Design

2.1.2 Active Roller Driving System

The design of the active cylinder includes several key points for choosing the actuator. The actuator should control motor torque, position, and speed and provide feedback information about the system at the same time. Dynamixel XM430-W350 type intelligent servo motor is used for this system. This type of motor has a high stall torque (4.1 [N.m]). The frictional catheter drive system is shown in Figure 2.3. This mechanism design has facilitated the insertion of the catheter. Position accuracy is high thanks to the 12-bit global encoder in the motor. The system has a 0.6 mm accuracy.

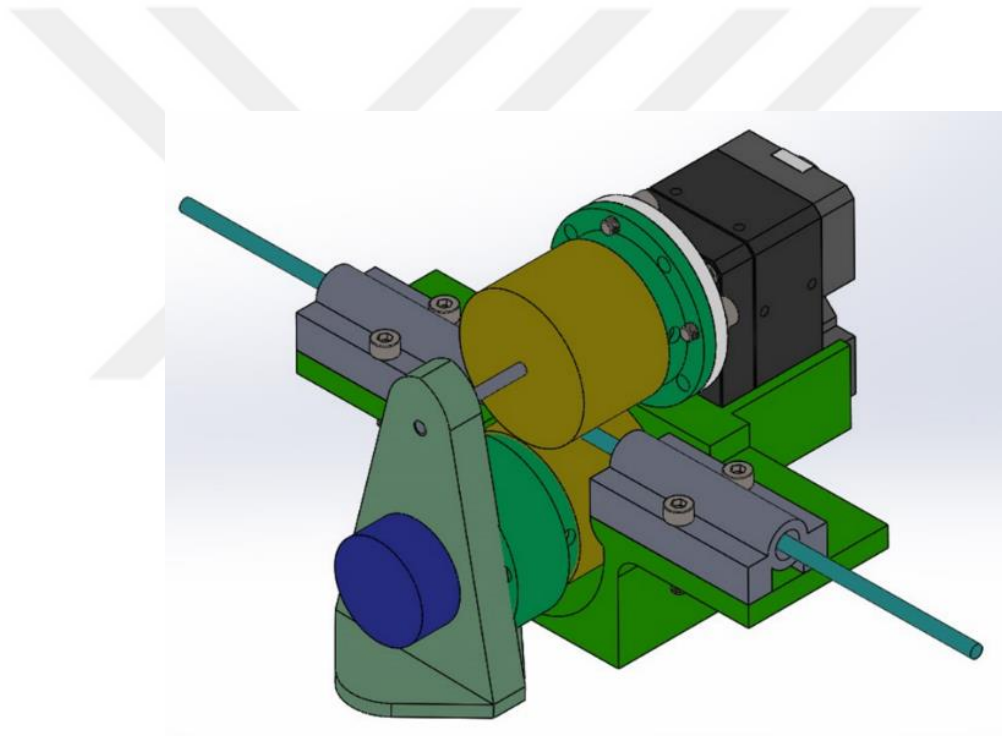


Figure 2.3: Frictional Catheter Driving System

2.2 Catheter Force and Motor Torque Relation

Experiment

In this section, the slip factor was examined. The slip factor occurs in the system, if the applied force is higher than the friction force between the active cylinder and the

catheter [47]. In the friction drive system, there is a possibility that not all torque is transferred to the catheter. There is a critical applied force value to prevent slipping. Therefore, an experiment is created to observe the slippage effect in the system. Leine et al. [48] mentioned a similar experimental setup in their research. First of all, 1 DOF model is designed to represent friction as a function of relative velocity. Therefore, the actuator limit force value is found when it exceeds the friction force. Also, the relationship between motor torque and catheter force is found. First, a simple seesaw mechanism is designed. The simple seesaw concept is given in Figure 2.4.

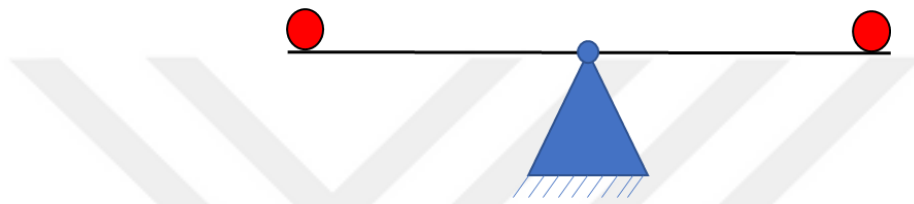


Figure 2.4: The Simple Seesaw Mechanism

According to this principle, an object with a mass of 1 kg was attached to one side of the seesaw and a precision scale was attached to the base of the mass. The catheter was attached to the other side of the seesaw to pull the handle. In this way, the applied force to the catheter was obtained in weight by using a precision scale. Then, the obtained values were multiplied by the gravitational constant and converted to the force. Then, the different current values were applied from the actuator and the force values from the precision scale were collected. Then, a linear relationship between the current value and the force value was found by using the Curve Fitting method in the Excel program. Finally, a linear prediction function is obtained with 99% accuracy which was shown in Figure 2.6.

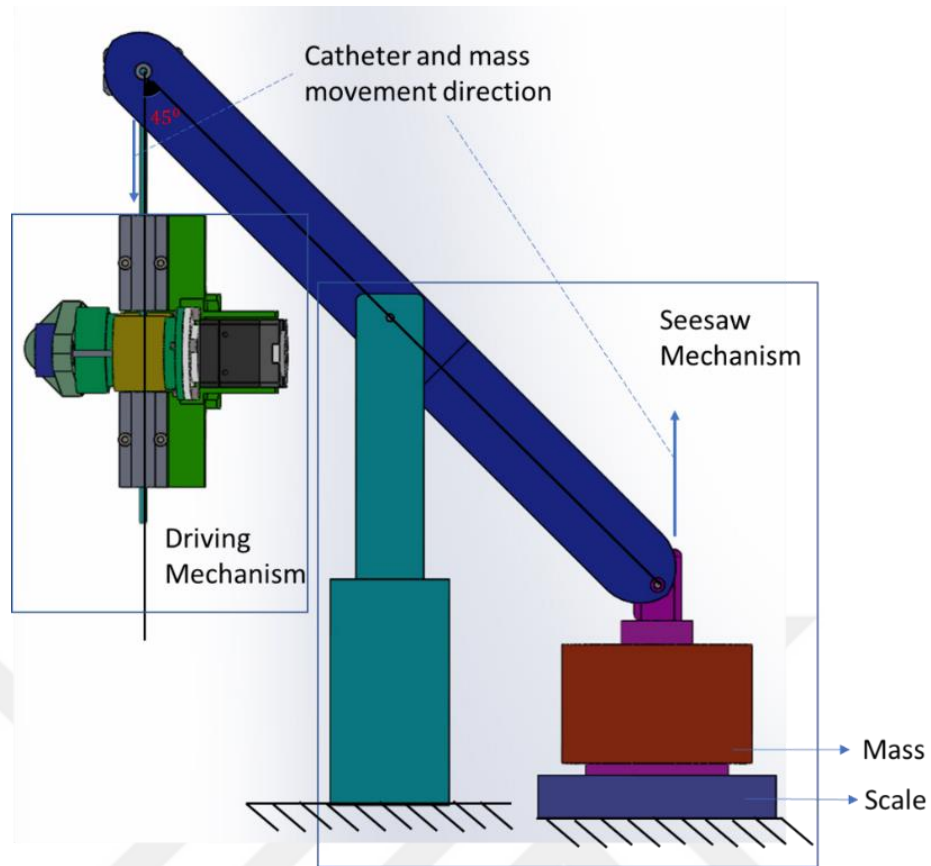


Figure 2.5: Seesaw Mechanism

It was also observed that there was a slippage when the force exceeds 6 N during the experiment. The slip effect was observed because the catheter could not lift the weight but the driving system is still working. The slip effect was observed only a brief moment at the beginning of the experiment. In this criterion, the slippage effect was eliminated by limiting the maximum force value to 5 N and the maximum current value to 110mA.

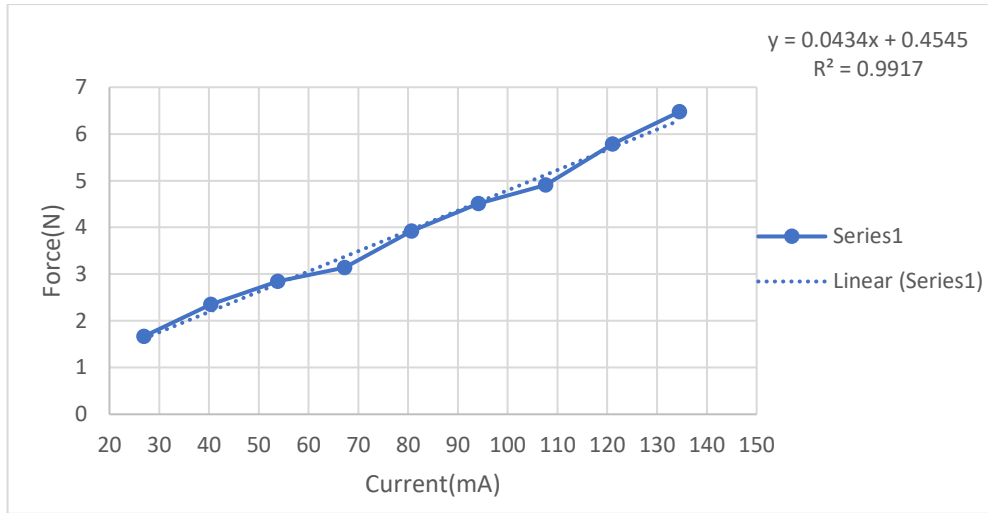


Figure 2.6: Current And Force Relation

2.3 Mathematical Model of Frictional Drive

The mathematical modeling of the proposed friction drive system (Figure 2.7a) is presented in this section. The dynamical interaction between rollers and the catheter is presented schematically in Figure 2.7b.

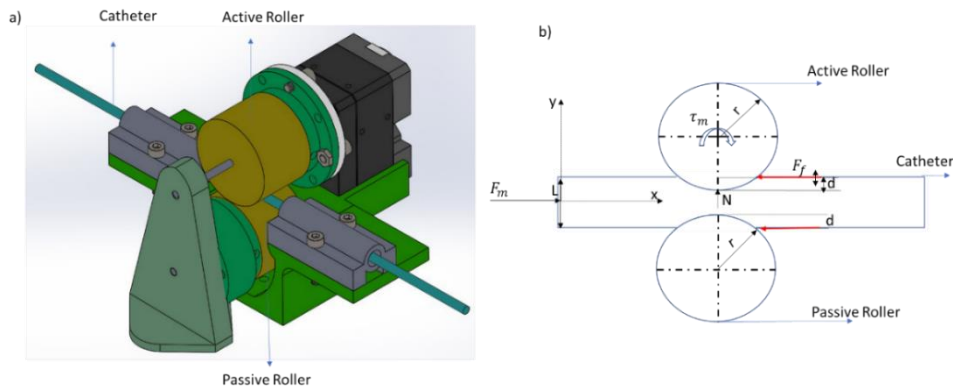


Figure 2.7: Frictional Catheter Driving System, a) CAD Design, b) Diagram

The force transferred to the catheter (F_m) is calculated with the radius of the active cylinder (r) is given in Equation 2.1.

$$F_m = \frac{\tau_m}{r} \quad (2.1)$$

Equation 2.1 is only valid when F_m is smaller than the friction force (F_f) between the catheter and the cylinders. The frictional force can be calculated using the friction coefficient (μ) between catheter and cylinder and the normal force (N) at the point of contact (Equation 2.2).

$$F_f = 2\mu N \quad (2.2)$$

As seen in Figure 2.1b, the cylinders compress the catheter and causing the elastic deformation of the catheter. Therefore, the friction force can be calculated by assuming that the catheter is a spring with an equivalent coefficient of (k) and compressed by an amount of d (Equation 2.3). Eventually, the normal force can be calculated as in Equation 2.3.

$$F_f = 2\mu kd \quad (2.3)$$

Applied force must exceed the static friction force to move an object. After that object is affected by kinetic friction force when the object starts the motion [49]. Applied force and the friction force relation is present in Figure 2.8.

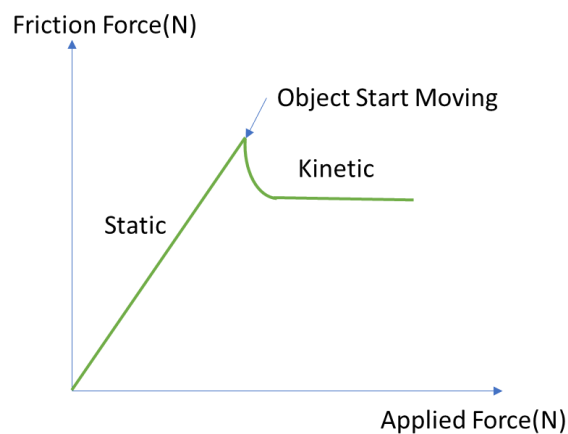


Figure 2.8: Static and Kinetic Friction

If the driving force is higher than the friction force ($F_m > F_f$), the movement of the catheter and friction pulley becomes independent and the system makes two degrees of freedom movement. Otherwise ($F_m \leq F_f$), the movement of the catheter and the friction pulley are dependent, and the system moves with a single degree of freedom. The dynamic of a single degree of freedom is obtained as Newton's Second Law (Equation 2.4).

$$m\ddot{x} = F_m - f(\dot{x}, t) \quad (2.4)$$

The catheters interact with tissues and fluids when moving through the body [21]. As a result, the effects of internal body interactions as unknown disturbances in the system model were observed. However, the limits of uncertain interaction forces can be predicted based on the properties of tissues and body fluids. In the formulation of any practical control problem, there is always a discrepancy between the actual and the mathematical model. These inconsistencies can consist of unknown external factors [41, 42], model parameters [43] and parasitic or unmodified dynamics [44]. In the presence of these disturbances or uncertainties, it is a very difficult task to design control laws that satisfy the desired operational specification [45]. Considering these factors in catheter control, a robust controller is designed [46] by adopting the sliding mode control.

2.4 Sliding Mode Control

The sliding mode controller can handle the non-linear system model [47]. The advantages of the sliding mode controller can be designed for robustness [48], ability to deal with nonlinear systems [49], time-varying systems [50] and fast dynamic responses [51]. The sliding mode control changes the input signal of the controller in response to reach the desired states. The controller reaches the desired states in the system by switching the input signal on and off at a high frequency [52]. Consequently, the implementation of sliding mode control requires a high-frequency switching control input. The chattering phenomenon is observed when the high-frequency

switching input signals exist due to the unknown system dynamics [53–55]. This phenomenon can lead to a decrease in system efficiency and damage the system.

First, the classical sliding mode control is applied to the system. After that, two chattering attenuation methods are applied, which are quasi and asymptotic sliding mode controllers. It is important to keep the chattering is minimum rather than eliminating completely. This is related to the static and kinetic friction situation which is mentioned in section 2.3. If the system is constantly in the motion, only kinetic friction affects the catheter. In conclusion, the drive and guidance system easily takes the catheter to the desired position. Afterwards, the performances of the controllers were examined and some modifications on the controllers in experimental states

2.4.1 Classical Sliding Mode Controller Design

Using the mathematical model in Equation 2.4, the position and velocity error of the catheter tip is shown in Equations 2.5, 2.6, 2.7 and 2.8.

$$x_1 = x - x_d \quad (2.5)$$

$$x_2 = \dot{x} - \dot{x}_d \quad (2.6)$$

$$\dot{x}_1 = x_2 \quad (2.7)$$

$$\dot{x}_2 = u + f(x_2, t) \quad (2.8)$$

u is a time-dependent input function of the system and produces the function that minimizes the tracking error defined in Equations 2.7 and 2.8. In Equation 2.8, u is the control input and $f(x_2, t)$ is considered as viscous friction from the mucus fluid. Accordingly, it was assumed that the viscous friction acting on the catheter tip would be below a certain limit under all conditions.

$$|f(x_2, t)| \leq F_d \quad (2.9)$$

To calculate the robust controller input signal, first, the sliding surface is defined as follows:

$$\sigma(x_1, x_2) = x_2 + cx_1 \quad c > 0 \quad (2.10)$$

To guarantee the stability of the controller, a Lyapunov stability function is proposed in Equation 2.11.

$$v = \frac{1}{2} \sigma^2 \quad (2.11)$$

If $v(x)$ is greater than or equal to zero and the time derivative of this Lyapunov function is less than zero for all values of x , the system is asymptotically stable. To ensure the negativity of \dot{v} , a limiting function is assumed as the design parameter α which is shown in Equation 2.12:

$$\dot{v} \leq -\alpha\sqrt{v} \quad (2.12)$$

If the system model is written in terms of σ for stability analysis, the following equations are obtained. Then the time-dependent response of the Lyapunov Function is calculated accordingly. Using the conditional system dynamics given in Equation 2.12, the response of the slip surface with respect to time (Equation 2.13) and the derivative of Lyapunov function (Equation 2.14) are obtained:

$$\dot{\sigma} = \dot{x}_2 + c\dot{x}_1 = u + f(x_2, t) + cx_2 \quad (2.13)$$

$$\dot{v} = \sigma\dot{\sigma} = \sigma(u + f(x_2, t) + cx_2) \quad (2.14)$$

The control input u is defined in Equation 2.15 and it is used in Equation 2.16 and the new expression for \dot{v} can be obtained as in Equation 2.17.

$$u = -cx_2 + \theta \quad (2.15)$$

$$\dot{v} = \sigma(f(x_2, t) + \theta) \quad (2.16)$$

$$\dot{v} = \sigma(f(x_2, t) + \theta) \leq |\sigma|F_d + \sigma\theta \quad (2.17)$$

The following equation is obtained by using Equation 2.11 and the absolute value of the slip surface is shown in Equation 2.18.

$$|\sigma| = \mp\sqrt{2v} \quad (2.18)$$

The derivative of the Lyapunov function with respect to time (Equation 2.19) is obtained using Equations 2.12 and 2.18.

$$\dot{v} = \frac{-\alpha|\sigma|}{\sqrt{2}} \quad (2.19)$$

As seen in Equation 2.19, the design parameter (α) can be included in the Lyapunov basic design procedure. To advance the controller design, a switching function with $\varphi > 0$ is given in Equation 2.20 to keep the system states on the slip surface. Equations are updated according to Equation 2.20:

$$\theta = -\varphi \text{sgn}(\sigma) \quad (2.20)$$

$$\dot{v} \leq -|\sigma|(\varphi + F_d) \quad (2.21)$$

The amplitude (φ) of the switching function was calculated by considering Equations 2.9, 2.16 and 2.21. The control input u is defined in Equation 2.15.

$$\dot{v} \leq \frac{-\alpha|\sigma|}{\sqrt{2}} = -|\sigma|(\varphi + F_d) \quad (2.22)$$

$$\varphi = \frac{\alpha}{\sqrt{2}} + F_d \quad (2.23)$$

Finally, the control effect is proposed in Equation 2.24, which is the combination of the sliding mode control and the proportional controller of the catheter tip position.

$$u = -cx_2 - Kx_1 - \left(\frac{\alpha}{\sqrt{2}} + F_d\right)sgn(\sigma) \quad (2.24)$$

2.5 Chattering Attenuation Methods for Increasing the Control Performance

As mentioned above, a major problem of sliding mode control due to high-frequency switching is chattering. However, there are several suggested methods to reduce the chattering to a certain level [50, 51]. In this section, Quasi Sliding Mode [39] and Asymptotic Sliding Mode [40] methodologies are used to increase the accuracy of the system and reduce chattering.

2.5.1 Quasi-Sliding Mode Control

In the quasi sliding mode control design, the sign function in Equation 2.24 is replaced by a continuous function to reduce the chattering. The quasi sliding mode behaves like a traditional sliding mode control outside of the boundary layer. In the boundary layer, continuous state feedback control is used instead of discrete state feedback control due to the intermittent switching function, effectively reducing chattering. However, the change in the controller might reduce the system accuracy. In quasi sliding mode, the continuous function emulating the signum function is given in Equation 2.25 [52] where ϵ is a small positive number.

$$sgn(\sigma) \approx \frac{\sigma}{|\sigma| + \epsilon} \quad (2.25)$$

In this concept, the input signal is updated as follows:

$$u = -cx_2 - Kx_1 - (\varphi) \frac{\sigma}{|\sigma| + \epsilon} \quad (2.26)$$

2.5.2 Asymptotic Sliding Mode

The derivative function approach is used in asymptotic sliding mode. In this case, the actual control signal (u) is continuous as it is integrated into the high-frequency switching signal. The asymptotic sliding mode can be obtained by applying four steps to the classical sliding mode method [53]:

Step 1: The auxiliary sliding variable s is defined using the sliding variable and its derivative. Also, the parameter \bar{c} is equal to the proportional gain parameter K .

$$s = \dot{\sigma} + \bar{c}\sigma \quad (2.27)$$

Step 2: According to the ideal sliding mode controller, the auxiliary sliding variable converges to zero in finite time. Therefore, the sliding variable and its derivative converge to zero.

$$s = \dot{\sigma} + \bar{c}\sigma = 0 \quad (\sigma, \dot{\sigma} \rightarrow 0) \quad (2.28)$$

Step 3: The sliding variable (Equations 2.27 and 2.28) approaches zero in finite time as a result of the derivative function. In this way, the disturbance effect is eliminated and the motion variables approach zero in the finite time.

$$\sigma = x_2 + cx_1 \rightarrow c > 0 \quad (2.29)$$

$$\dot{\sigma} = \dot{x}_2 + c\dot{x}_1 \quad (2.30)$$

Step 4: The derivative (ζ) of the control input signal is calculated using a similar approach in Equation 2.14 regarding the stability of the sliding mode and the cancellation of the bounded uncertainties.

$$\dot{u} = \zeta \quad (2.31)$$

$$\zeta = -c\bar{c}x_2 - (c + \bar{c})u - \zeta_1 \quad (2.32)$$

$$\zeta_1 = \varphi \operatorname{sgn}(s) \quad (2.33)$$

$$\varphi = \frac{\alpha}{\sqrt{2}} + \bar{F}_d + (c + \bar{c})F_d \quad (2.34)$$

$$\zeta = -c\bar{c}x_2 - (c + \bar{c})u - \varphi \operatorname{sgn}(s) \quad (2.35)$$

2.6 Performance Improvement Method

After examining the chattering reduction methods given above, some modifications have been applied to the controllers to improve the performance of the system. In this section, the Asymptotic Sliding Mode Control performance is tried to increase by using the Proportional Integral Asymptotic Sliding Mode Controller, which is a new controller type obtained within the scope of this thesis.

2.6.1 Proportional Integral Asymptotic Sliding Mode Control (PIASMC)

In the first step, the integral of the position is added to the sliding variable in Equation 2.36.

$$\sigma = x_2 + c_1x_1 + K \int x_1 dt \quad (2.36)$$

Then, the equation of the system is obtained by repeating 4 basic steps in the Asymptotic Sliding Mode controller.

$$s\dot{s} = s(u(c + \bar{c}) + f(x_2, t)(c + \bar{c}) + \zeta + f(\dot{x}_2, t) + (c\bar{c} + K)x_2 + \bar{c}Kx_1) \quad (2.37)$$

$$\zeta_1 = \zeta + u(c + \bar{c}) + (c\bar{c} + K)x_2 + \bar{c}Kx_1 \quad (2.38)$$

$$\zeta = -u(c + \bar{c}) - (c\bar{c} + K)x_2 - \bar{c}Kx_1 + \zeta_1 \quad (2.39)$$

$$s\dot{s} = s(\zeta_1 + f(x_2, t)(c + \bar{c}) + f(\dot{x}_2, t)) \leq s\zeta_1 + |s|(\bar{F}_d + (c + \bar{c})F_d) \quad (2.40)$$

$$\zeta = -u(c + \bar{c}) - (c\bar{c} + K)x_2 - \bar{c}Kx_1 - \varphi \text{sgn}(s) \quad (2.41)$$

Later, the same logic used in quasi sliding mode was applied here, and chattering was reduced at the same time. The derivative of the updated system control function was given in Equation 2.43.

$$\text{sgn}(s) \approx \frac{s}{|s| + \epsilon} \quad (2.42)$$

$$\zeta = -u(c + \bar{c}) - (c\bar{c} + K)x_2 - \bar{c}Kx_1 - \varphi \frac{s}{|s| + \epsilon} \quad (2.43)$$

The Derivative of the input signal in Equation 2.43 is used to find the input signal increment in Equation 2.44. In this way, the response of the input signal is obtained using the Euler approximation.

$$\Delta(u) = \zeta * \Delta t \quad (2.44)$$

$$u_{k+1} = u_k + \Delta(u) \quad (2.45)$$

$$u_{k+1} = \left(-u(c + \bar{c}) - (c\bar{c} + K)x_2 - \bar{c}Kx_1 - \varphi \frac{s}{|s| + \epsilon} \right) * \Delta t + u_k \quad (2.46)$$

2.7 Experimental Results

Using the experimental setup given in Figure 2.9, the performance of the proposed controllers in real-time was evaluated. The performance analysis was carried out by assuming that the catheter moves under the effect of bounded unknown friction force ($|F_d| > f(x_2, t)$).

2.7.1 Test setup

As an actuator for driving the active roller, the Dynamixel XM430-W350 type smart servo motor is exploited. The controller mode for the actuator is selected as the current control mode in which the controlled motor operates as a torque source. The proposed controllers are implemented using Python2.6 with the Robotic Operating System (ROS) [46] interface was designed using a computer which has a Ubuntu18.04 operating system.

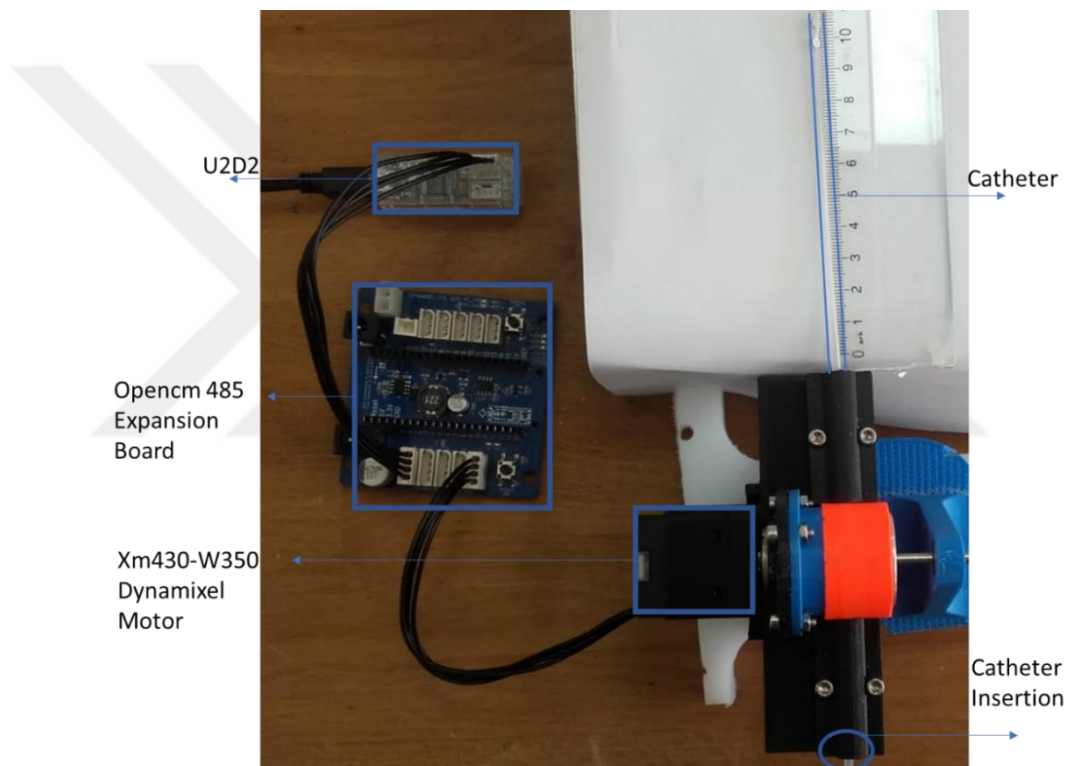


Figure 2.9: Frictional Catheter Driving System

2.7.2 The Controller Performance Tests

Performance tests were implemented to adjust the control parameters ϕ , c and K given in Table 2.1. Reference inputs for catheter tip advance position were given as 200mm and 5mm. During the test, the values of position, speed, and control signals were obtained. The rise time, MAE, overshoot, and steady-state value were calculated using

the recorded signals to determine the best-performing controller parameters. The MAE value was calculated between the desired value and the actual values, which are position values above 95% of the desired position value. In addition, reaching 95% of the desired position gives the system rise time performance. During the experiments, the upper limit of the unknown friction force was estimated for 1N and the switching gain (φ) was kept constant as 2. The set of controller parameters was obtained using the trial and error method is presented in Table 2.1.

Table 2.1: Sliding Mode Control Performance

SMC Type	c	K or \bar{c}	x_d	Transient Response		Accuracy	
				Rise Time (s)	Overshoot Value (mm)	Steady-state error (mm)	MAE Value
Classical	0.1	0.1	200	1.770	1.18	0.8	0.56
Quasi	0.05	0.3	200	1.740	5.80	0.03	0.18
Asymptotic	0.05	0.4	200	1.770	11.14	0.03	1.02
Classical	0.1	0.1	5	0.156	Not available	Oscillatory	0.80
Quasi	0.05	0.3	5	0.228	No overshoot	0.28	0.28
Asymptotic	0.05	0.4	5	0.432	Not available	Oscillatory	0.34

The first three rows of Table 2.1 show that all sliding mode controllers have underdamped responses when the reference is 200 mm. Control input and position signals obtained during the experiment are given in Figure 2.10. All catheter tip position signals appear to look similar. However, when the position signal reached a steady-state, high-magnitude chattering is observed in the classical and asymptotic sliding mode control signals in Figures 2.10a and 2.10e. Both controllers have a chattering size greater than the disturbance force limit. Also, it is observed that the quasi sliding mode controller compensates the disturbance force. As a result, the quasi sliding mode control chattering attenuation performance is better than the asymptotic sliding mode control. In the 5 mm reference performance test, chattering in the control signals of the classical and asymptotic sliding mode controllers (Figures 2.11 a, and e) is higher than quasi sliding mode(Figures 2.11 c).

In that conclusion, the quasi-sliding mode controller compensates the constant disturbance force. In addition, the quasi sliding mode controller has the best performance in terms of transient and steady-state performance, as seen in Table 2.1.

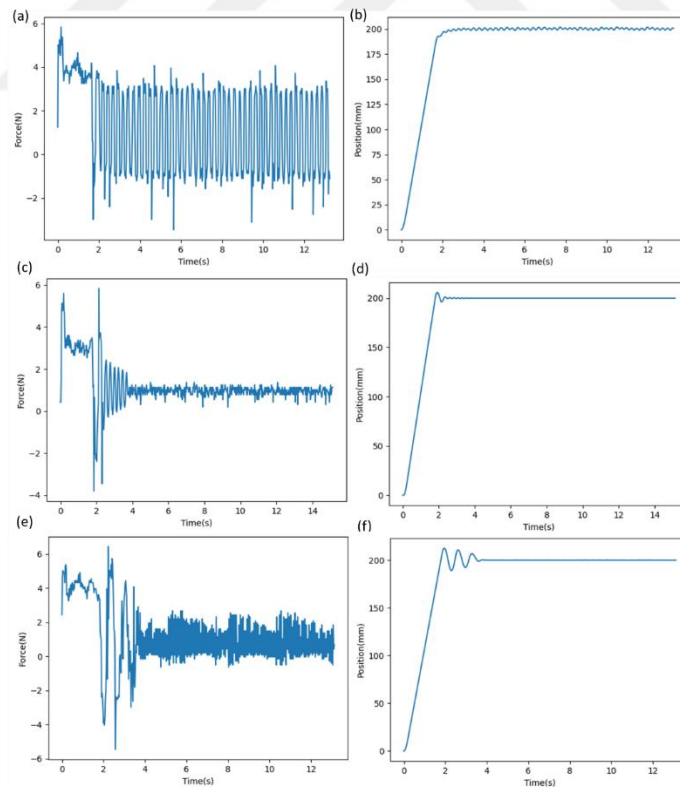


Figure 2.10: Sliding Mode Controller Control Actions and Position State Result When Goal Position 200 mm a-b) Classical Sliding Mode, c-d) Quasi Sliding Mode, e-f) Asymptotic Sliding Mode

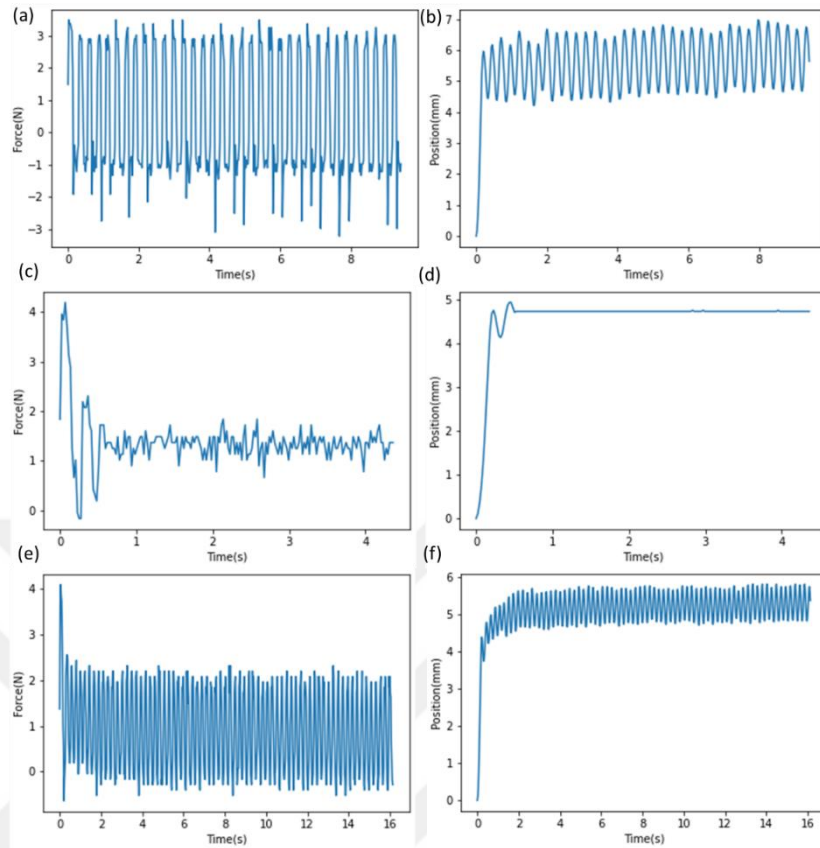


Figure 2.11: Sliding Mode Controller Control Actions and Position State Result When Goal Position 5 mm a-b) Classical Sliding Mode, c-d) Quasi Sliding Mode, e-f) Asymptotic Sliding Mode

2.7.3 Controller Improvement

As mentioned earlier, for better guidance strategy chattering signal must be limited instead of eliminated. In that conclusion, the sliding mode controller chattering signal is limited using changing disturbance signal. The selected controller should not lose its stability and accuracy performance under changing disturbance signals. In that conclusion, a better robust controller type is chosen against the changing disturbance signal.

The asymptotic sliding mode is the most effective controller against changing disturbance signals due to the derivative effect on the controller. For this reason,

controller accuracy performance was increased by combining the proportional-integral controller and quasi sliding mode controller to the Asymptotic sliding mode controller.

In that conclusion, a novel sliding mode controller was designed and added to the system which is a proportional-integral asymptotic sliding mode. For the catheter tip position, reference positions are chosen 100mm. Position, speed, and control signals were recorded during the test. During the experiments, it was estimated 1N is the upper limit of the unknown disturbance force and the disturbance signal is changed by applying a 0.25Hz sinusoidal signal. Controller performance is given in Figure 2.12.

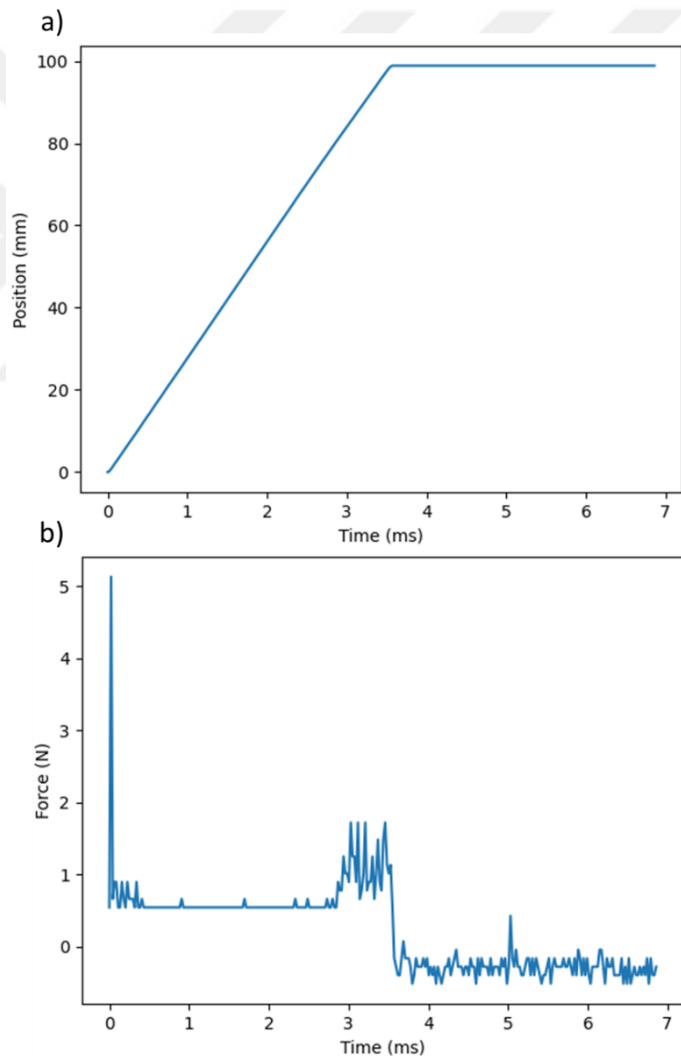


Figure 2.12: Proportional Integral Asymptotic Sliding Mode a) Position State Result
b) Actions State Result

When Figure 2.12 is examined, it is understood that the Proportional Integral Asymptotic Sliding mode performance value is better than other controllers. First, this new controller has high accuracy. Second, there is no overshoot in the controller and controller chattering performance is lower than other controllers.



Chapter 3

Catheter Guidance System

In this section, the design of the permanent magnet actuator system, the guidance strategy and the results of the guidance system were presented.

3.1 Permanent Magnet Actuator

Firstly, 2D modeled bronchial was considered as the working environment of the catheter system [54]. A magnetic actuator system was designed to guide the catheter in the working area. In the design process, the characteristics and number of permanent magnets inside the catheter were determined [10]. Then, the equations of magnetic actuators were examined for creating a magnetic force on the small particle. The Finite Element Analysis was carried out based on magnetostatic theory. In the Finite Element Analysis, the structure and layout of the poles of the magnetic actuators were determined. In the analysis, the magnetic field size of the system and the structural and functional parameters of the magnetic actuator system were determined.

3.1.1 Characteristics of the Permanent Magnet Inside the Catheter

In this study, the small particle inside the catheter is a cylindrical N35 type magnet with a 1.5 mm radius and 1.5 mm height. Neodymium magnets are permanent magnets composed of an alloy of neodymium, iron, and boron to achieve a tetragonal crystal structure [55, 56]. The neodymium magnets are generally used because they have high magnetization under magnetic fields [55].

3.2 Catheter Guidance

In this section, the design of the magnetic actuation system, which performs to bend the catheter at a certain angle, was presented.

3.2.1 Magnetic Guidance via Permanent Magnet Actuator

The magnetization vector of the small particle inside the catheter and the magnetic field vector generated by the magnetic actuator exert a magnetic torque to bend the catheter. The magnetic torque and force acting on a permanent magnet with magnetization vector \vec{M} under magnetic fields are given in Equations 3.1 and 3.2 [18, 57]. In the equations, \vec{B} is the magnetic flux density and $\vec{\nabla B}$ is the gradient of the magnetic flux density.

$$\vec{F}_{pm} = (\vec{M} \cdot \vec{\nabla})\vec{B} \quad (3.1)$$

$$\vec{\tau}_{pm} = \vec{M} \times \vec{B} \quad (3.2)$$

The vectorial components of the magnetic force equation are given in Equations 3.3, 3.4, 3.5 and 3.6. In the equations, B_y is the Y-axis component of the magnetic flux density, B_x is the X-axis component of the magnetic flux density and B_z is the Z-axis component of the magnetic flux density.

$$\vec{F}_{pm} = (\vec{M} \cdot \vec{\nabla})\vec{B} = \left(M_x \frac{\partial}{\partial x} + M_y \frac{\partial}{\partial y} + M_z \frac{\partial}{\partial z} \right) (B_x \vec{i} + B_y \vec{j} + B_z \vec{k}) \quad (3.3)$$

$$F_{pm,x} = M_x \frac{\partial B_x}{\partial x} + M_y \frac{\partial B_x}{\partial y} + M_z \frac{\partial B_x}{\partial z} \quad (3.4)$$

$$F_{pm,y} = M_x \frac{\partial B_y}{\partial x} + M_y \frac{\partial B_y}{\partial y} + M_z \frac{\partial B_y}{\partial z} \quad (3.5)$$

$$F_{pm,z} = M_x \frac{\partial B_z}{\partial x} + M_y \frac{\partial B_z}{\partial y} + M_z \frac{\partial B_z}{\partial z} \quad (3.6)$$

3.2.2 The Force Required for Bending the Catheter

In this section, the minimum amount of force required to bend the catheter is calculated. For this, the catheter is assumed as a Cantilever Beam [42, 58, 59]. Young's modulus and second moment of inertia are obtained to find the amount of force required to bend the catheter. The second moment of inertia is found by using Equation 3.7 [60]. In the equation, the outer radius of the hollow cylinder is r_o and the inner radius of the hollow cylinder is r_i .

$$I = \frac{\pi}{4}(r_o^4 - r_i^4) \quad (3.7)$$

3.2.2.1 Young Modulus Experiment

In this section, the amount of elongation in the catheter was examined by applying a certain amount of pulling force to the catheter. In this way, the catheter young modulus value was obtained by founding the tensile stress and strain value. The tensile stress (σ_t) and strain (ϵ_t) values of the catheter were found by using Equations 3.8 and 3.9 [61]. In the experiment, the object weight was 100 grams and fixed to the bottom of the catheter using a hook system. Then, the elongation of the catheter was measured with a ruler. At the end of this process, stress and strain values were obtained. The stress value was found as 318471Pa and the strain value was found as 7.

$$\sigma_t = \frac{F_a}{A} \quad (3.8)$$

$$\epsilon_t = \frac{\Delta L}{L_0} \quad (3.9)$$

Young's modulus value of the catheter material was obtained by dividing the tensile stress value to the strain value (Equation 3.10). Young modulus value was found as 2234903Pa.

$$E = \frac{\sigma_t}{\epsilon_t} \quad (3.10)$$

Then, the bending of the catheter was found using this information. The slope (α) and deflection (δ) states formed by applying the P force to the cantilever beam was shown in Figure 3.1.

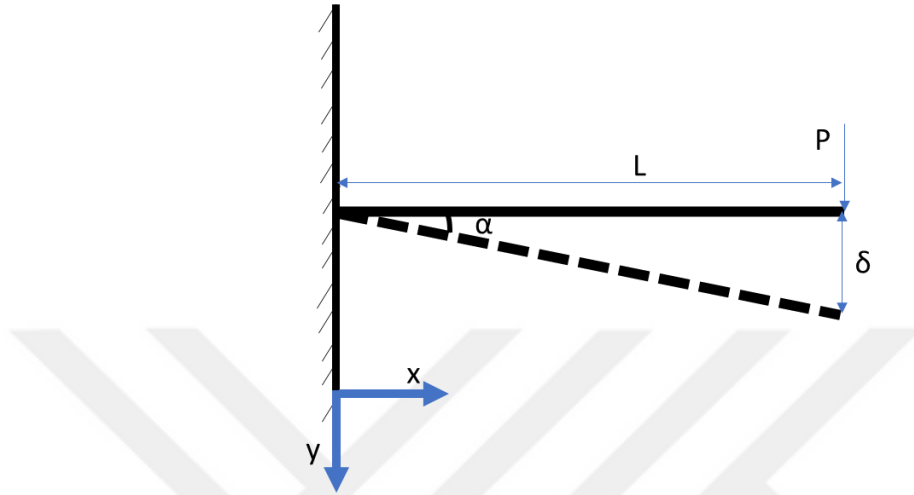


Figure 3.1: Simple Cantilever Beam Schematic

First, the catheter bending force was found. It was seen in the Equation 3.11 and 3.12 the required amount of force is 0.05 N.

$$M = \frac{\sigma I}{r_o} \quad (3.11)$$

$$P = \frac{M}{L} \quad (3.12)$$

The slope and deflection value was found in Equations 3.13 and 3.14.

$$\alpha = \frac{PL^2}{2EI} \quad (3.13)$$

$$\delta = \frac{PL^3}{3EI} \quad (3.14)$$

However, the working environment includes a frictional plane. Also, the friction force increases with the advancement of the catheter must be taken into account.

It is assumed that the catheter is bent a maximum of 150 degrees in the working area. The required catheter bent force is found 0.2 N using Equation 3.13. In addition, the friction force must be taken into account. In that conclusion, the expected magnetic force of the system must be higher than 0.25N. Also, it is found that a 10 cm long catheter can be bent up to 170 degrees by using the obtained force.

3.3 Permanent Magnet Actuator System Design

In this section, the magnetic actuator system design that provides the required magnetic force for the catheter bend was discussed. As a result of the preliminary studies, it was decided to design the magnetic actuator system depending on certain structural parameters. For this purpose, the size of the large permanent magnet is determined. In the Equations 3.15 to 3.18 were given magnetic fields produced by permanent magnets depending on their types and distances [62].

In the Equation 3.15 B_r is remanence magnetic field, z is a distance from a pole face on the symmetry axis, L is the length, W is the width and D is the height of the block magnet. In the Figure 3.2a represent a block magnet shape.

$$B = \frac{B_r}{\pi} \left[\arctan \left(\frac{LW}{2z\sqrt{4z^2+L^2+W^2}} \right) - \arctan \left(\frac{LW}{2(d+z)\sqrt{4(D+z)^2+L^2+W^2}} \right) \right] \quad (3.15)$$

In the Equation 3.16 B_r is remanence magnetic field, z is a distance from a pole face on the symmetry axis, R is the radius and D is the height of the cylinder magnet. In the Figure 3.2b represent a cylinder magnet shape.

$$B = \frac{B_r}{2} \left[\frac{D+z}{\sqrt{R^2+(D+z)^2}} - \frac{z}{\sqrt{R^2+z^2}} \right] \quad (3.16)$$

In the Equation 3.17 B_r is remanence magnetic field, z is a distance from a pole face on the symmetry axis, R_a is the outer radius, R_i is the inner radius, and D is the height of a ring magnet. In the Figure 3.2c represent the ring magnet shape.

$$B = \frac{B_r}{2} \left[\frac{D+z}{\sqrt{R_a^2+(D+z)^2}} - \frac{z}{\sqrt{R_a^2+z^2}} - \left(\frac{D+z}{\sqrt{R_i^2+(D+z)^2}} - \frac{z}{\sqrt{R_i^2+z^2}} \right) \right] \quad (3.17)$$

In the Equation 3.18 B_r is remanence magnetic field, z is a distance from a pole face on the symmetry axis and R radius of a sphere magnet. In the Figure 3.2d represent the sphere magnet shape.

$$B = B_r \frac{2}{3} \frac{R^3}{(R+z)^3} \quad (3.18)$$

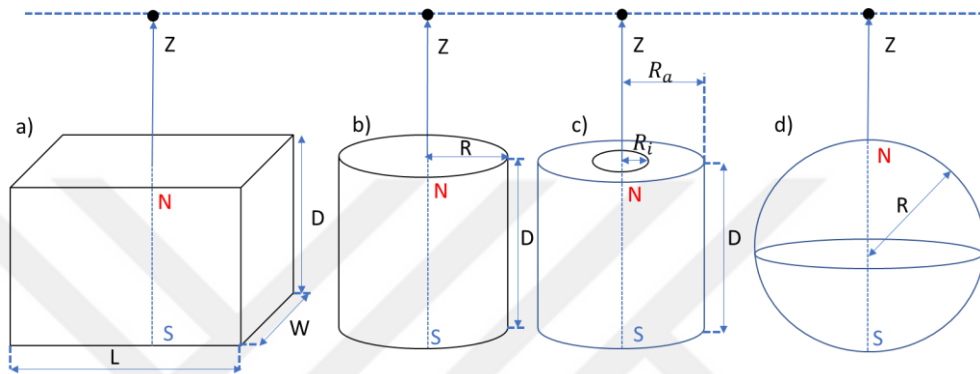


Figure 3.2: a) Block Magnet Representation b) Cylindrical Magnet Representation c) Ring Magnet Representation d) Spherical Magnet Representation

The block magnet type produces more magnetic fields when the D , L , W and $2R$ variables are the same for all magnets. The magnets were combined, to increase the pulling force. The desired magnetic force value was found by using finite element analysis.

3.4 Finite Element Analysis for Permanent Magnets

The finite element methods provide mathematical solutions by simplifying engineering problems. Finite element analysis is used in many engineering applications [63–65]. In this study, the magnetic force produced by a magnet depending on its position and magnet geometry is found by using finite element analysis. The Comsol Multiphysics program is used for this process. Some steps have been followed when using the Comsol program [66].

At first, the system dimension was selected. In the Equation 3.3 F_x , F_y , and F_z components of the magnetic force were needed. For that reason, 3-dimensional analysis was selected. Then, Magnetic Field (mf) was selected in the Physics section. Then the Stationary was selected for the study. After this process, the design of the system was started in the geometry section.

3.4.1 Finite Element Analysis for a Single Permanent Magnet

In the geometry section, the dimensions of a magnet are entered by selecting the cube. The dimensions of the magnet in Figure 3.3b are given. Magnet size is chosen as $20 \times 20 \times 20 \text{ mm}^3$. After the single magnet is designed, an air sphere is designed outside of the system (Figure 3.3 a). The size of the air sphere should not be chosen too large because the number of mesh elements increases the computational cost and effect the solution accuracy.

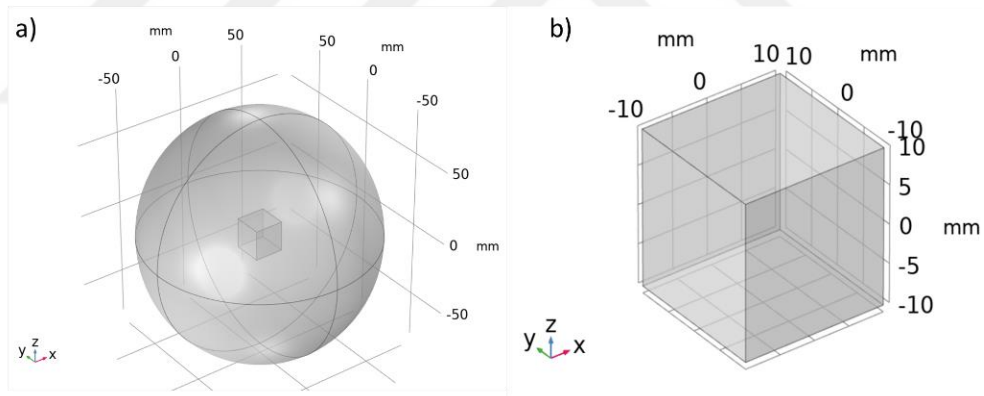


Figure 3.3: Geometric View Of a) All System, b) Single Magnet System

Later materials were selected. The air was selected for the sphere, and the default permanent magnet was selected for the cube. The magnet relative permeability value was entered into the material section. Then the meshes of the system were selected. Increasing the number of meshes in this part depends on their similarity in the analysis results. First, meshes of different sizes are appointed. After that, obtained results were compared depending on the mean absolute error value which is found between them. When the results give similar values regardless of the mesh, the appropriate mesh

range was selected. Thanks to mesh comparison analysis, the optimum size of the air sphere was found. Magnetic field values depending on the mesh numbers were given in Figure 3.4.

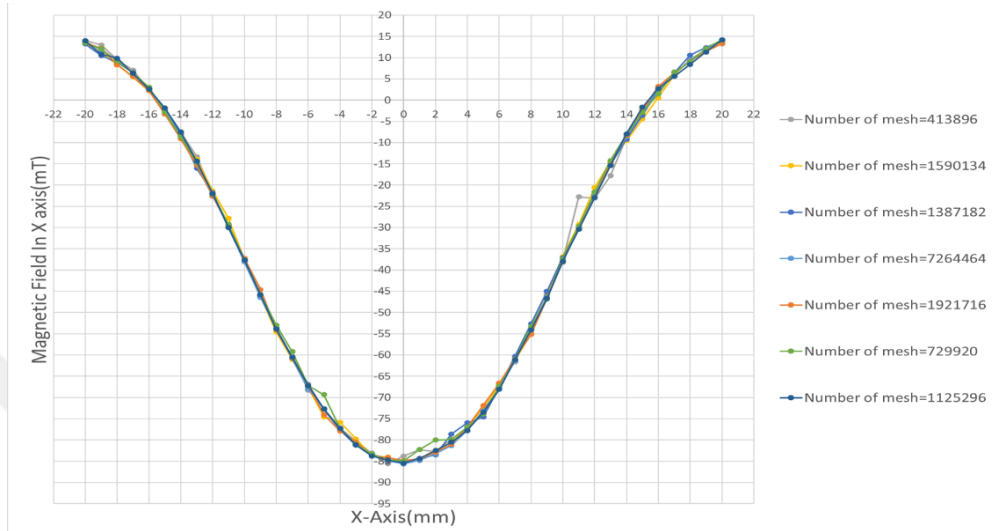


Figure 3.4: Magnetic Field X-axis Values Dependent On Number of Mesh

A mesh view of the Comsol program was given in Figure 3.5. In the figure, a total of 1125296 mesh values were appointed.

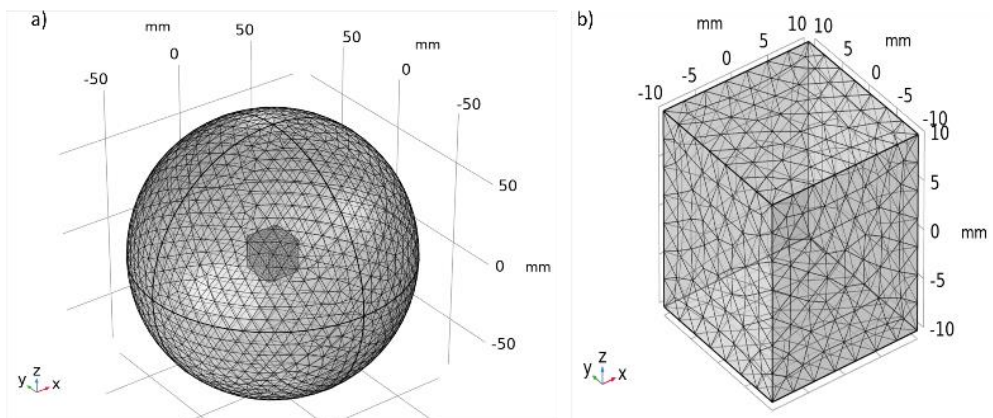


Figure 3.5: Mesh View of a) All System, b) Single Magnet System

In the Comsol study section, Ampere's law was selected for the magnets and the Remanent Flux Density values of the magnets and the polarization direction of the magnet was determined. Finally, when all the steps are finished, the program is compiled. Then, the obtained results were analyzed. In the examination section, the magnetic flux density norm was selected for the expression section and the magnetic field values produced by the magnet were examined. It can be seen, in Figure 3.6, the norm of the magnetic flux density is between 0 and 100 mT.

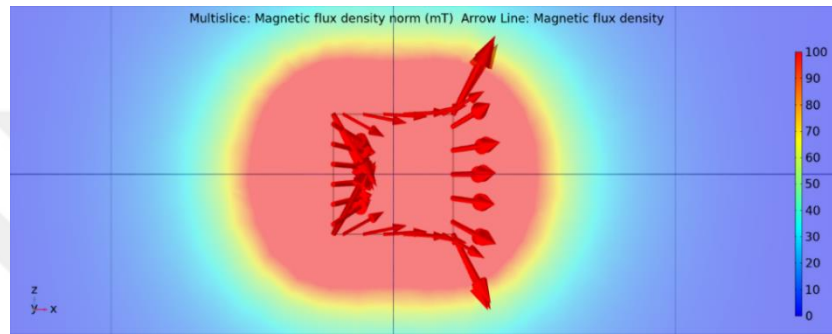


Figure 3.6: Magnetic Flux Density Norm

To calculate the gradient of the magnetic field, the magnetic field values are collected in a coordinate base with dimensions of a rectangular cube. For this process, two separate data grid sets were created. In the first data set, the x-axis was fixed at 15mm because of the distance between the magnet and the tip of the catheter at 5mm. Then, the z-axis was collected at intervals of 2 mm from -20mm to 20mm. Finally, the -10, 0, and 10 Y-axis values were added to all data points. For the second data set, the x-axis was collected at 1mm intervals from 15mm to 35mm. Then, -10, 0, and 10 values were selected as the Z-axis. Finally, on the Y-axis, the origin point was assigned. In Figure 3.8, the dimensions of the data surface were given.

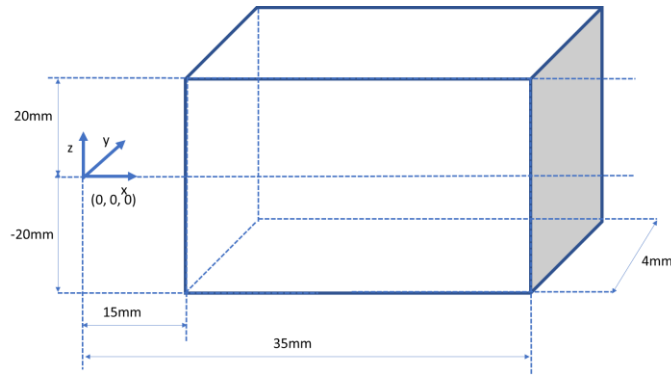


Figure 3.7: Coordinate Grid Values

Then, depending on the coordinate points extracted in the export part, the desired magnetic field values were obtained.

3.4.2 Calculating Magnetic Force Values of a Single Magnet

By using two coordinate data sets extracted with a single magnet, magnetic field values in the specified study area were collected. In the scope of the studies, it was thought that the north pole of the magnetic particle placed inside the catheter was in the +x direction and the north pole of the permanent magnet was chosen as +x direction. In this way, the catheter was pulled by the permanent magnet. Magnetic force values and vectorial directions were calculated. The magnetic force value and magnetic force directions produced in the x and z planes of the designed single magnet were shown in Figures 3.8 and 3.9.

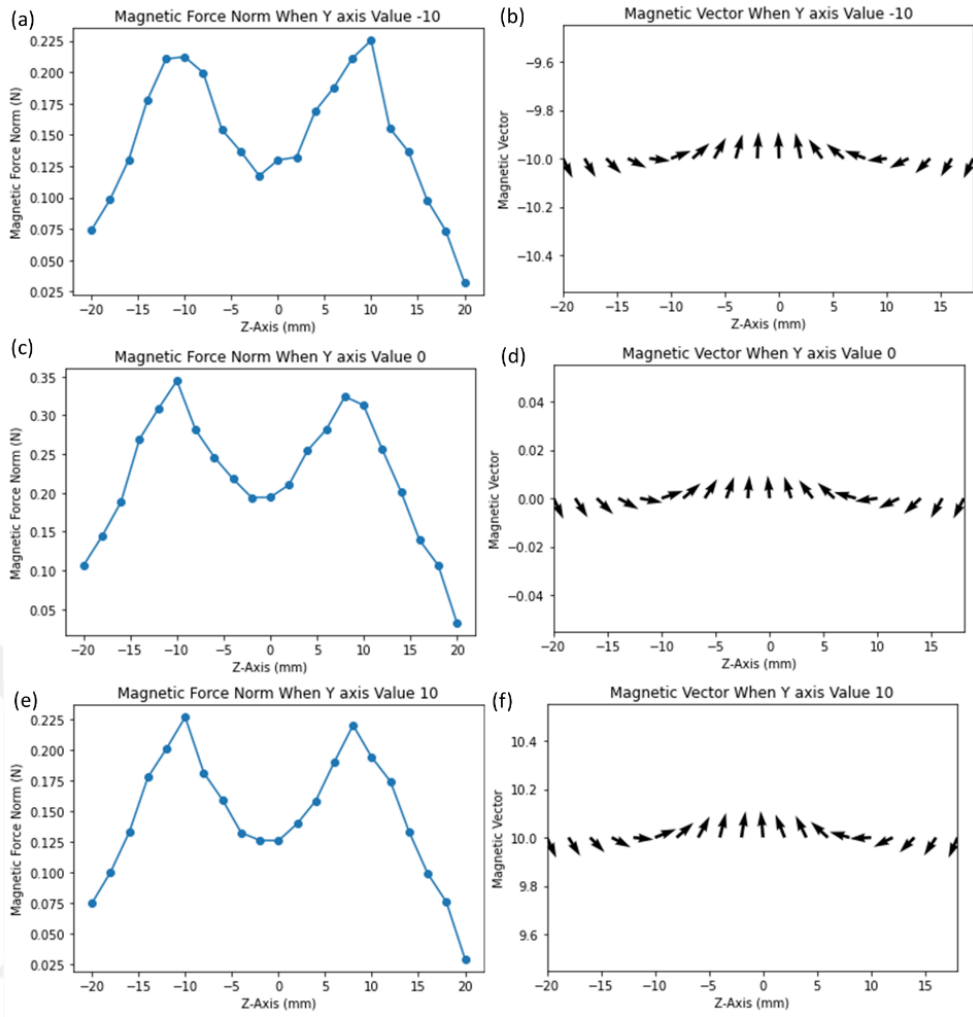


Figure 3.8: Magnetic Effect on Different Y-axis Values in X and Z Planes a-c-e) Magnetic Force Magnitudes, b-d-f) Magnetic Force Vector Direction

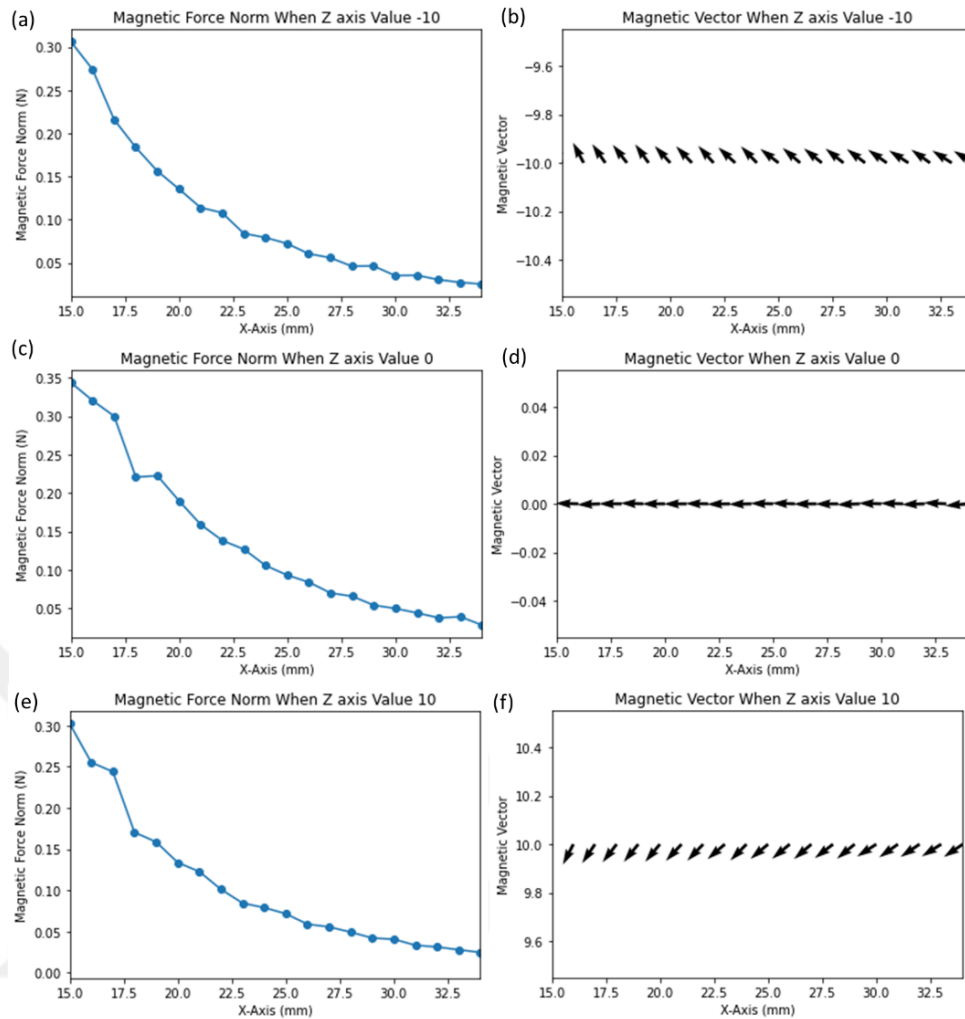


Figure 3.9: Magnetic Effect on Different Z-axis Values in X and Z Planes a-c-e) Magnetic Force Magnitudes, b-d-f) Magnetic Force Vector Direction

3.4.3 Finite Element Analysis for Double Magnet System

After examining the above analytical results, an additional magnet with the same size was added and the same steps were repeated. The dimensions of the permanent magnet and the air cube are given in Figure 3.10. The dimension of the double magnet was a $20 \times 20 \times 40 \text{ mm}^3$.

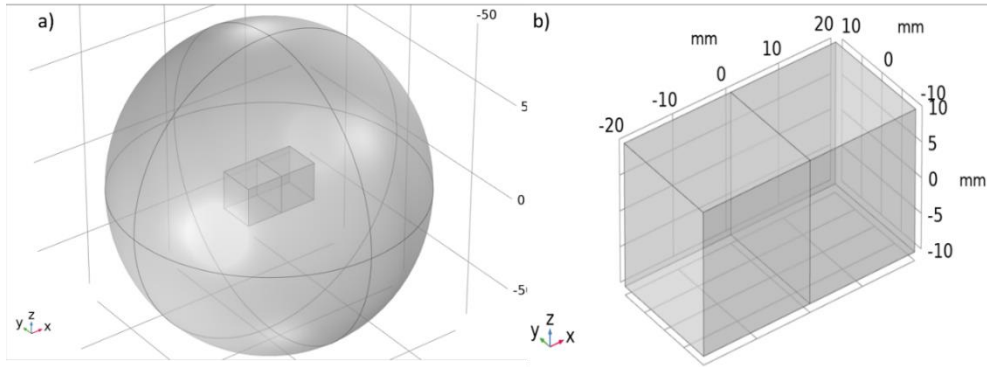


Figure 3.10: Geometric View of a) All System, b) Double Magnet System

A mesh view of Comsol is given in Figure 3.11. In the figure, a total of 1157356 mesh values were appointed.

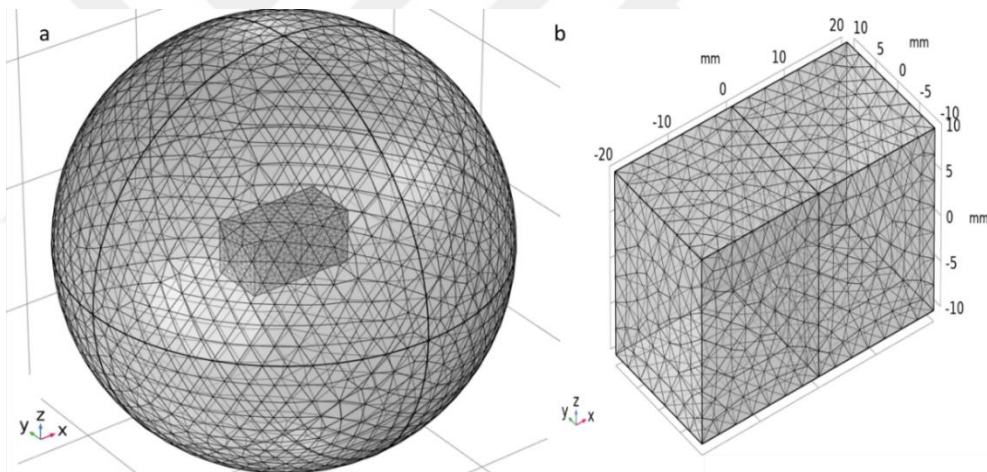


Figure 3.11: Mesh View of a) All System, b) Double Magnet System

In Figure 3.12, the norm of the magnetic flux density of the permanent magnet was between 0 and 100 mT, and the color chart and the representation of the magnetic field lines were given.

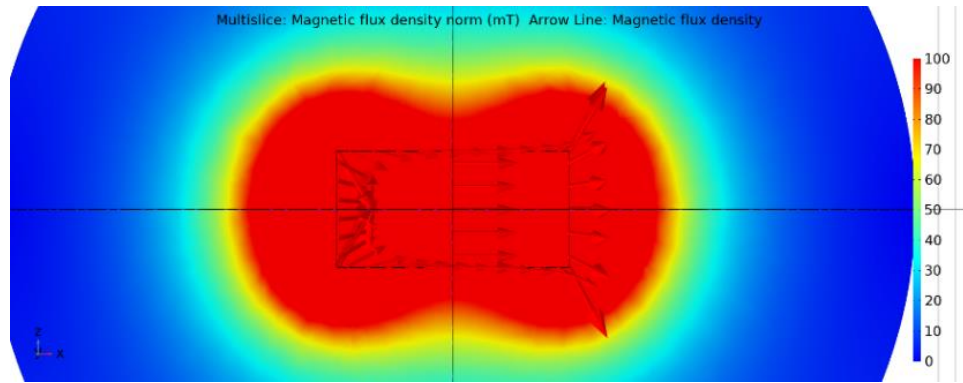


Figure 3.12: Magnetic Flux Density Norm

3.4.4 Calculating Magnetic Force Values of Double Magnet System

The working area of a double magnet was the same as a single magnet. The magnetic force value and magnetic force directions produced in the x and z planes of the designed double magnet were shown in Figures 3.13 and 3.14.

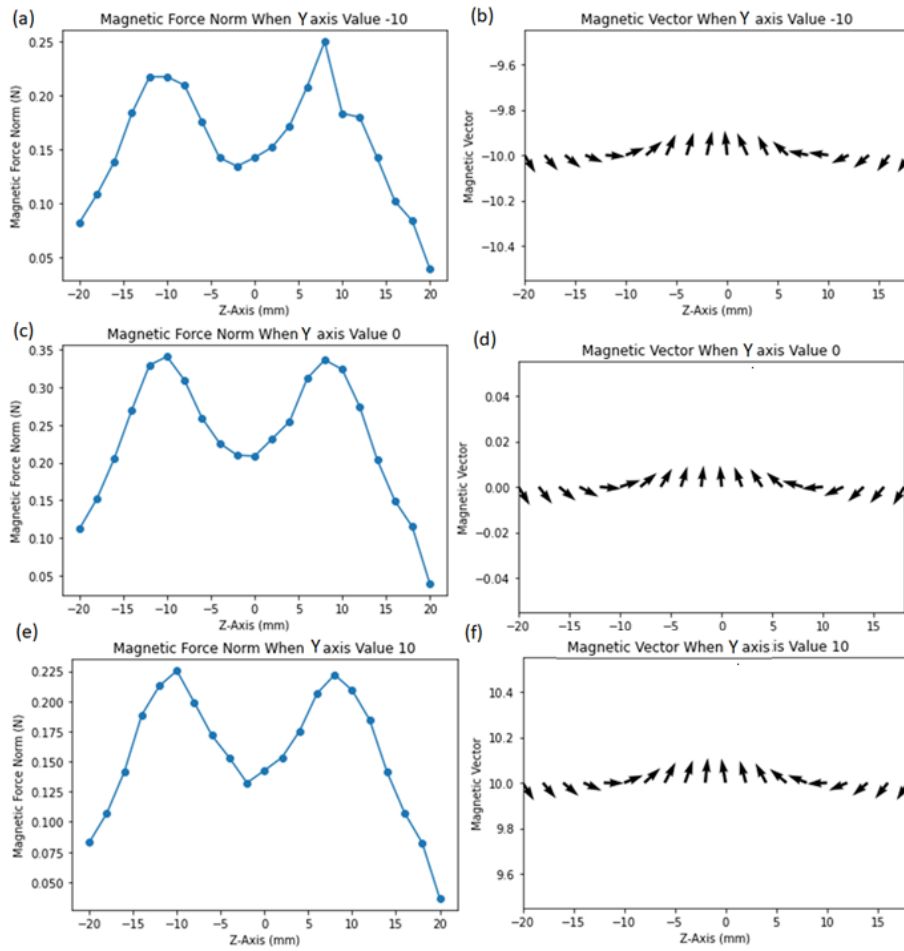


Figure 3.13: Magnet Effect on Different Y-axis Values in X and Z Planes a-c-e) Magnetic Force Magnitudes, b-d-f) Magnetic Force Vector Direction

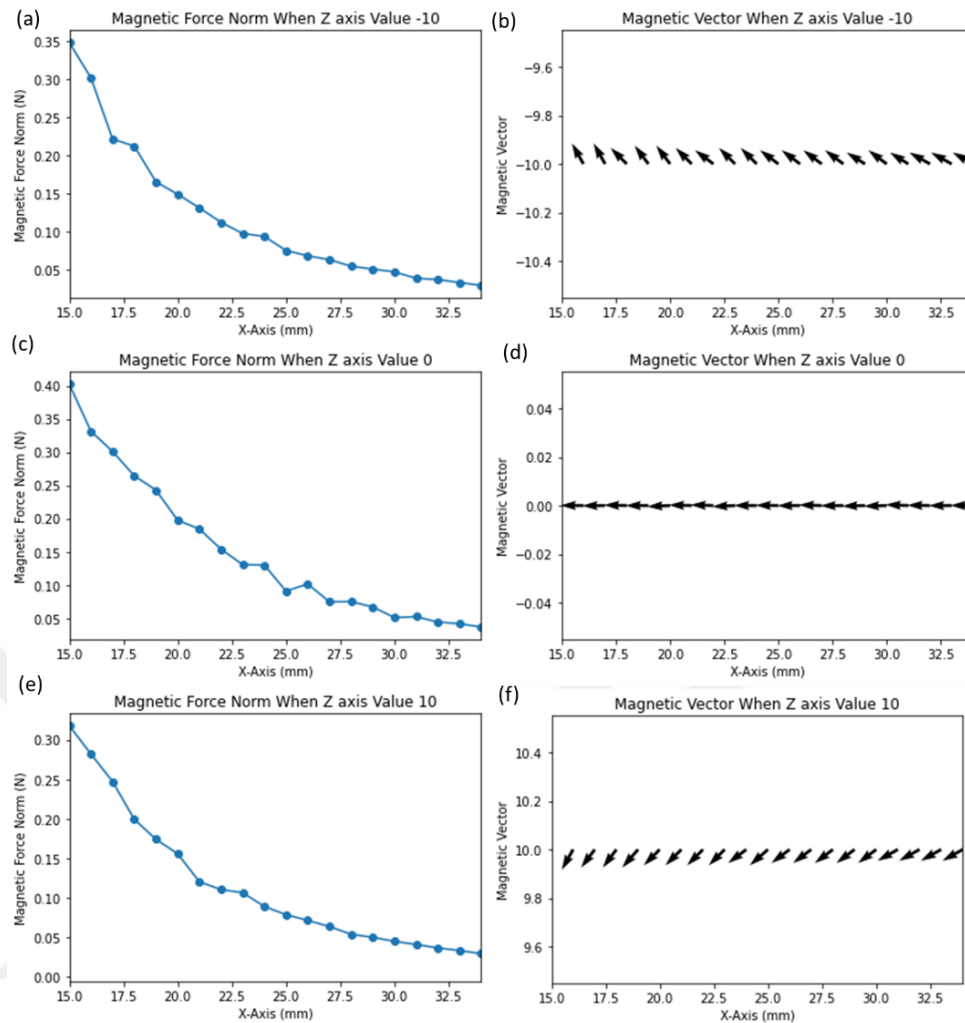


Figure 3.14: Magnet Effect on Different Z-axis Values in X and Z Planes a-c-e) Magnetic Force Magnitudes, b-d-f) Magnetic Force Vector Direction

3.4.5 Finite Element Analysis for Triple Magnet System

After examining the above analysis results, an additional magnet of the same dimensions was added and the same steps were repeated. The dimensions of the permanent magnet and the air cube were given in Figure 3.15. The dimension of the triple magnet was a $20 \times 20 \times 60 \text{ mm}^3$.

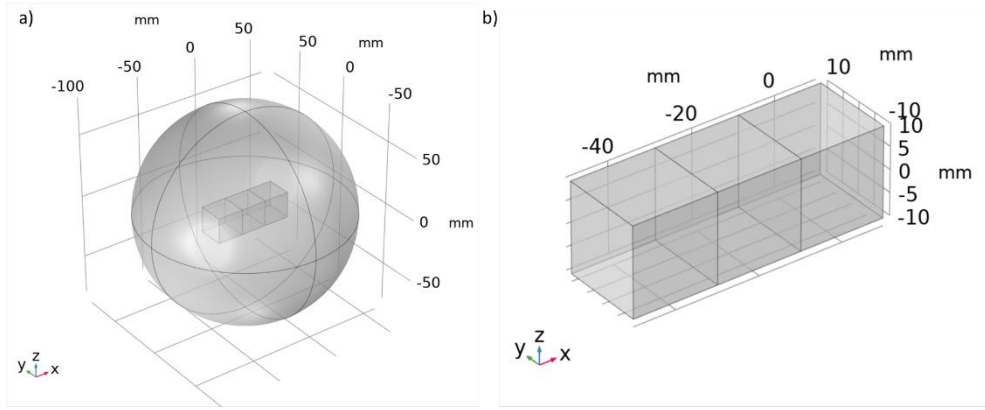


Figure 3.15: Geometric View of a) All System, b) Triple Magnet System

A mesh view of Comsol is given in Figure 3.16. In the figure, a total of 2068376 number of mesh were appointed.

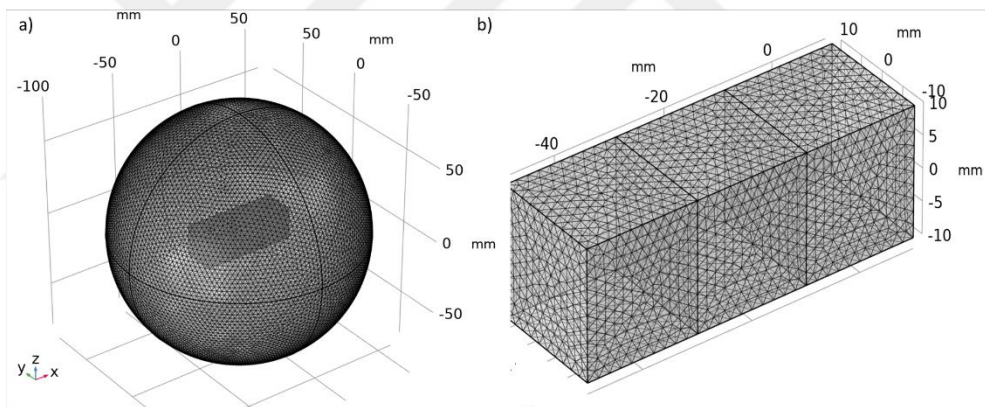


Figure 3.16: Mesh View of a) All System, b) Triple Magnet System

In Figure 3.17, the norm of the magnetic flux density of the permanent magnet was between 0 and 100 mT, and the color chart and the representation of the magnetic field lines were given.

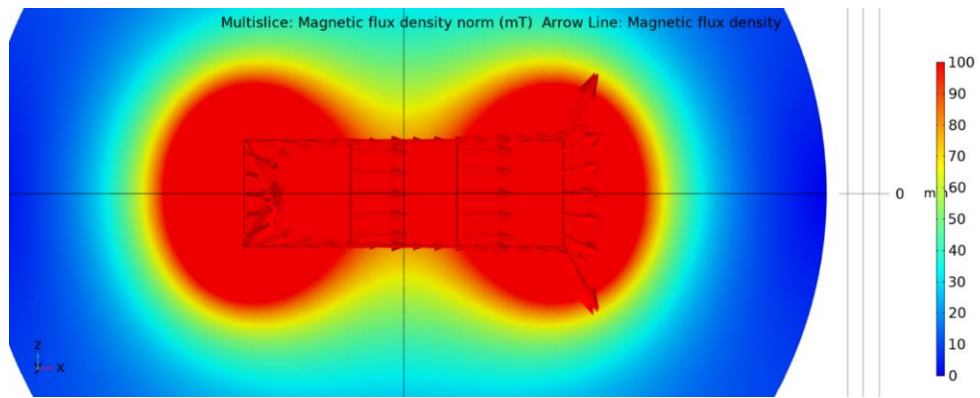


Figure 3.17: Magnetic Flux Density Norm

3.4.6 Calculating Magnetic Force Values of Triple Magnet System

The magnetic force value and magnetic force directions produced in the x and z planes of the designed double magnet were shown in Figures 3.18, and 3.19.

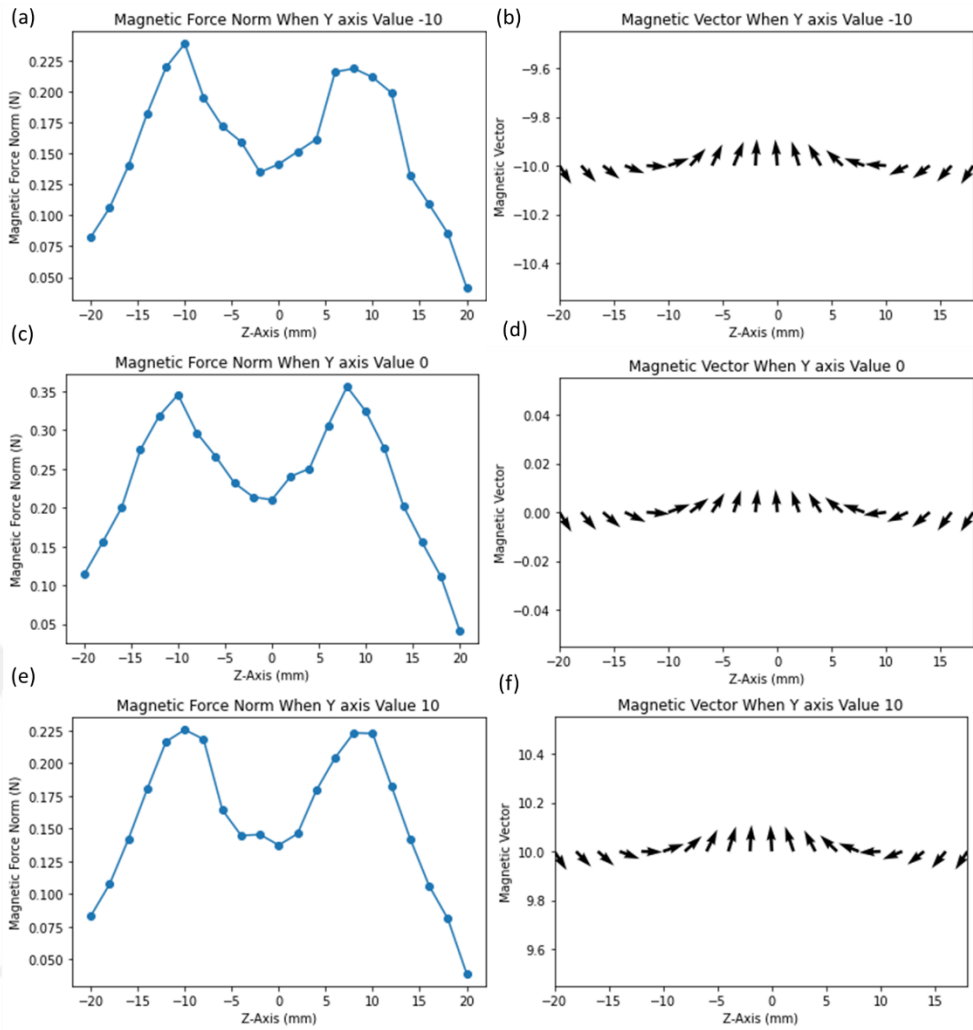


Figure 3.18: Magnet Effect on Different Y-axis Values in X and Z Planes a-c-e) Magnetic Force Magnitudes, b-d-f) Magnetic Force Vector Direction

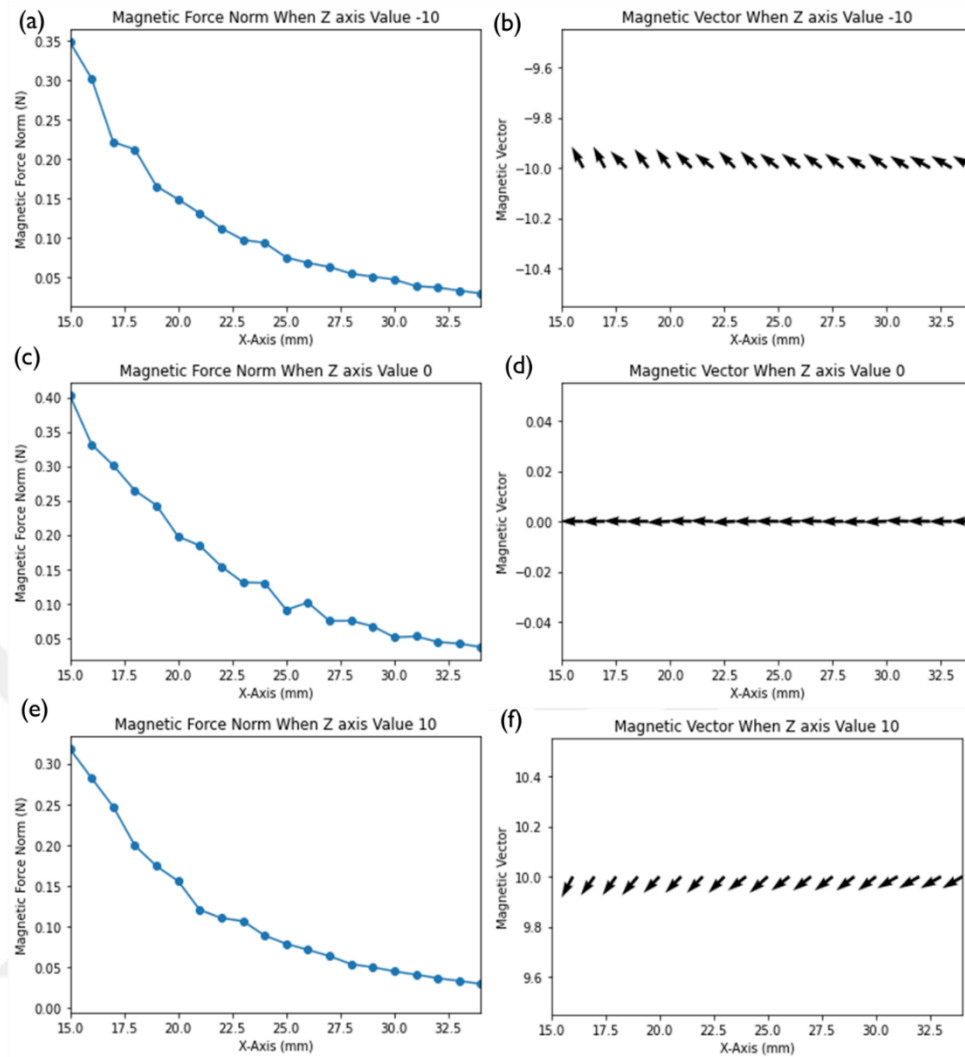


Figure 3.19: Magnet Effect on Different Z-axis Values in X and Z Planes a-c-e) Magnetic Force Magnitudes, b-d-f) Magnetic Force Vector Direction

As a result of the finite element analysis, extending the size of the magnet increases the value on the x-axis of the magnetic field. When Figures 3.18 and 3.19 were examined, it was sufficient to use a maximum of three magnets for our system, since it meets the required 0.25 N force in any case, to bend the catheter.

3.5 Guidance Strategy

During the bend of the catheter system, the polarities of the permanent magnets and the small particle placed inside the catheter were kept in reverse to pull each other.

Then, it was ensured that the catheter was pulled under the permanent magnet by magnetic force.

3.6 Guidance Results

In this part, a test was performed to measure the amount of bending of the catheter depending on the movement of the magnet drive system. First of all, the magnet drive system was designed. Then, the relationship between the graph and table results of the magnet movement and the bend of the catheter was examined.

3.6.1 Experimental Setup

The magnet movement system was responsible for guiding the catheter and it is ensured that it moves synchronously with the catheter drive system. The design of the magnet drive mechanism consists of 2 prismatic systems connected in series. Screw shaft and belt pulley system were used for the motion system. The nut bearings allow the slide to move in the Y-axis of 4 mm with 1 turn of the screw shaft. In the X-axis movement, the system moves with the motion of the screw connected to the double belt pulley system.

Stepper motors were permanent magnet pole motors that produce analog rotational movement output against the pulse signals applied to the input and provide this rotational movement step by step and with very precise control [67]. The polarity of the poles was changed using electronic switches. The speed of the motor was controlled by changing the operating frequency of the signals to be applied to the motor. The direction of rotation of the stepper motors can be clockwise (CW) or counterclockwise (CCW) by changing the order of the applied signals. The motion diagram and assembly of the system are shown in Figure 3.20.

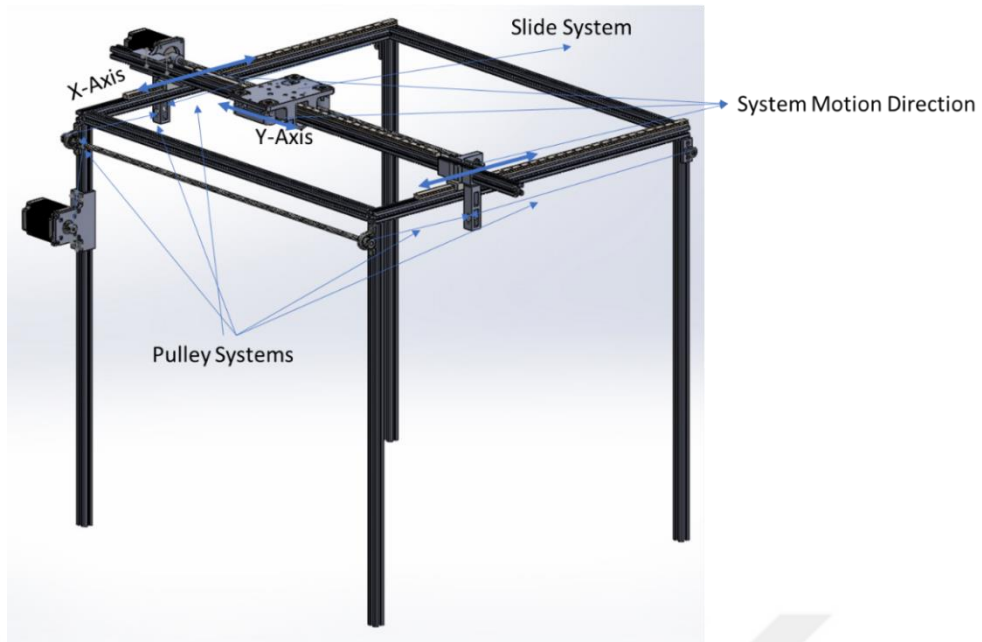


Figure 3.20: Magnet Motion System

3.6.2 Test Results

In this part, a triple magnet with the dimensions of $20 \times 20 \times 60 \text{ mm}^3$ connected to the slide part of the system. Afterwards, the catheter was pulled to a distance of 100 mm and placed directly under the magnet system. In this test setup, the relationship between the amount of bend of the catheter and the movement of the magnet motion system was examined. The left corner of the working area was accepted as the origin and the experiment was started at a 52.7 mm distance from the system. The motion of the system and the bending angle of the catheter were given in Figure 3.21. Afterwards, values were given in Table 3.1.

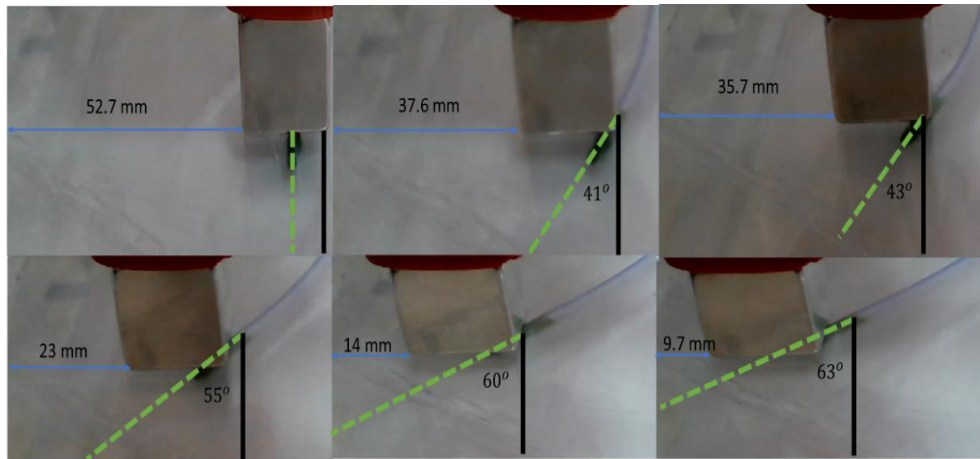


Figure 3.21: Magnet Position and Catheter Bending Angle

Table 3.1: Magnet Distance to Rotation Angle

Magnet Distance (mm)	52.7 mm	37.6 mm	35.7 mm	23 mm	14 mm	9.7 mm
Catheter Angle (Degree)	0°	41°	43°	55°	60°	63°

After examining the values in the Table 3.1, the relation between the magnet distance and the catheter angle was found by using the curve-fitting method. In Figure 3.22, magnet distance and angle graph were given. Also, the curve-fitting equation was given in the graph.

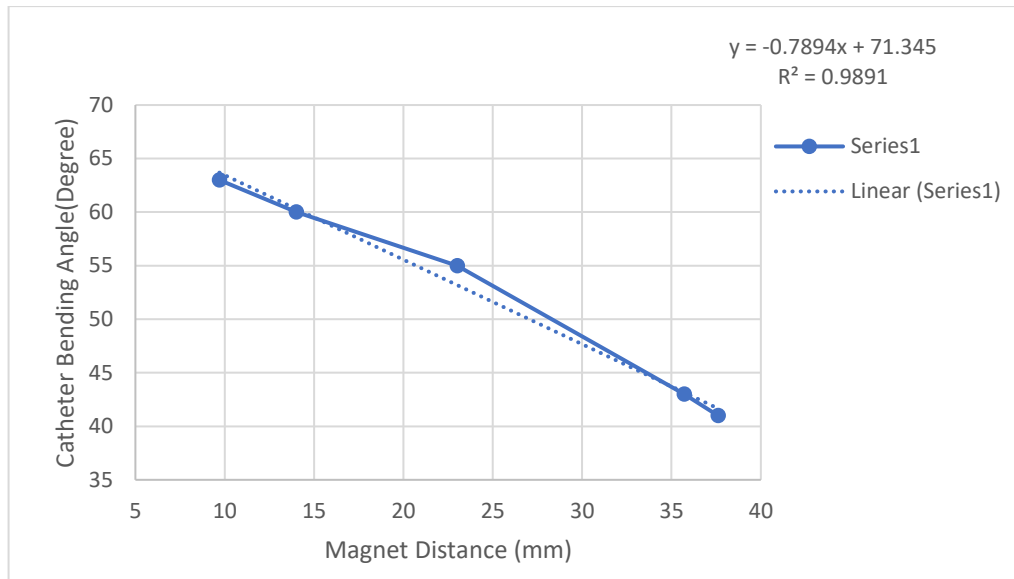


Figure 3.22: Magnet Distance and Catheter Angle Relation

In the curve-fitting process, the initial point was not taken into account. At the end of the procedure, it was learned that there is a linear relation between magnet distance and catheter bending angle.

Chapter 4

Machine Vision Feedback

One of the most important parts of the automatic control of catheters is machine vision [41, 68, 69]. The position of the catheter is obtained by a camera image since the working area is curved. The camera pixel has a 0.6 mm precision in the working area. The image processing method is used to find the position of the catheter. Also, the camera image is used to select the desired position value on the environment. In addition, the operator was used the camera system to monitor the environment.

4.1 Machine Vision

Image processing is a method used to digitize the image of the data with digital signal processing and obtain information on the data [70]. In image processing applications, the use of preprocessing methods is preferred to simplify the analysis of the image. These methods consist of, removing or reducing noise, determining the shape, color, and position of the object. These methods simplify and facilitate image processing applications and reduce processor time. Different preprocessing methods are applied according to the application and the used hardware.

Different methods are followed for applications that can be made with a motion camera and fixed camera [71]. Problems in object tracking and detection applications in fixed cameras are usually caused by light changes, camera vibrations, and environmental noise. In applications with moving cameras, in addition to the problems encountered in applications with fixed cameras, changes in the background due to camera movement and increase in processor load [71].

Camera systems do not directly learn the position of the target object. For this, some features of the target object are followed. Accordingly, various filter processes are

applied based on the shape, edges, colors, or corner points of the target object. In this the following steps are applied: Obtaining the digital image, identifying the target in the image, reducing the noise in the resulting image, obtaining the position information of the target.

4.1.1 Obtaining the Digital Image

When the image is digitized, the numbers in a two-dimensional matrix represent the color of points which is known as pixels. These pixel values are in between 0 and 255. In this section, the working environment and camera positions are chosen. First, the working environment and catheter drive system are merged by designing a base part. The base part is fixed in the middle of the magnetic actuator system. Afterwards, the camera position is placed on the magnetic actuator system so that it could see the working environment. The camera image is transformed to the digital environment by using the Python OpenCV module.

The illumination system is important for finding the catheter tip point in the environment. The illumination system reduces the fast pixel change on the image. For this, a glacier-colored 10 mm plexiglass material is taken as a ground of the working area. Then, strip LEDs are placed on the four edges of the plexiglass. After that, the plexiglass edges and back sides are covered with aluminum foil to reflect light only to the front side of the plexiglass. In Figure 4.1, the illumination system of the working area is given. The red marker is the origin point on the working environment.

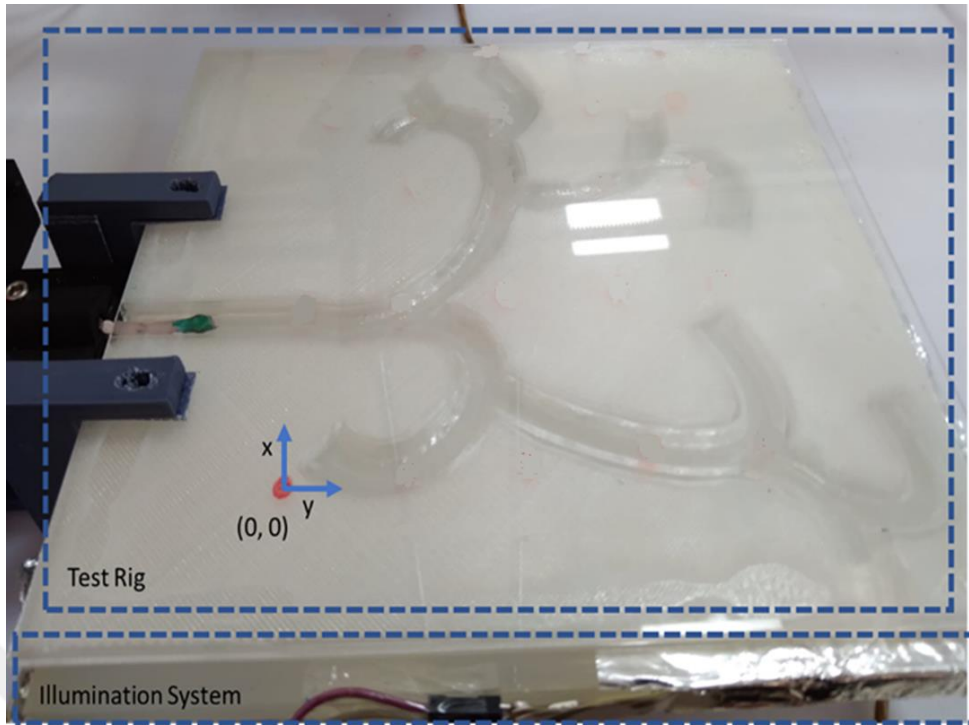


Figure 4.1: Illumination System and Working Environment

4.1.2 Identifying the Target in the Image

Hue Saturation Value (HSV) method is used in the process of identifying the object based on the color [72–74]. HSV is a conical color model that remaps RGB primary colors (Figure 4.2). Hue specifies the angle of the color in the RGB color wheel. It results in 0° red, 120° green, and 240° blue. Saturation controls the amount of color used. A color with 100% saturation is the purest possible color, while a color with 0% saturation provides grayscale. Value controls the brightness of the color. A color with 0% brightness is pure black, while a color with 100% brightness does not contain black mixed into the color.

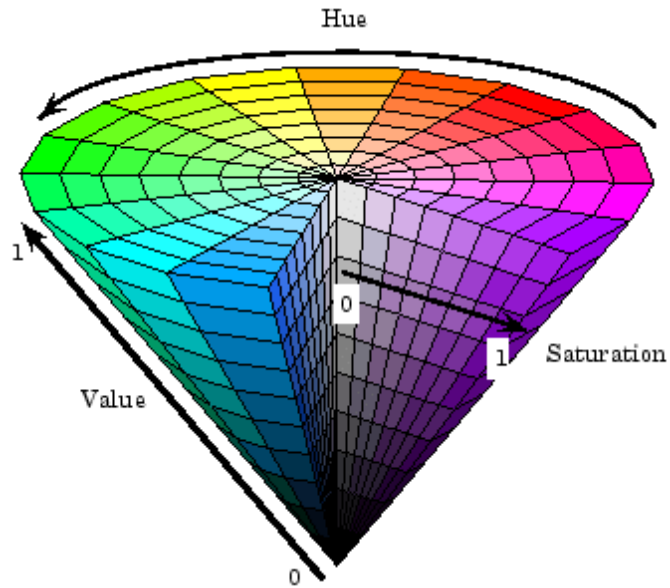


Figure 4.2: HSV Color Circle [75]

First, the detected color was chosen which was different from the environment. In that conclusion, the dark green color was chosen. Later that HSV calibration was made using the python OpenCV module. The HSV color bar to lower and higher values was presented in Figure 4.3.



Figure 4.3: HSV Color Bar Selection

After the HSV calibration values were obtained. The masking process was made using these values. In the Figure 4.4 shows the HSV position result.

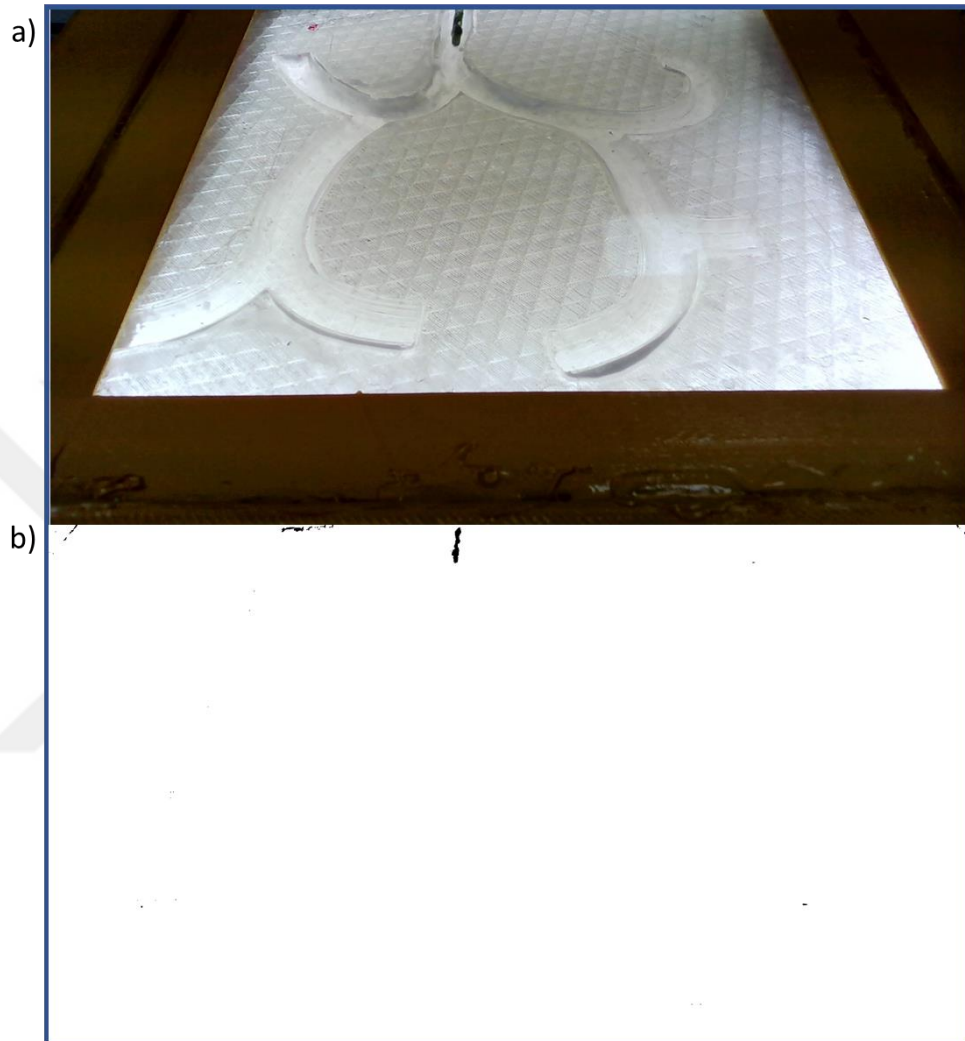


Figure 4.4: HSV Position Detection a) Captured Image, b) Masking of the Captured Image

In the Figure 4.4b presented the HSV masking. The position of the catheter was found by extracting the other part in Figure 4.4a. Also in the figure, HSV masking could not able to eliminate some noise in the image. This noise exists because of the environmental factor and camera precision. A noise reduction filter is applied to the captured image before the masking process to capture a clear image.

4.1.3 Noise Reduction Methods

In image processing applications, noise is a part outside the targeted object. In this way, the program allows us to see only the detected object by not showing unimportant parts. In this process, a filter is required to not show the rest of the image to obtain the desired part [76–78].

First, a median filter is applied to the captured image. The median filter is a non-linear digital filtering technique used to get rid of noise from an image [79]. This noise removal is also one of the preprocessing steps used to improve the results of further processing. The median filter is determined by the pixel values in the specified size of a kernel. These values are sorted arithmetically. Then, the middle pixel in the sequence is selected and placed in the image. In this study, 5×5 median kernel size is selected. Later that high-frequency pixel component was observed in the edge of the image. When the high-frequency components of the image are softened or eliminated, the quality of the image is decreased [80].

Gaussian filter kernel, make the edges of the image clear, while it does not change the original image. The equation of the Gaussian function is given in Equation 4.2. In the equation x is the distance of the horizontal axis, y is the distance of the vertical axis, and σ is the standard deviation of the gaussian distribution.

$$G_{\sigma} = \frac{1}{2\pi\sigma^2} e^{-\frac{(x^2+y^2)}{2\sigma^2}} \quad (4.2)$$

In this part, a 3×3 kernel-sized gaussian filter is added. The performance of the median and Gaussian filters is showed in Figure 4.5.

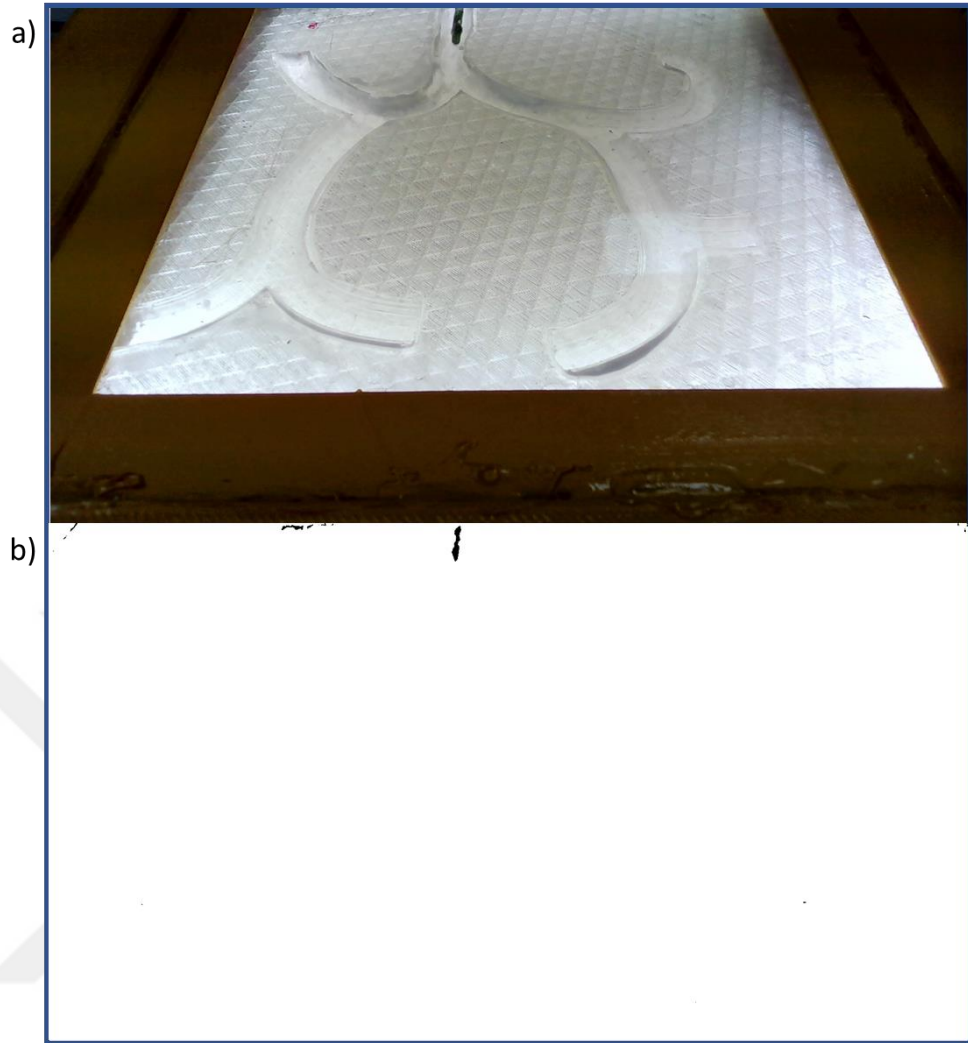


Figure 4.5: Median and Gaussian Filters with HSV Position Detection a) Captured Image, b) Masking of the Captured Image

In the figure, it is understood that noise became lesser. Also captured image is less affected by environmental light. These filters are used to eliminating the fast-changing pixel. But, these filters are also affected the targeted object image. After that, another filter is applied to the masking image instead of capturing the image.

4.1.3.1 Erosion and Dilation

Erosion and dilation filters modify the geometric structure in the image. This filter is used for learning the shape and size of the image. Erosion is enlarged the black region in the image. On the other hand, dilation is enlarged in the white region in the image. The pixel value in the original image of the kernel shifted on the image takes the value

of one if all the pixels under the kernel are one, otherwise, it takes the value of zero [81]. Erosion and dilation make it possible to detect the exact position of the target easily. Without these filters, the center of the targeted area changes rapidly and the position of the object disappears. In Figure 4.6 is showed the performance of the machine vision application.

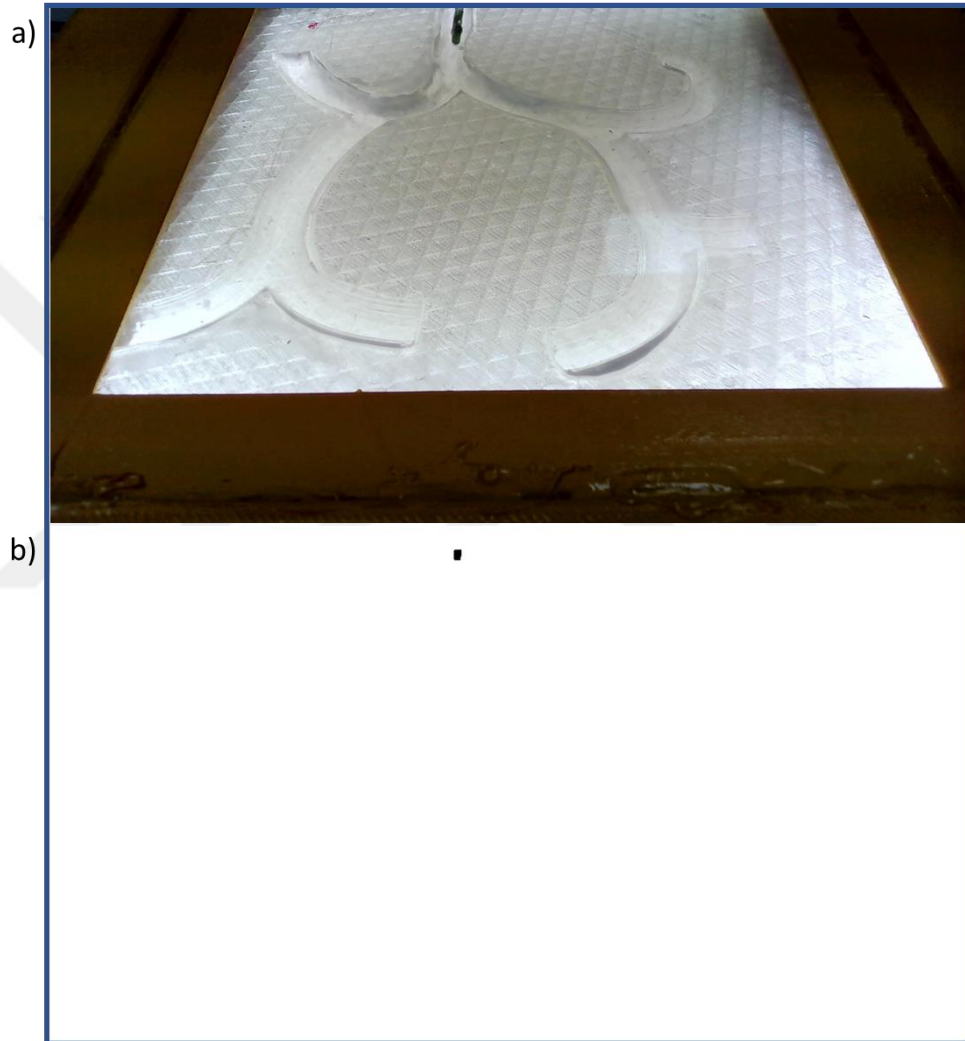


Figure 4.6: Median, Gaussian, Erosion and Dilation Filters with HSV Position Detection a) Captured Image, b) Masking of the Captured Image

After the filtering and masking process localization of the targeted object is found. Filtering is used to reduce the noise effect. Masking is used to locate the catheter tip. The location of the black region in the masking image was found by using the contour finding feature in the OpenCV module.

4.1.4 Obtaining the Position Information of The Target in The Working Environment

In this section coordinate of the targeted object was found. First, camera calibration was needed. Twenty points are selected in the working environment by using a red marker for camera calibration. Later that, x and y pixel coordinate values of marker points are obtained by the camera. The positions of the markers are determined according to the origin in the working environment using a ruler (Figure 4.7).

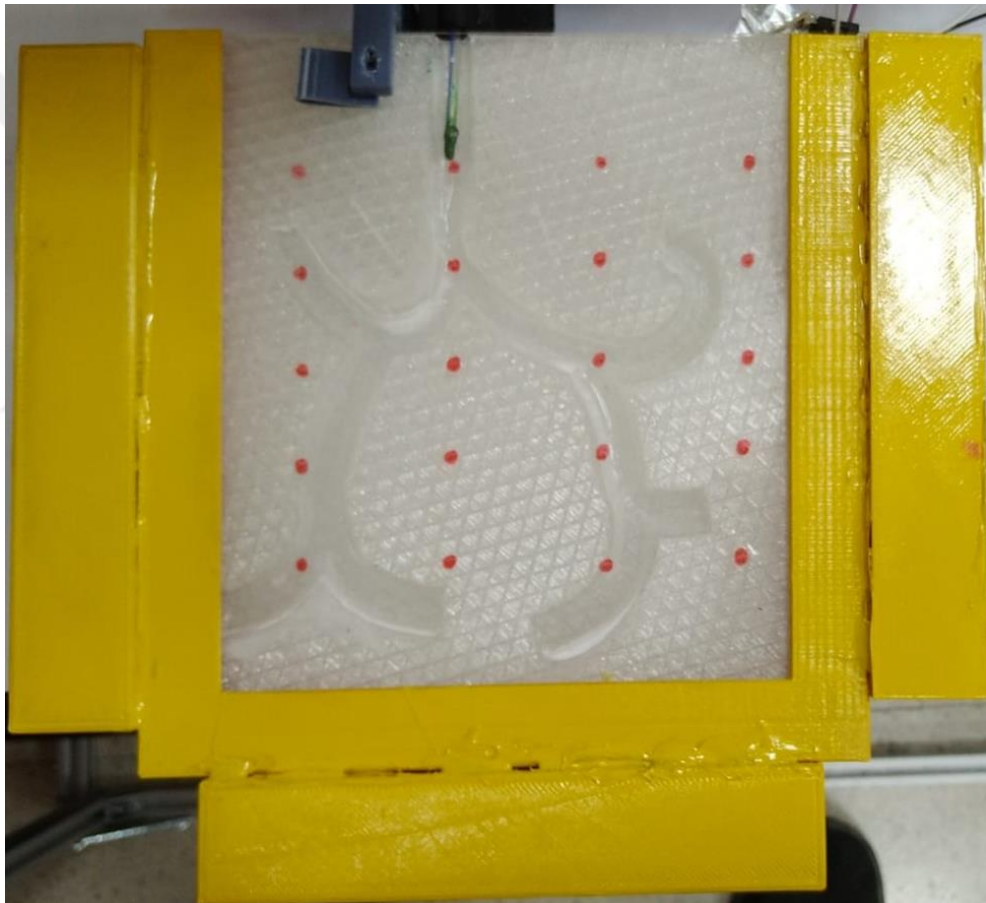


Figure 4.7: The Working Environment Calibration Points

After that, the curve fitting method is applied between the pixel coordinates and the environment points to calibrate the camera. In this study, the curve fitting function is a multi-input and single output function. The curve fitting application is made by using the Matlab program. In Figures 4.8 and 4.9 the curve-fitting graph results are given.

Also, prediction function results are given in Equations 4.6 and 4.7 which are obtained using the curve fitting method.

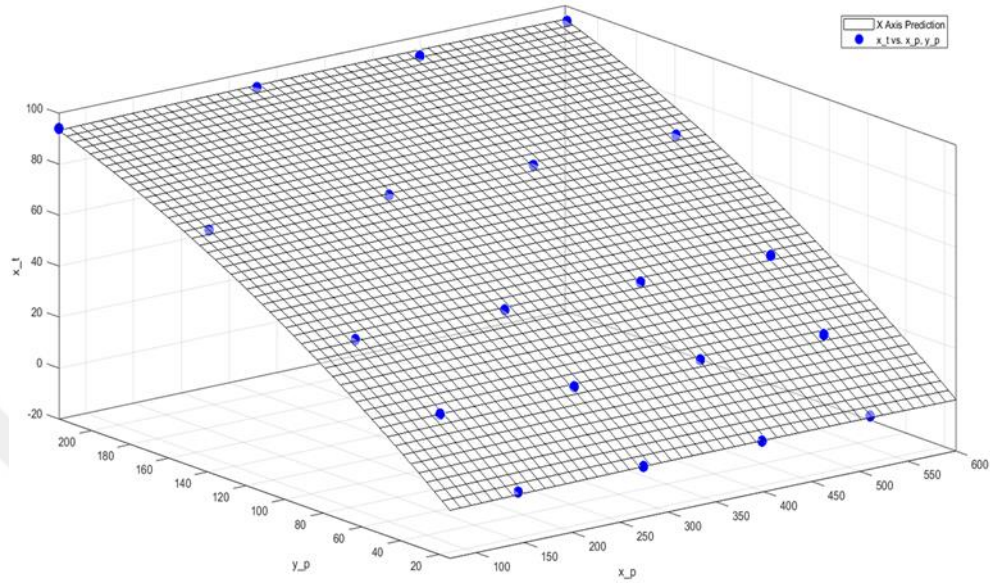


Figure 4.8: Curve Fitting Results of the x_t

$$x_t = -42 + 0.3 * x_p + 0.11 * y_p + 1.4e - 06 * x_p^2 - 0.00043 * x_p * y_p + 7.7e - 05 * y_p^2 \quad (4.6)$$

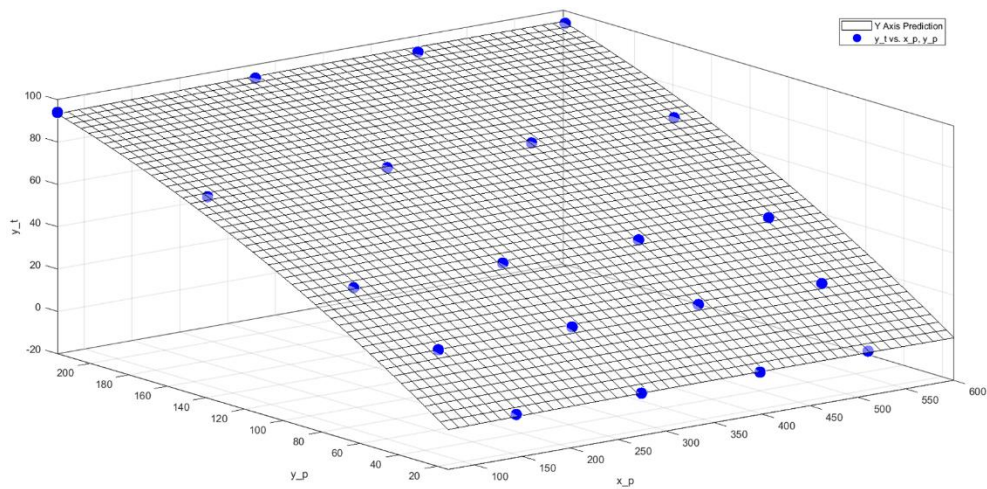


Figure 4.9: Curve Fitting Results of the y_t

$$y_t = -10.8 + 0.01 * x_p + 0.67 * y_p + -9.3e - 06 * x_p^2 - 1.81e - 06 * x_p * y_p - 0.001 * y_p^2 \quad (4.7)$$

After obtaining the estimation function, the position of the tip of the catheter was found. Curve fitting prediction function accuracy is 99.8% for the x-axis and 99.3% for the y-axis. Those results are not only used for catheter position detection. In the operator control, mouse click position on image converted using Equations 4.6 and 4.7. Those mouse positions are used for desired positions.



Chapter 5

Catheter Motion

During the movement of the catheter, the drive system, the guidance system, and the visual feedback system are worked synchronously. A detailed block diagram for the Catheter Motion System is given in Figure 5.1. In this section, task control with the Human-Machine interface is mentioned [82, 83]. Then, the control of the Robotic Operating System (ROS) and the block diagram of each system are presented. Afterwards, the working area of the system is mentioned. Moreover, magnet desired points are converted to the catheter's desired position. In this part, the machine learning method is used. In the last part, the motion experiment and its results are presented.

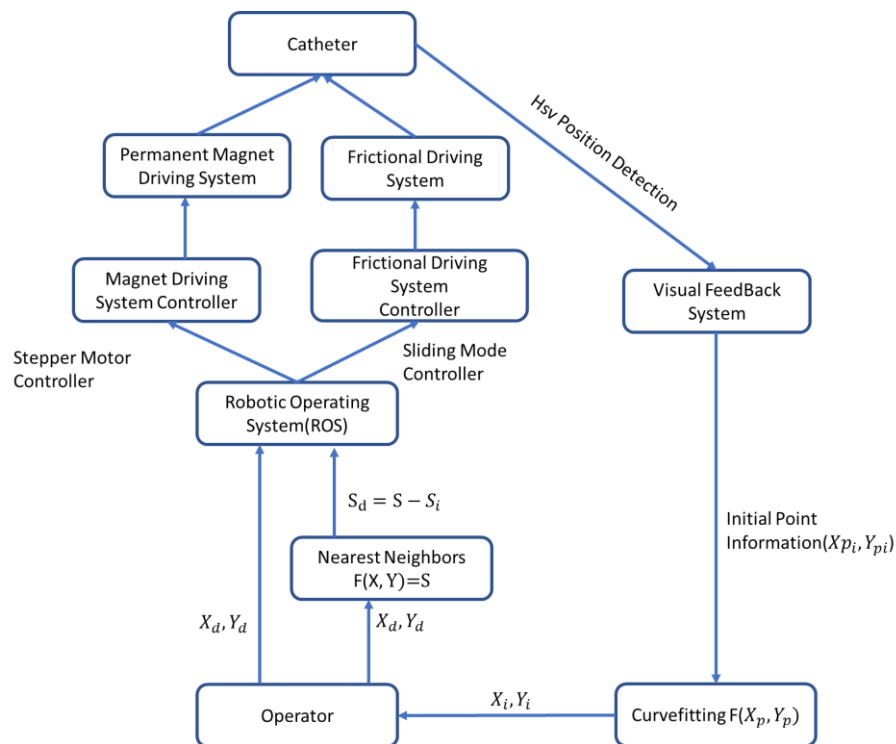


Figure 5.1: System Block Diagram

5.1 Task Controller

In this section, using the task controller, Permanent Magnet Driving, Frictional Driving, and Visual Feedback Systems are worked together. Three systems are worked synchronously, which is accomplished by the ROS controller.

5.2 ROS Based Control

The most problematic part of this project is the control part. Because the number of controlled systems is more than one. In this part, the system is monitored by the operator using the camera system. Also, the feedback is obtained by the camera at the same time.

A master controller is needed to control these three systems in real-time. ROS controller is used as a master controller. ROS is a Linux-based, open-source framework to use in robot applications [83]. ROS is a useful framework for its performance and usage because it uses object-oriented programming within multiple systems [84, 85]. Object-oriented programming is a programming language model that organizes software design around data or objects rather than functions and logic. ROS consists of three basic parts: the file system, the compute graph, and the community.

5.2.1 Filesystem Level

The file system is the basic part that allows the ROS framework to be organized. ROS has packages in its software center. The modularity of ROS allows users to select and use ready-made packages. Many packages in ROS can be easily connected to other devices and those devices can be controlled. ROS packages created by users are used by other ROS community members due to open-source software. This feature increases the framework performance every day. Packages can contain execution programs called nodes, a library, datasets, configuration files, third-party software, or any software that needs to be organized together. The biggest advantage of packages is that they provide easy functionality so they can be reused for many different projects.

This organizational system, as well as object-oriented programming and packages, work harmoniously together to achieve the desired purpose. Packages often consist of the following contents: package declarations, message types, service types, headers, executable scripts, build files, and runtime processes. Packages contain message types for messages sent in ROS and request (req) and response (res) service types for services.

5.2.2 Computation Graph Level

Compute graph is a where network data is processed peer-to-peer in ROS. The basic elements of the compute graph level of ROS are nodes, messages, threads, services, bags, main and parameter servers. Nodes are an element of ROS that connect and receive information from topics, perform inter-system computations, receive data from sensors and control actuators, and broadcast data for other nodes to use. Nodes communicate with each other via messages. Messages are carried through a communication system which is publishing and subscription. A node sends its message to a specific topic. The topic is a name used to describe the content of the message. The publish/subscribe model is a one-way communication paradigm. Services provide the request/response interactions required in distributed systems. Bags are a data storage format for recording and playing ROS message data. Parameter Server provides key storage of data in a central location. The master provides communication between nodes and they exchange messages. The communication of ROS between packages is shown in Figure 5.2.

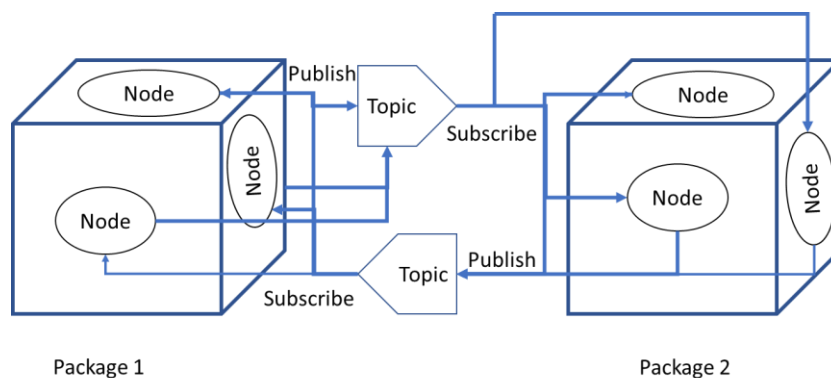


Figure 5.2: Graphical Representation Of ROS Procedure

5.2.3 ROS Community Level

ROS Community Level is a ROS resource that enables separate communities to exchange software and information. ROS Community Level consists of ROS distributions, repositories, ROS Wiki, and ROS answers.

5.2.4 Basic ROS Commands

ROS provides users with a variety of tools to make navigating and debugging the ROS file system simple as possible. A few key ROS commands used in this thesis are shown in Table 5.1.

Table 5.1: ROS Commands

roscore	Start ROS Master
roslaunch <pkg name> <node_name (python or c++)>	Execute Node File
roslaunch <pkg name> <launch_file>	Execute Launch File
rostopic list	Lists all active topics.
rostopic info </topic name>	Information about topic
rostopic echo </topic name>	Listen to topic message
rosclear	Name of all executed nodes
rosclear info </node name>	Information about node
rosclear rqt_graph rqt_graph	Tools to visualize graphical representation of nodes, and topics
rosclear record -0 <filename> </topic name>	Record data from a desired topic
rosclear type </topic name>	Show message type of any topic
rosclear msg show </message name>	Show detail of message type
rosclear topic pub </topic name> </message name> <args>	Publishes data on to a topic

5.2.5 ROS Packages

In this study, the Robotis Dynamixel Workbench package was used to control the drive system. Serial Communication of ROS-Arduino package is used for the guidance system. Arduino stepper motor library is used to control the multiple step motors synchronously. In visual feedback, the position information is obtained by using the OpenCV (Open Source Computer Vision) module of the Python 2.6 program. The Qt-

Design ROS program is an rqt-based interface program that combines these three systems.

5.2.5.1 Robotis Dynamixel Workbench

As mentioned before, this project consists of three systems. The first system is the catheter drive system, and the Robotis Dynamixel motor is used as the actuator. The ready-made package of Robotis for ROS is easier for motor control. ROS node was created by using the sliding mode controller in the Python program by using position, velocity, and current values. The service package of the Dynamixel motor for ROS determines the speed and the current value of the motor. The feedback of the actuator is made using the subscriber command. The block diagram of the catheter drive system is given in Figure 5.5.

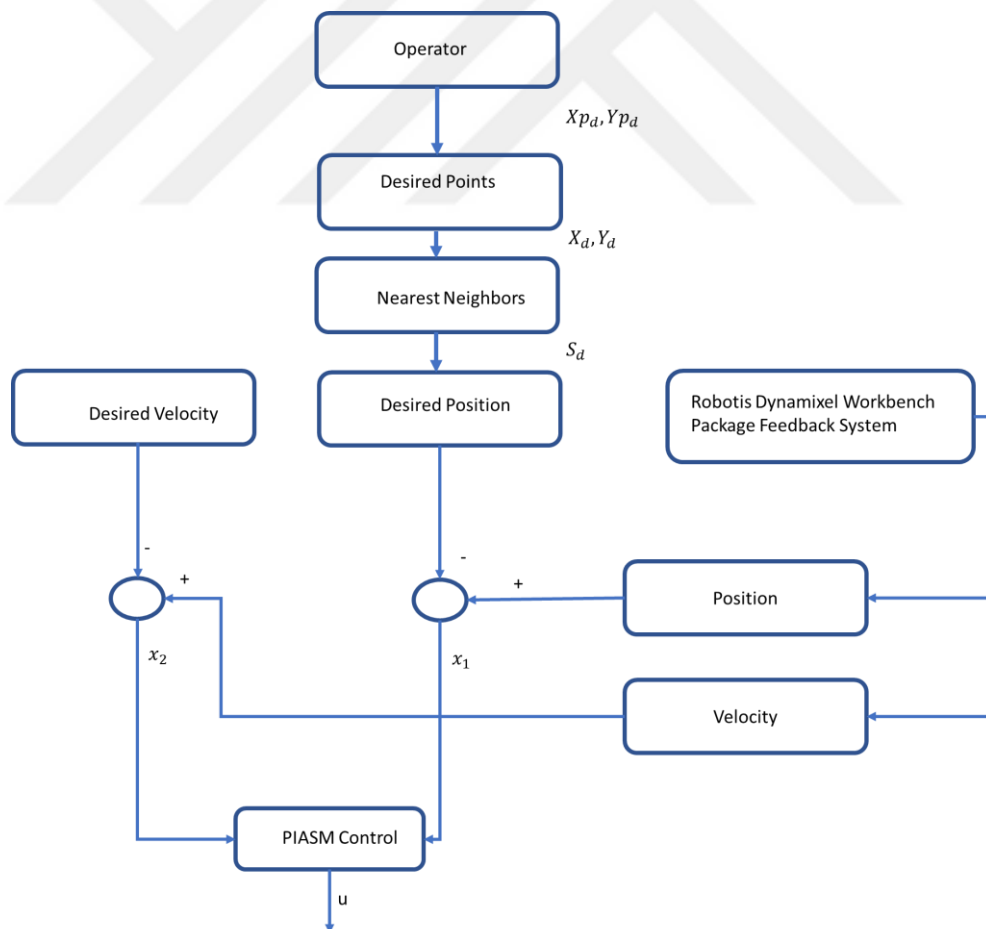


Figure 5.3: Catheter Driving System Block Diagram

In the block diagram, the desired position is obtained using the Nearest Neighbors method. The input data of the Nearest Neighbors method are desired positions of the magnetic actuator system (X_d, Y_d). Output data are catheter desired position (S_d). Data points are created using the SolidWorks program. In the SolidWorks program, 300 data points are collected for training. Later that, data is trained in the Nearest Neighbors algorithm using the python scikit-learn module. After that, the prediction model has a 99.93% accuracy value. Later that, the prediction model is saved using the python pickle model then it is used inside the master controller.

5.2.5.2 ROS- Arduino Serial Communication

The magnet drive system is actuated by two Nema 23 stepper motors. In the driving process of stepper motors, an Arduino Mega microcontroller [86] was used. Arduino has a ROS serial communication package. First, stepper motors were controlled synchronously with Arduino. The ready-made stepper motor library is used which is provides the synchronous movement of the stepper motors. Then, the position values for two motors are sent by the subscribe command. The block diagram of the magnet drive system is given in Figure 5.6.

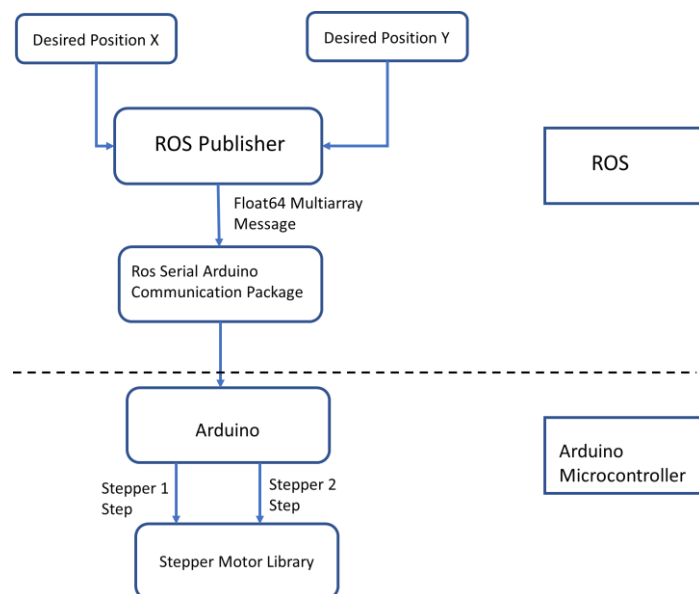


Figure 5.4: Magnet Driving System Block Diagram

5.2.5.3 OpenCV Module

In this section, the python image processing module is presented. OpenCV is generally used in works involving feature analysis such as image processing and object identification on videos or images [87, 88]. The second OpenCV program is used to getting the pixel coordinates of the selected point on the video image by just using the mouse click. The visual feedback system block diagram is presented in Figure 5.7.

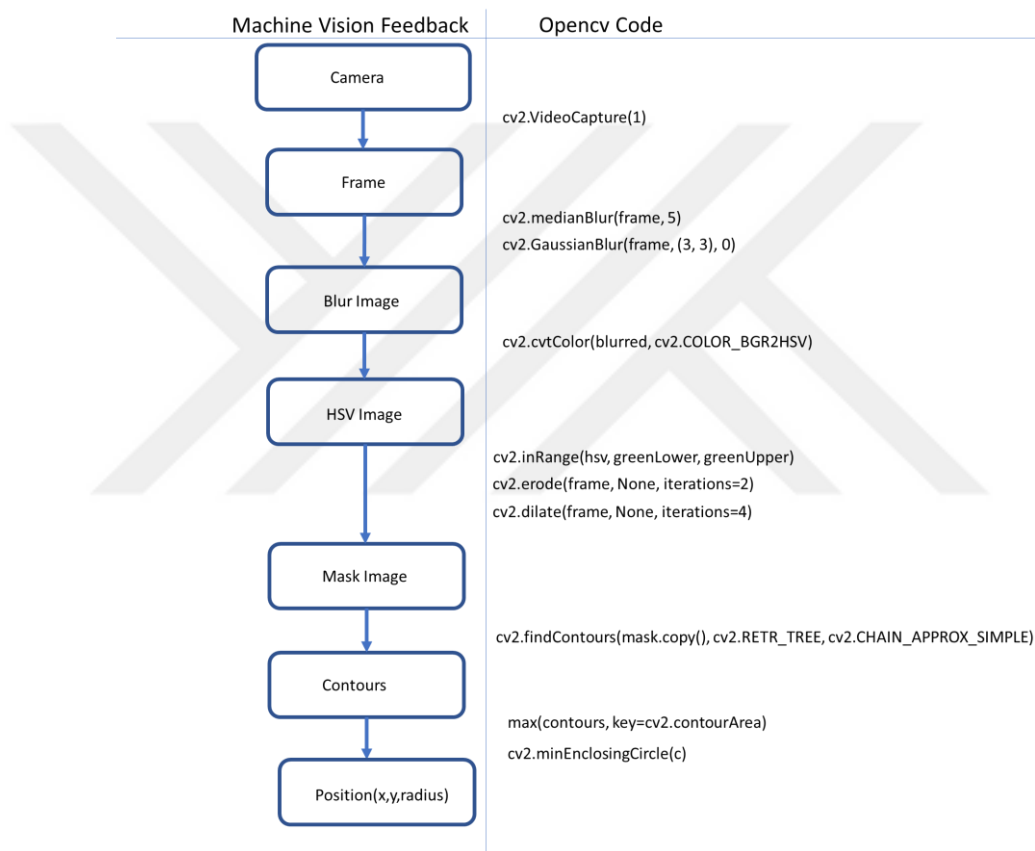


Figure 5.5: Machine Vision Feedback Block Diagram

5.2.5.3 QT-Design

These three systems can be controlled separately with object-oriented programming. In this part, the Qt-design interface is used as a master program. In this way, all systems are combined in a single interface. The block diagram of the Qt design system is given in Figure 5.8.

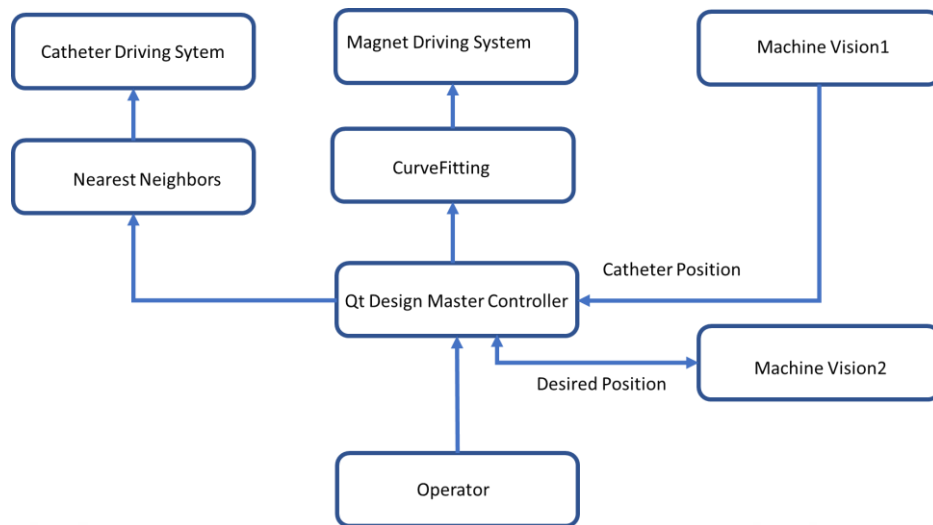


Figure 5.6: QT-Design Block Diagram

5.3 Working Environment

CAD designs of the working environment were found on the internet. 2D representation of the bronchial tracts was preferred as the working area. CAD design of the branchial tree is given in Figure 5.7.

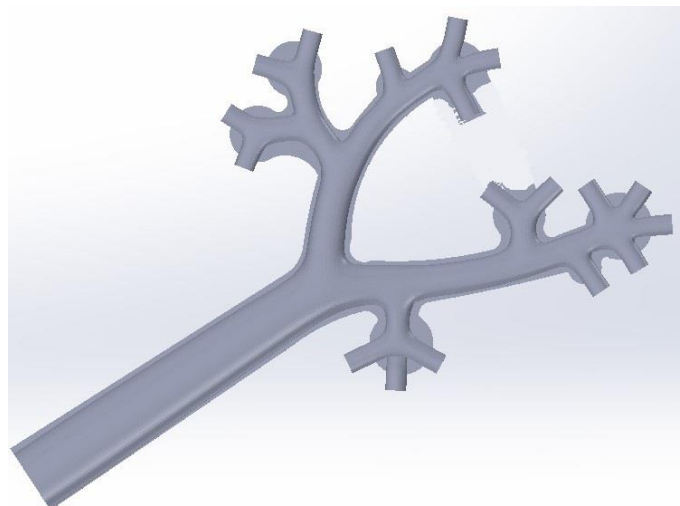


Figure 5.7: 2D Bronchial CAD Model

Afterwards, it was decided to cut the system in the middle and cover it with transparent plexiglass so that the catheter could move inside the CAD model and the catheter can be seen with the camera. The final modified version of the working environment is given in Figure 5.8. The working environment was produced with a transparent filament material using a 3D printer (Figure 5.8b).

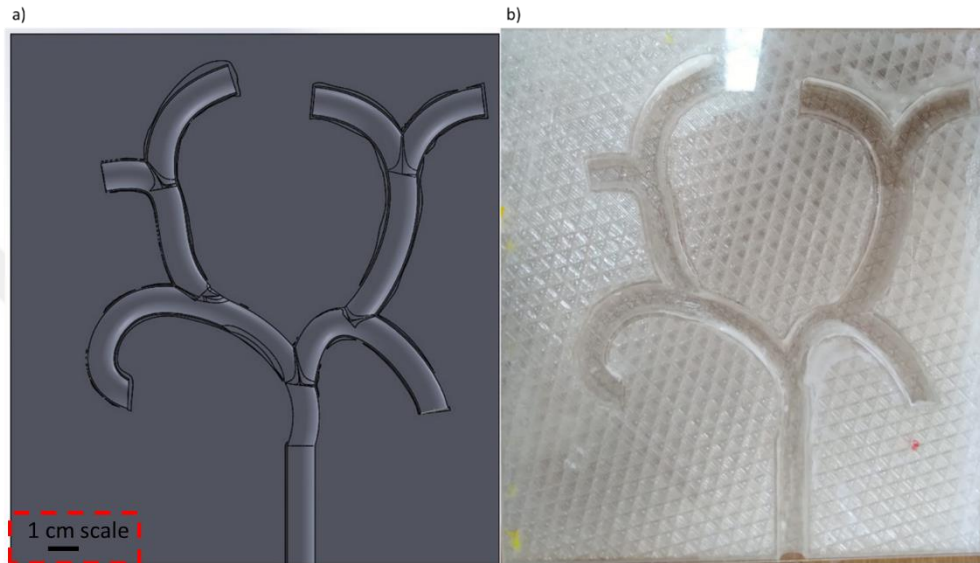


Figure 5.8: Working Environment of a) CAD Model, b) Test Rig

5.4 Motion Control Experiment

In this section, the catheter motion under the sliding mode controller is examined. Also, catheter guidance performance is discussed. The experimental setup is given in Figure 5.9. The experiment assumed that catheter driving force (F_m) is not affected by magnetic actuation force (F_{pm}). Because of catheter driving force much higher than magnetic actuation force. Because the catheter driving force is much higher than the magnetic actuation force.

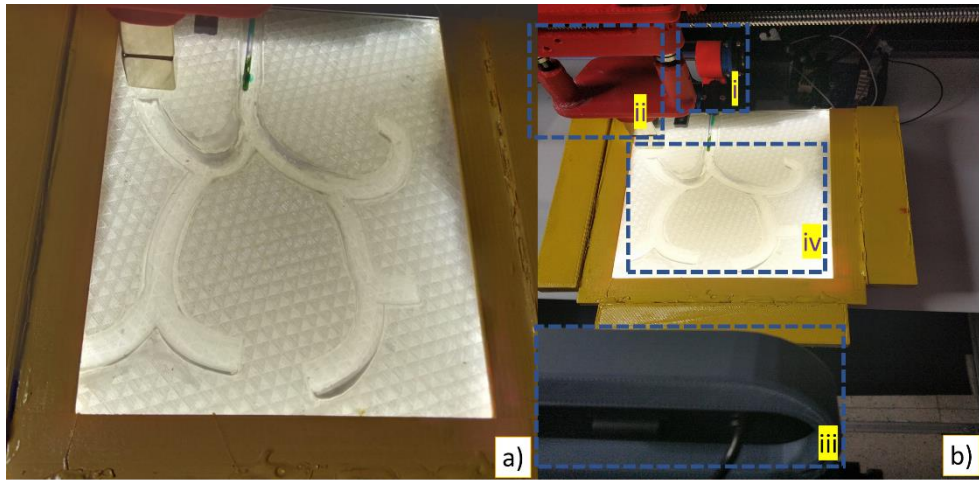


Figure 5.9: Experimental Setup a) Test Rig b) Experimental Setup Components (i- Frictional Drive, ii-Guidance System, iii-Image Acquisition System, iv- Test Rig and Its Illumination System)

The Qt-Design interface of the system is given in Figure 5.10. The user interface has three modes. In the initialization mode, has two buttons is exist. In the initiate setup button, the systems are controlled manually by entering the desired value into the text box. The Activate Front Camera button is used to measure the initial position of the catheter. In the Operation mode, has two buttons is exist. Select Reference point is used for human-machine interface to choose the desired position of the catheter location. Active control setup is selected and the system starts working automatically. The Debugging mode two-button is exists. The catheter Stop button is stopped the catheter drive system and Send uPMA to Origin button sent the magnet drive system to the origin point which is chosen by the operator.

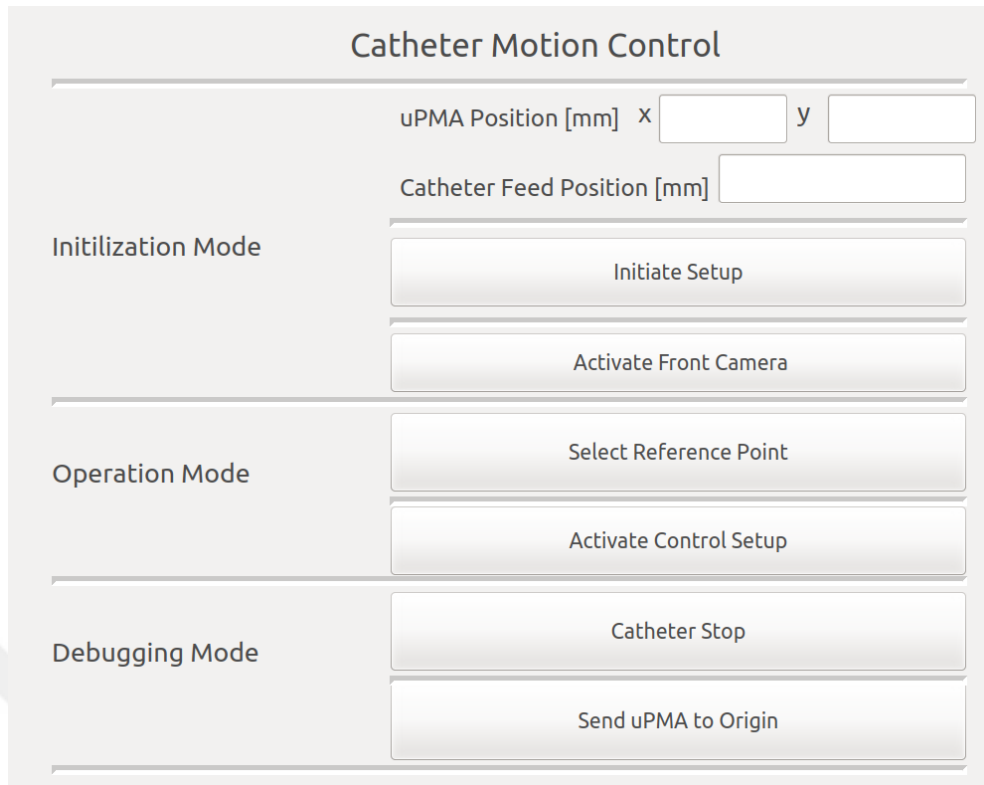


Figure 5.10: User Interface

5.4.1 Experimental Result

In this experimental study, the catheter drive system is controlled using the Proportional Integral Asymptotic Sliding Mode. In the experiment, the catheter is sent to the six points of the working area. Later, the catheter is brought back to the initial position. The position status, the input graph, the position path of the catheter, and the images of the system at a certain time are given in Figures 5.11 to 5.16.

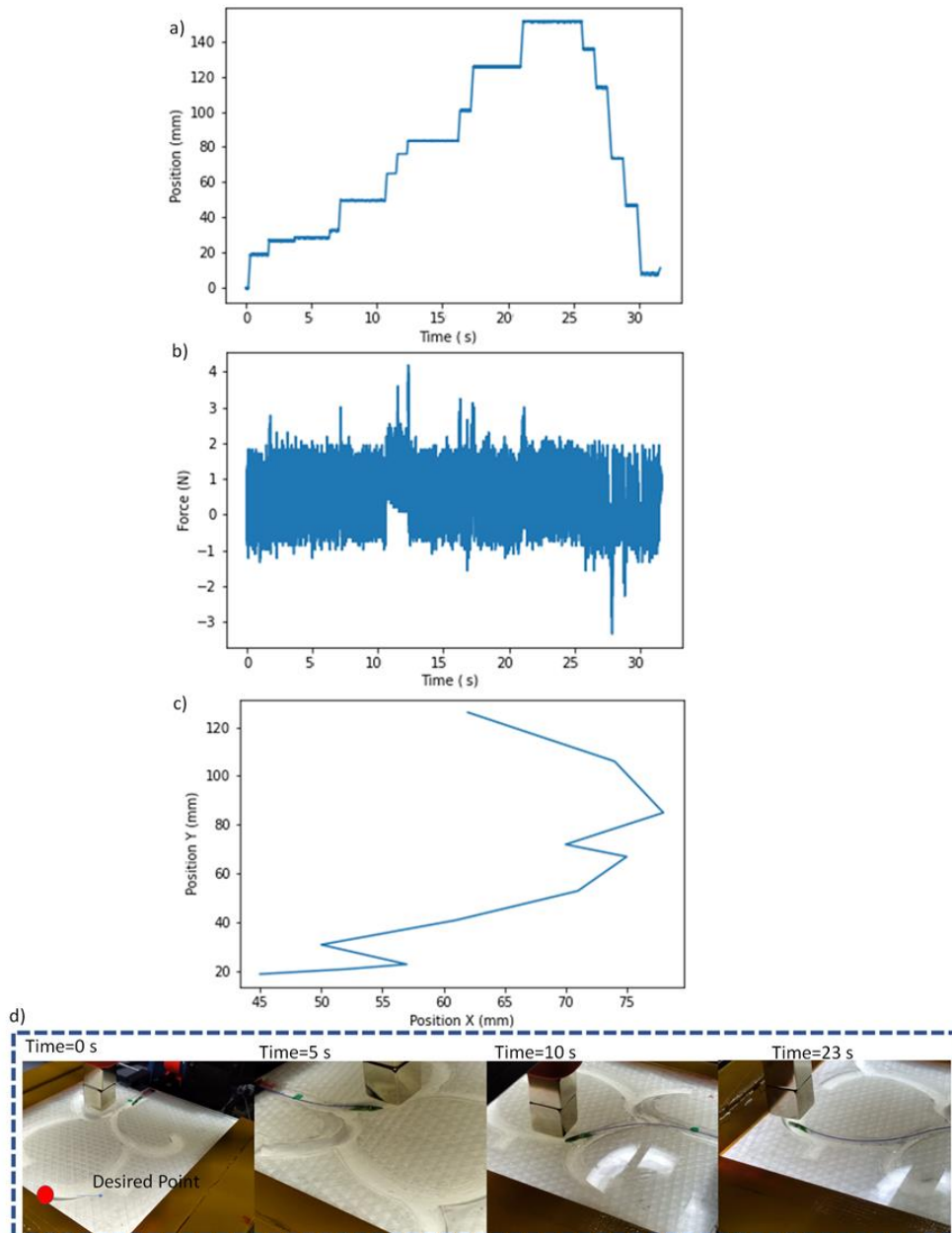


Figure 5.11: Desired Position 1 of the Catheter Motion System a) Position State, b) Input Graph, c) Position Path of The Catheter, d) The Images of System at Certain Times

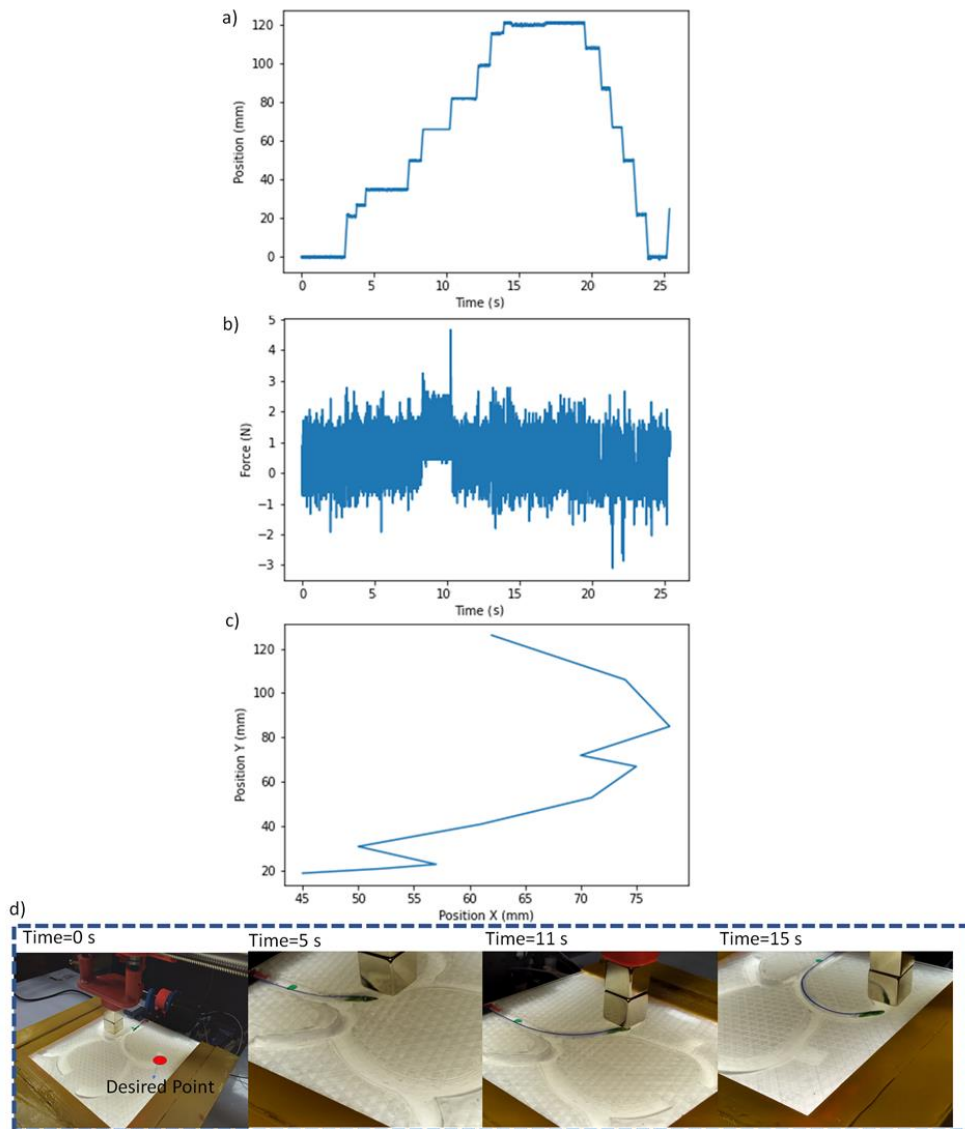


Figure 5.12: Desired Position 2 of the Catheter Motion System a) Position State, b)Input Graph, c) Position Path of The Catheter, d) The Images of System at Certain Times

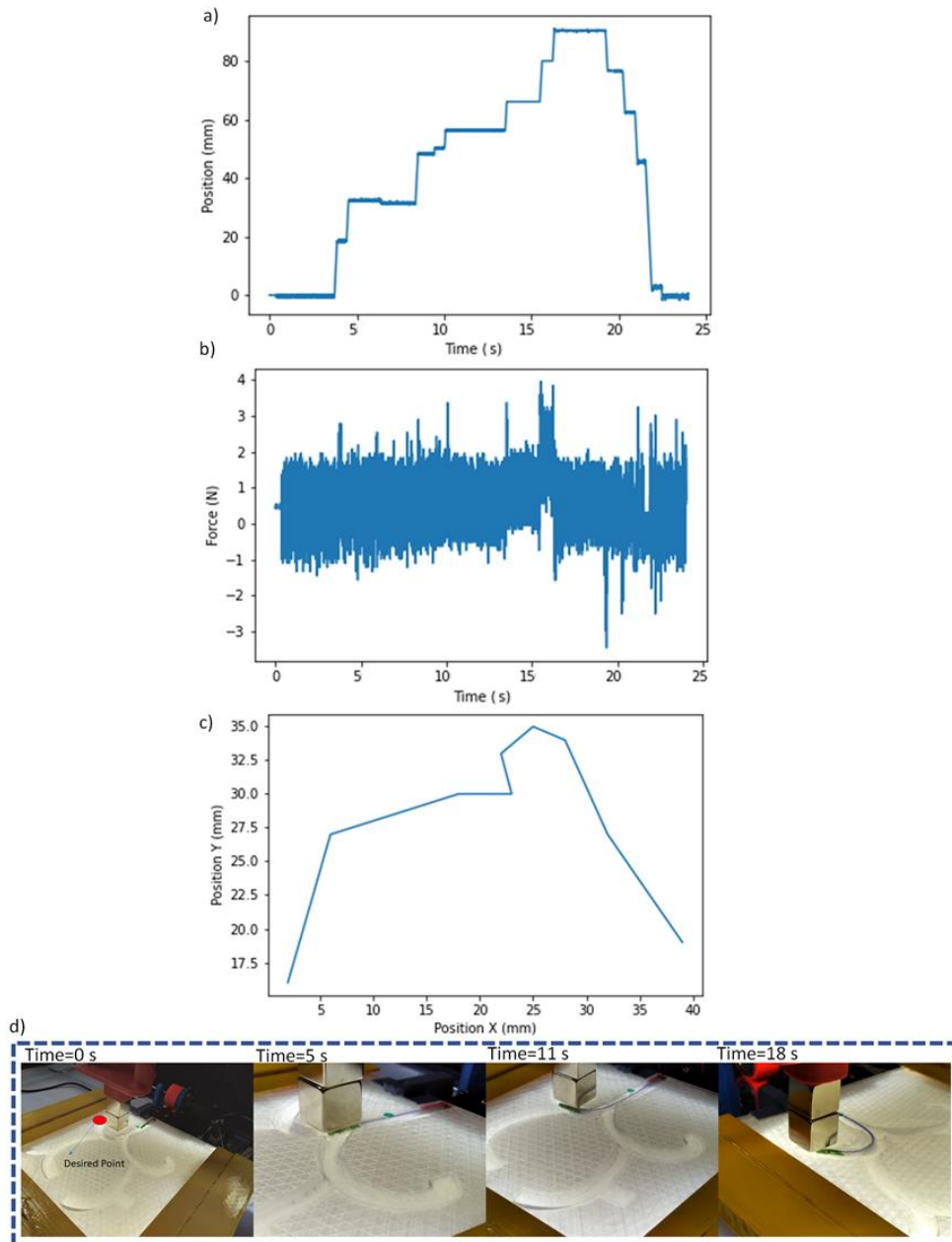


Figure 5.13: Desired Position 3 of the Catheter Motion System a) Position State, b) Input Graph, c) Position Path of The Catheter, d) The Images of System at Certain Times

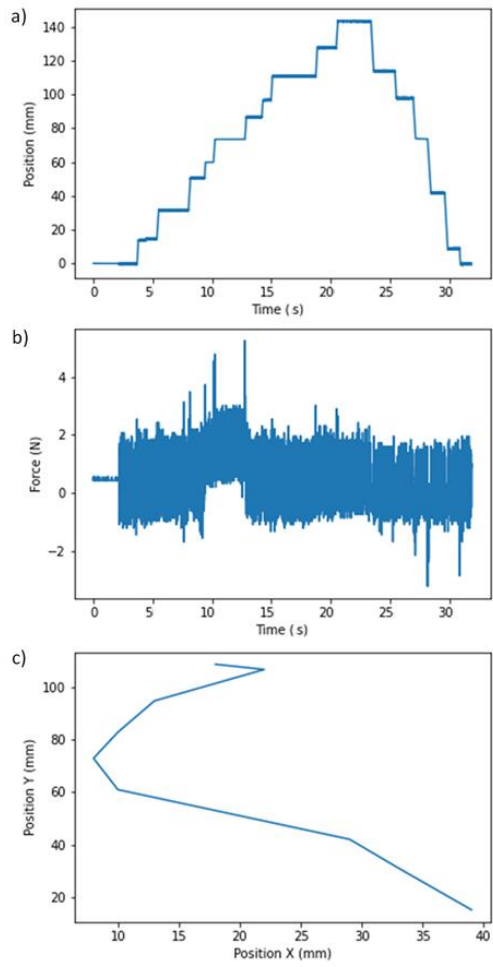


Figure 5.14: Desired Position 4 of the Catheter Motion System a) Position State, b)Input Graph, c) Position Path of The Catheter, d) The Images of System at Certain Times

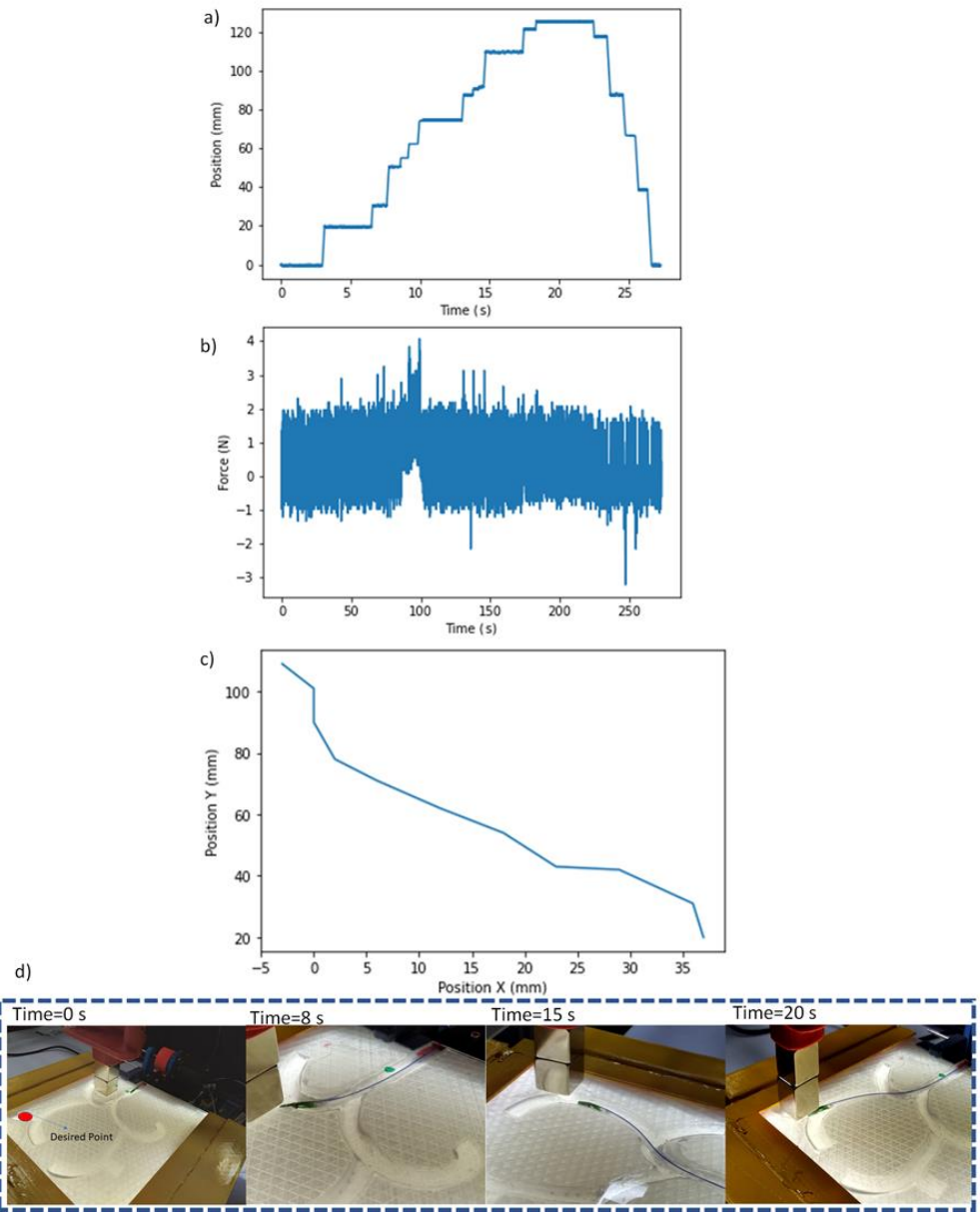


Figure 5.15: Desired Position 5 of the Catheter Motion System a) Position State, b)Input Graph, c) Position Path of The Catheter, d) The Images of System at Certain Times

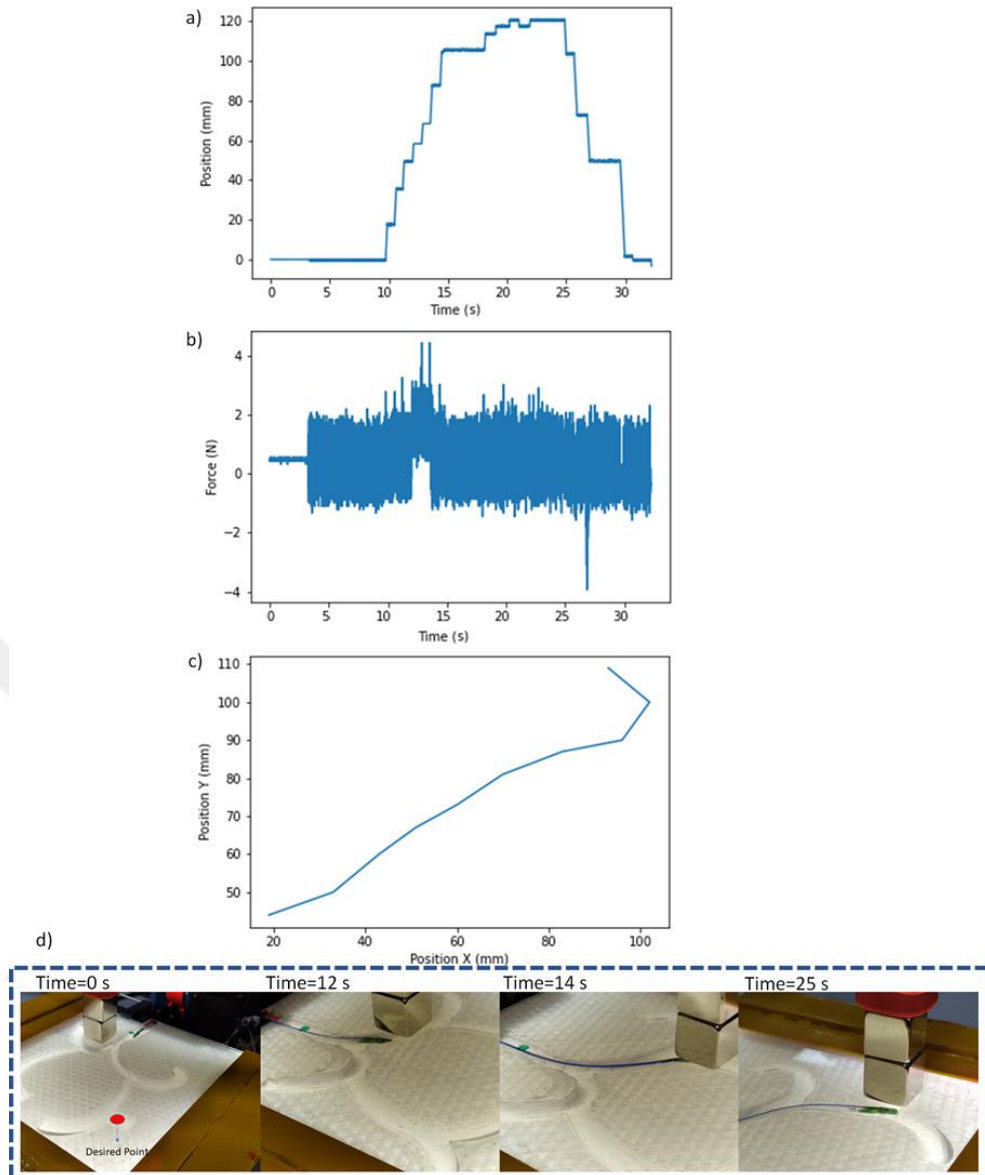


Figure 5.16: Desired Position 6 of the Catheter Motion System a) Position State, b)Input Graph, c) Position Path of The Catheter, d) The Images of System at Certain Times

5.5 Discussion

When all the results are examined, it is seen that the system reaches the desired points with high accuracy. The system is passed at least 7 location points to reach the goal points. In that location point, the system constantly chattering between 3 and 0.5 mm. The catheter reached the desired points more easily due to the chattering situation. Because the static friction does not affect the catheter during the motion and small

magnetic particle inside the catheter is easily affected by the external magnetic field. In the controller, it is proven that the amount of chattering is adjusted depending on a disturbance frequency value.

Compared to other sliding mode controller studies, a controller with high accuracy was obtained despite the changing disturbance value. At the same time, the chattering range of the controller is limited. In some studies, it is mentioned that the accuracy and robustness of the system are decreased with the application of the chattering attenuation method[89, 90]. Within the scope of this study, it is proven that the accuracy of the system is kept high by limiting the chattering range.

This study proves that the designed frictional driving system has overcome the slippage problem. Compared to other studies, the position loss of the system was prevented by conducting experiments on the slippage problem. In this way, high accuracy and precision of the catheter drive mechanism were designed. In addition, the catheter was controlled using force control. In this way, the catheter is effective against the unknown friction force in the body.

Chapter 6

Conclusion

As a result of this thesis, catheter motion control is provided by the synchronous operation of the frictional catheter driver and the permanent magnet actuator system. The catheter is not continuously positioned with the camera system. Because the position of the catheter is lost at several points in the working environment. This causes the system to lose all performance. For this reason, the initial position of the catheter is obtained using HSV color detection and several filters. The initial value is used at the beginning of the controller. Later the catheter was controlled autonomously by the operator using an open-loop controller strategy. The catheter drive system was controlled with the proportional-integral asymptotic sliding mode which is found in this study. It is learned that a minimum amount of chattering is required in order to prevent the catheter from being exposed to static friction during the movement to six desired points in the working environment. Also chattering in the system makes it easier to bend the catheter tip.

The position accuracy and system stability result show that this new controller is effective against changing disturbance values. In the experiment, the range of the chattering is adjusted by changing the magnitude and the frequency of the disturbance signal. The high accuracy of the catheter position and no overshoot were observed in the system due to the Integral controller. Also, the high accuracy of the catheter driving system proved that the slippage effect is eliminated in this work. This study performed with a catheter system guided by a planar magnetic actuator and driven by a frictional system is contribute to the easy control of the catheter in surgical operations. Thanks to this thesis, it contributes to the control of the 3D magnetic actuator and the use of small magnetic particles in surgical operations.

In the future, the force sensor will be added. Additionally, the magnetic actuation mechanism will be improved and the system starts working in 3d space. The magnetic actuation system will produce more magnetic force. The test rig will be a replica of the human lung model. The catheter will be smaller. The catheter motion system will be controlled by a close-loop controller.



References

- [1] Fuchs KH, Gastrointestinal U, Disorders F. Minimally Invasive Surgery. *Endoscopy* 2002; 34: 154–159.
- [2] Putten EPW Van Der, Goossens RHM, Jakimowicz JJ. Minimally Invasive Therapy & Allied Technologies Haptics in minimally invasive surgery – a review. 5706. Epub ahead of print 2009. DOI: 10.1080/13645700701820242.
- [3] Jaffray B. Minimally invasive surgery. *Arch Dis Child* 2005; 90: 537–542.
- [4] Haissaguerre M, Gencel L, Fischer B, *et al.* Successful catheter ablation of atrial fibrillation. *J Cardiovasc Electrophysiol* 1994; 5: 1045–1052.
- [5] Alam MW, Vedaei SS, Wahid KA. A fluorescence-based wireless capsule endoscopy system for detecting colorectal cancer. *Cancers (Basel)* 2020; 12: 890.
- [6] Betensky BP, Jauregui M, Campos B, *et al.* Use of a Novel Endoscopic Catheter for Direct Visualization and Ablation in an Ovine Model of Chronic Myocardial Infarction. 2012; 1–8.
- [7] Khoshnam Tehrani M, Rajni Patel S V, Tehrani K, *et al.* Modeling and Control of Steerable Ablation Catheters, <https://ir.lib.uwo.ca/etd> (2014).
- [8] Feng W, Chi C, Wang H, *et al.* Highly precise catheter driving mechanism for intravascular neurosurgery. In: 2006 IEEE International Conference on Mechatronics and Automation, ICMA 2006. IEEE, 2006, pp. 990–995.
- [9] Khoshnam M, Azizian M, Patel R V. Modeling of a steerable catheter based on beam theory. *Proc - IEEE Int Conf Robot Autom* 2012; 4681–4686.
- [10] Jeon S, Hoshidar AK, Kim K, *et al.* A Magnetically Controlled Soft Microrobot

Steering a Guidewire in a Three-Dimensional Phantom Vascular Network. *Soft Robot* 2019; 6: 54–68.

- [11] You H, Bae E, Moon Y, *et al.* Automatic control of cardiac ablation catheter with deep reinforcement learning method. *J Mech Sci Technol* 2019; 33: 5415–5423.
- [12] Sganga J, Eng D, Graetzel C, *et al.* Autonomous Driving in the Lung using Deep Learning for Localization. 2019; 1–10.
- [13] Gosselin FP, Lalande V, Martel S. Characterization of the deflections of a catheter steered using a magnetic resonance imaging system. *Med Phys* 2011; 38: 4994–5002.
- [14] Ryan S. Penning, Jinwoo Jung, Justin A. Borgstadt NJF. Towards closed loop control of a continuum robotic manipulator for medical applications. *IEEE Int Conf Robot Autom* 2011; 3: 193–196.
- [15] Schmidt B, Chun KRJ, Tilz RR, *et al.* Remote navigation systems in electrophysiology. *Europace* 2008; 10 Suppl 3: 57–61.
- [16] Chun KRJ, Schmidt B, Köktürk B, *et al.* Catheter ablation - New developments in robotics. *Herz* 2008; 33: 586–589.
- [17] Choi H, Choi J, Jeong S, *et al.* Two-dimensional locomotion of a microrobot with a novel stationary electromagnetic actuation system. *Smart Mater Struct*; 18. Epub ahead of print 2009. DOI: 10.1088/0964-1726/18/11/115017.
- [18] Abbott JJ, Ergeneman O, Kummer MP, *et al.* Modeling magnetic torque and force for controlled manipulation of soft-magnetic bodies. *IEEE Trans Robot* 2007; 23: 1247–1252.
- [19] Nelson BJ, Kaliakatsos IK, Abbott JJ. Microrobots for minimally invasive medicine. *Annu Rev Biomed Eng* 2010; 12: 55–85.
- [20] Magdanz V, Gebauer J, Mahdy D, *et al.* Sperm-templated magnetic microrobots. *Proc MARSS 2019 4th Int Conf Manip Autom Robot Small Scales* 2019; 1–6.

- [21] Iacovacci V, Ricotti L, Signore G, *et al.* Retrieval of magnetic medical microrobots from the bloodstream. *Proc - IEEE Int Conf Robot Autom* 2019; 2019-May: 2495–2501.
- [22] Alasli A, Çetin L, Akçura N, *et al.* Electromagnet design for untethered actuation system mounted on robotic manipulator. *Sensors Actuators, A Phys* 2019; 285: 550–565.
- [23] Furlani EP. Permanent magnet and electromechanical devices: materials, analysis, and applications. Academic press, 2001.
- [24] Chen R, Folio D, Ferreira A. Computational Electromagnetics Performances of Magnetic Microrobotics Systems. *2019 IEEE Int Conf Comput Electromagn ICCEM 2019 - Proc* 2019; 1–3.
- [25] Choi H, Cha K, Choi J, *et al.* EMA system with gradient and uniform saddle coils for 3D locomotion of microrobot. *Sensors and Actuators, A: Physical* 2010; 163: 410–417.
- [26] Amokrane W, Belharet K, Souissi M, *et al.* Macro–micromanipulation platform for inner ear drug delivery. *Rob Auton Syst* 2018; 107: 10–19.
- [27] Demircali AA, Varol R, Erkan K, *et al.* Untethered MicroRobot Motion Mechanism with Increased Longitudinal Force. *J Mech Robot* 2021; 1–12.
- [28] Fitane E, Messine F, Nogarède B. The electromagnetic actuator design problem: A general and rational approach. *IEEE Trans Magn* 2004; 40: 1579–1590.
- [29] Carpi F, Pappone C. Stereotaxis Niobe magnetic navigation system for endocardial catheter ablation and gastrointestinal capsule endoscopy. *Expert Rev Med Devices* 2009; 6: 487–498.
- [30] Liu J, Wang Q, Wang H, *et al.* Design and Fabrication of a Catheter Magnetic Navigation System for Cardiac Arrhythmias. *IEEE Trans Appl Supercond* 2016; 26: 5–8.
- [31] Nguyen BL, Merino JL, Gang ES. Remote Navigation for Ablation Procedures – A New Step Forward in the Treatment of Cardiac Arrhythmias. *European*

Cardiology Review 2010; 6: 50.

- [32] Stammes CW, Prest PH, Mobley CG. A friction drive robot wrist: electronic and control requirements. *Mechatronics* 1992; 2: 391–401.
- [33] Spaelter U, Samur E, Bleuler H. A 2-DOF friction drive for haptic surgery simulation of hysteroscopy. *IFAC*, 2006. Epub ahead of print 2006. DOI: 10.3182/20060906-3-it-2910.00057.
- [34] Kesner SB, Howe RD. Position control of motion compensation cardiac catheters. *IEEE Trans Robot* 2011; 27: 1045–1055.
- [35] Rodr E, Kypson AP, Moten SC, *et al.* Autonomous catheter insertion system using magnetic motion capture sensor for endovascular surgery. *Int J* 2006; 211–215.
- [36] Ma X, Guo S. Dynamic performance analysis of a robotic catheter manipulating system. *2013 IEEE Int Conf Mechatronics Autom IEEE ICMA 2013* 2013; 779–784.
- [37] Arai F, Fujimura R, Fukuda T, *et al.* New catheter driving method using linear stepping mechanism for intravascular neurosurgery. *Proc - IEEE Int Conf Robot Autom* 2002; 3: 2944–2949.
- [38] Samantaray J, Chakrabarty S. Implementing sliding mode control of DC servo motor over a control network. *2018 Indian Control Conf ICC 2018 - Proc 2018; 2018-Janua*: 358–362.
- [39] Bartoszewicz A. Discrete-time quasi-sliding-mode control strategies. *IEEE Trans Ind Electron* 1998; 45: 633–637.
- [40] Shtessel YB, Shkolnikov IA, Brown MDJ. Asymptotic second-order smooth sliding mode control. *Asian J Control* 2003; 5: 498–504.
- [41] Park H, Song C, Kang M, *et al.* Forward imaging OCT endoscopic catheter based on MEMS lens scanning. *2012; 37*: 2673–2675.
- [42] Howell LL, Midha A. Parametric deflection approximations for end-loaded,

- large-deflection beams in compliant mechanisms. *J Mech Des Trans ASME* 1995; 117: 156–165.
- [43] Ya X, Xuejun L, Carin L, *et al.* Multi-task learning for classification with Dirichlet process priors. *J Mach Learn Res* 2007; 8: 35–63.
- [44] Yu KAI, Ji L, Zhang X. Kernel Nearest-Neighbor Algorithm. 2002; 147–156.
- [45] Keller JM, Gray MR. A Fuzzy K-Nearest Neighbor Algorithm. *IEEE Trans Syst Man Cybern* 1985; SMC-15: 580–585.
- [46] Morgan Quigley, Brian Gerkey, Ken Conley, Josh Faust, Tully Foot, Jeremy Leibs, Eric Berger, Rob Wheeler AN. ROS: an open-source Robot Operating System. *IECON 2015 - 41st Annu Conf IEEE Ind Electron Soc* 2015; 4754–4759.
- [47] Khoshnam M, Skanes AC, Patel R V. Modeling and estimation of tip contact force for steerable ablation catheters. *IEEE Trans Biomed Eng* 2015; 62: 1404–1415.
- [48] Leine RI, Van Campen DH, De Kraker A, *et al.* Stick-Slip Vibrations Induced by Alternate Friction Models. *Nonlinear Dyn* 1998; 16: 41–54.
- [49] Braun OM, Barel I, Urbakh M. Dynamics of Transition from Static to Kinetic Friction. *Phys Rev Lett* 2009; 103: 1–4.
- [50] Young KD, Utkin VI. Sliding Mode in Systems with Parallel Unmodeled High Frequency Oscillations. *IFAC Proc Vol* 1995; 28: 483–487.
- [51] Cagal K, Salamci MU, Cevik F. Proportional-Integral Sliding Mode Controller Design for a Fin Actuation Mechanism. 2020; 1–6.
- [52] Gao W, Wang Y, Homaifa A. Discrete-Time Variable Structure Control Systems. *IEEE Trans Ind Electron* 1995; 42: 117–122.
- [53] Shtessel Y, Edwards C, Fridman L, *et al.* Sliding mode control and observation. Springer, 2014.
- [54] Liu Y, So RMC, Zhang CH. Modeling the bifurcating flow in an asymmetric

- human lung airway. *J Biomech* 2003; 36: 951–959.
- [55] Wolber T, Ryf S, Binggeli C, *et al.* Potential interference of small neodymium magnets with cardiac pacemakers and implantable cardioverter-defibrillators. *Hear Rhythm* 2007; 4: 1–4.
- [56] Oono N, Sagawa M, Kasada R, *et al.* Production of thick high-performance sintered neodymium magnets by grain boundary diffusion treatment with dysprosium-nickel-aluminum alloy. *J Magn Magn Mater* 2011; 323: 297–300.
- [57] Li H, Tan J, Zhang M. Dynamics modeling and analysis of a swimming microrobot for controlled drug delivery. *IEEE Trans Autom Sci Eng* 2009; 6: 220–227.
- [58] Beléndez T, Neipp C, Beléndez A. Large and small deflections of a cantilever beam. *Eur J Phys* 2002; 23: 371–379.
- [59] Su HJ. A pseudorigid-body 3r model for determining large deflection of cantilever beams subject to tip loads. *J Mech Robot* 2009; 1: 1–9.
- [60] Ariefka R, Pramudya Y. The study of hollow cylinder on inclined plane to determine the cylinder moment of inertia. *J Phys Conf Ser*; 1170. Epub ahead of print 2019. DOI: 10.1088/1742-6596/1170/1/012081.
- [61] Umemoto M, Liu ZG, Sugimoto S, *et al.* Tensile Stress-Strain Analysis of Single-Structure Steels. 31.
- [62] O’Connell JLG, Robertson WSP, Cazzolato BS. Simplified equations for the magnetic field due to an arbitrarily-shaped polyhedral permanent magnet. *J Magn Magn Mater* 2020; 510: 166894.
- [63] Wong M-F, Picon O, Hanna VF. Finite Element Method Based On Whitney Forms. *IEEE Trans Magn* 1995; 31: 4–7.
- [64] Nagy Z, Nelson BJ. Lagrangian modeling of the magnetization and the magnetic torque on assembled soft-magnetic MEMS devices for fast computation and analysis. *IEEE Trans Robot* 2012; 28: 787–797.

- [65] Yamaguchi E. Finite element method. Bridg Eng Handb Fundam Second Ed 2014; 225–251.
- [66] Introduction to Comsol Multiphysics. Comsol Inc 2011; 1–162.
- [67] Blauch AJ, Bodson M, Chiasson J. High-Speed Parameter Estimation of Stepper Motors. IEEE Trans Control Syst Technol 1993; 1: 270–279.
- [68] Bernal J, Sanchez J, Vilarino F. Impact of image preprocessing methods on polyp localization in colonoscopy frames. Proc Annu Int Conf IEEE Eng Med Biol Soc EMBS 2013; 7350–7354.
- [69] Swathi C, Anoop BK, Dhas DAS, *et al.* Comparison of different image preprocessing methods used for retinal fundus images. 2017 Conf Emerg Devices Smart Syst ICEDSS 2017 2017; 175–179.
- [70] Cawkell AE. Image Processing. Inf Serv Use 2008; 11: 33–34.
- [71] Yusuf Sukman J. İNSANSIZ HAVA ARAÇLARINDA GÖRÜNTÜ İŞLEME İLE ROTA TESPİTİ VE OTONOM TAKİBİ. BÜLENT ECEVİT ÜNİVERSİTESİ YÜKSEK LİSANS TEZİ 2017; 4: 9–15.
- [72] Brainard DH, Wandell BA. Analysis of the retinex theory of color vision. J Opt Soc Am A 1986; 3: 1651.
- [73] Chen W, Shi YQ, Xuan G. Identifying computer graphics using HSV color model and statistical moments of characteristic functions. Proc 2007 IEEE Int Conf Multimed Expo, ICME 2007 2007; 1123–1126.
- [74] Wu G, Rahimi A, Goh K, *et al.* Identifying color in motion in video sensors. Proc IEEE Comput Soc Conf Comput Vis Pattern Recognit 2006; 1: 561–569.
- [75] Kemal E, Nihat Y. Shifting Colors to Overcome not Realizing Objects Problem due to Color Vision Deficiency. Conf Adv Comput Electron Electr Technol 2014; 11–14.
- [76] Gupta G. Algorithm for Image Processing Using Improved Median Filter and Comparison of Mean, Median and Improved Median Filter. Int J Soft Comput

2011; 304–311.

- [77] Burt PJ. Fast filter transform for image processing. *Comput Graph Image Process* 1981; 16: 20–51.
- [78] Zhu R, Wang Y. Application of improved median filter on image processing. *J Comput* 2012; 7: 838–841.
- [79] Tao Chen, Kai-Kuang Ma and L-HC. Tri-State Median Filter for Image Denoising. *IEEE Trans IMAGE Process* 1999; 8: 1834–1838.
- [80] Deng G, Cahill LW. Adaptive Gaussian filter for noise reduction and edge detection. *IEEE Nucl Sci Symp Med Imaging Conf* 1994; 1615–1619.
- [81] Gil JY, Kimmel R. Efficient dilation, erosion, opening, and closing algorithms. *IEEE Trans Pattern Anal Mach Intell* 2002; 24: 1606–1617.
- [82] Bach-y-Rita P, W. Kerckel S. Sensory substitution and the human-machine interface. *Trends Cogn Sci* 2003; 7: 541–546.
- [83] Strausser KA, Kazerooni H. The development and testing of a human machine interface for a mobile medical exoskeleton. *IEEE Int Conf Intell Robot Syst* 2011; 4911–4916.
- [84] Software BS-I, 1988 U. What is Object-Oriented Programming. *IeeexploreIeeeOrg*, <https://ieeexplore.ieee.org/abstract/document/2020/>.
- [85] Stefik M, Bobrow DG. Object-Oriented Programming: Themes and Variations. *AI Mag* 1986; 6: 40–62.
- [86] Badamasi YA. The working principle of an Arduino. *Proc 11th Int Conf Electron Comput ICECCO 2014* 2014; 7–10.
- [87] Culjak I, Abram D, Pribanic T, et al. A brief introduction to OpenCV. *MIPRO 2012 - 35th Int Conv Inf Commun Technol Electron Microelectron - Proc* 2012; 1725–1730.
- [88] Pulli K, Baksheev A, Korniyakov K, *et al.* Realtime computer vision with OpenCV. *Queue* 2012; 10: 1–17.

- [89] Nemati H, Bando M, Hokamoto S. Chattering Attenuation Sliding Mode Approach for Nonlinear Systems. *Asian J Control* 2017; 19: 1519–1531.
- [90] City T. Variable Structure Robot Control Undergoing Chattering Attenuation: Adaptive and Nonadaptive Cases. 1994; 1824–1829.



Republic of Turkey
İzmir Kâtip Çelebi University
Graduate School of Natural and Applied Sciences

Design of a Catheter Motion Control System

Department of Mechanical Engineering

Master's Thesis

Gökmen Atakan Türkmen

ORCID 0000-0002-4845-6547

Thesis Advisor: Doc. Dr. Levent Çetin

August 2021

∞ TÜRKMEN Design of a Catheter Motion Control System MASTER' S THESIS 2021



Curriculum Vitae

Name Surname : Gökmen Atakan Türkmen

Education:

2014–2019 İzmir Kâtip Çelebi University, Dept. of Mechatronic Eng.

2018–2021 İzmir Kâtip Çelebi University, Dept. of Mechanical Eng.

Work Experience:

2016 Summer Internship İzmir Mekanik

2016 Summer Internship Destek Otomasyon

2017 Summer Internship Destek Otomasyon

Publications (if any):

1. Kateter Tahrik Sisteminin Kayma Kipli Kontrolü ve Bulanık Mantık ile Performans İyileştirmesi (Sliding Mode Control of Catheter Drive System and Performance Improvement via Fuzzy Logic)